Measurements of the High Latitude Middle Atmosphere Dynamic Structure Using Lidar

C.R. PHILBRICK   R. SLUDER
D.P. SIPLER   F.J. SCHMIDLIN
B.E. DIX   L.D. MENDENHALL
G. DAVIDSON   K.H. BHAVNANI
W.P. MOSKOWITZ   K.J. HAHN
C. TROWBRIDGE

18 February 1987
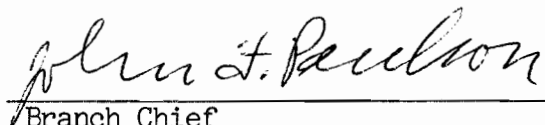
IONOSPHERIC PHYSICS DIVISION   PROJECT 7670

GEOPHYSICS LABORATORY

HANSCOM AFB, MA 01731-5000

"This technical report has been reviewed and is approved for publication"

FOR THE COMMANDER

Branch Chief
JOHN F. PAULSON, Acting Branch Chief
Ionospheric Interactions Branch
Ionospheric Physics Division

Division Director
ROBERT E. HUFFMAN, Acting Director
Ionospheric Physics Division

Qualified requestors may obtain additional copies from the Defense Technical
Information Center.

If your address has changed, or if you wish to be removed from the mailing
list, or if the addressee is no longer employed by your organization, please
notifiy AFGL/DAA, Hanscom AFB, MA 01731. This will assist us in maintaining
a current mailing list.

Do not return copies of this report unless contractual obligations or notices
on a specific document requires that it be returned.

REPORT DOCUMENTATION PAGE		*Form Approved* *OMB No. 0704-0188*
1a. REPORT SECURITY CLASSIFICATION Unclassified		1b. RESTRICTIVE MARKINGS
2a. SECURITY CLASSIFICATION AUTHORITY		3. DISTRIBUTION/AVAILABILITY OF REPORT Approved for Public Release; Distribution Unlimited
2b. DECLASSIFICATION/DOWNGRADING SCHEDULE		
4. PERFORMING ORGANIZATION REPORT NUMBER(S) AFGL-TR-87-0053 ERP, No. 967		5. MONITORING ORGANIZATION REPORT NUMBER(S)

6a. NAME OF PERFORMING ORGANIZATION Air Force Geophysics Laboratory	6b. OFFICE SYMBOL *(If applicable)* LID	7a. NAME OF MONITORING ORGANIZATION
6c. ADDRESS *(City, State, and ZIP Code)* Hanscom AFB, Massachusetts 01731		7b. ADDRESS *(City, State, and ZIP Code)*
8a. NAME OF FUNDING/SPONSORING ORGANIZATION	8b. OFFICE SYMBOL *(If applicable)*	9. PROCUREMENT INSTRUMENT IDENTIFICATION NUMBER

8c. ADDRESS *(City, State, and ZIP Code)*	10. SOURCE OF FUNDING NUMBERS			
	PROGRAM ELEMENT NO.	PROJECT NO.	TASK NO	WORK UNIT ACCESSION NO.
	62101F	7670	16	01

11. TITLE *(Include Security Classification)*
Measurements of the High Latitude Middle Atmosphere Dynamic Structure using Lidar

12. PERSONAL AUTHOR(S) C.R. Philbrick, D.P. Sipler, B.E. Dix, G. Davidson*, W.P. Moskowitz*, C. Trowbridge,* R. Sluder,* F.J. Schmidlin+, L.D. Mendenhall**, K.H. Bhavnani++ (over)

13a. TYPE OF REPORT Scientific, Interim	13b. TIME COVERED FROM 2/18/1987	14. DATE OF REPORT *(Year, Month, Day)* 1987, February 18	15. PAGE COUNT 142

16. SUPPLEMENTARY NOTATION
*Photometrics, Inc.   ** Space Division
+NASA Wallops   ++ Radex, Inc.

17. COSATI CODES			18. SUBJECT TERMS *(Continue on reverse if necessary and identify by block number)*
FIELD	GROUP	SUB-GROUP	Lidar, Atmospheric density, Middle atmosphere, Atmospheric variations, High latitude atmosphere

19. ABSTRACT *(Continue on reverse if necessary and identify by block number)*

Between February and April 1986, a new mobile lidar was used to obtain data on the variations that occur in the high latitude atmosphere between 20 and 85 km. Data were obtained on 26 nights during the program. Standard meteorological balloon and rocket payloads also measured the density, for comparison with the lidar data. More than a thousand profiles of atmospheric density were obtained with the lidar and 20 meteorological rockets were launched.

Comparisons between the lidar data and the meteorological rocket data showed generally good agreement. However, the lidar data from the February period is offset 12-14 percent from the rocket data. The March and April data, including 14 sets of overlapping data, generally agree to within 3 percent

20. DISTRIBUTION/AVAILABILITY OF ABSTRACT ☒ UNCLASSIFIED/UNLIMITED ☐ SAME AS RPT. ☐ DTIC USERS	21. ABSTRACT SECURITY CLASSIFICATION Unclassified	
22a. NAME OF RESPONSIBLE INDIVIDUAL John Meriwether	22b. TELEPHONE *(Include Area Code)* (617) 377-4944	22c. OFFICE SYMBOL LID

DD Form 1473, JUN 86   *Previous editions are obsolete.*   SECURITY CLASSIFICATION OF THIS PAGE

(Continued from Block 12) K.J. Hahn++.

Contents

Contents (contd)

Illustrations

Foreword

When Dr Philbrick left the Geophysics Laboratory in March 1988, he had completed the text of this report, and had selected the illustrations. He sent approximately half of the illustrations to the Laboratory in March 1989. The departure of Dr Dwight Sipler from the Laboratory during this time period further delayed publication of the report.

Through my association with several of the authors of this report, I had learned that it had been written, and thus, when I came to the Geophysics Laboratory in June 1989, I began to seek its publication in some form. It is my hope that publication of this report will further the use of lidar as a probe of the middle atmosphere.

--John Meriwether

A recent effort at AFGL has been to develop techniques for remote sounding of the atmospheric properties using lidar. The work was begun in 1979. A portion of this effort was accelerated to complete a transportable lidar. The mobile lidar would provide information on atmospheric structure and variability at various locations in support of Space Division test programs. The laboratory lidar system was developed to provide a test of new technology and to gather a long term data base. The laboratory instrument was placed into service in 1983. The equipment for the mobile lidar system, which was scaled from our laboratory efforts, was placed into a 32 foot trailer in June 1985. In September 1985, the trailer was shipped to NASA Wallops Facility for the first comparisons of a lidar with standard meteorological rocket and balloon sensors.

In response to a 4 December TWX request from SD, we designed an investigation for making lidar measurements from Alaska during the January-February 1986 winter period. This deployment was requested as a way. gather a data base to better understand the variability of the high latitude structure. The impetus for the effort was to better understand the atmospheric variations which may effect the reentry of Shuttle from a polar orbit. Many factors relating to that deployment were considered. A plan was prepared which represented a proposed approach to meet the stated objectives with minimum cost and a reasonable chance of successfully obtaining the goals. The plan included the following elements:

a. Deployment of the lidar to obtain measurements of structure properties for a period of four weeks at high latitude during peak winter conditions. Attempt to obtain measurements on each night on which the sky can be observed with the goal of obtaining profiles on at least 10 of the nights during a 30 day measurement period.

b. Obtain rawinsonde balloon measurements of structure properties between the surface and 30 km. The results will be compared with the lidar returns and used to account for the transmission of the lower atmosphere. The standard meteorological measurements from the Fairbanks Airport NOAA station would be supplemented during the period of this data set.

c. Make meteorological rocket measurements using Super-Loki datasondes and passive spheres. The rocket payloads would provide measurements of the structure profiles from 20 km to altitudes of 60 and 90 km, respectively. The results will be used to compare with the lidar results and to investigate the small scale features by combining the in-situ rocket measurements and the remote sensing lidar measurements.

The lidar trailer packing was started on 12 January 1986 at Wallops Island, Va. The trailer was loaded onto a C-141 on 28 January for transport to Eielson AFB at Fairbanks, Alaska. The ground transportation of the trailer to Poker Flat Research Range (about 30 miles northeast of Fairbanks) was accomplished on 31 January. On 12 February, the unpacking and setup of the trailer was completed. The alignment and calibration tests were completed on 14 February and the data collection period started. Data was collected on each night when weather permitted from 14 February to 9 March. The corresponding launches of meteorological rockets were delayed by range safety problems involving the mount for the launch rail and errors in booster impact prediction. The lidar data collection proceeded during the period of solving the launcher problems. A failure in the laser power supply occurred on 9 March which was repaired on 21 March. When testing verified that the laser was working properly, a break was taken to wait for a period when range support would allow additional rocket launchings. On 15 April, the lidar was reactivated and data obtained. The range personnel took a brief vacation between 17 April and 21 April. On 27 and 28 April, the remaining rocket payloads were launched together with lidar data collection. The packing and wrap-up of the field campaign was concluded on 10 May 1986.

This program was carried out as a first test of a new instrument, and therefore, not everything worked as well as might be hoped. The most significant problems resulted from power line noise and power variations which necessitated major efforts to correct problems in the data (shutter variation and shutter sync-lock loss). However, these problems are understood and can be easily solved by electrical isolation in the future. During the program, a total of more than 2600 lidar profile returns were obtained and 17 meteorological rockets were successfully launched. A valuable set of data has been obtained and interesting scientific conclusions have been developed from the results. It is our hope that this effort will have proved to be an important step in the development of lidar techniques for sounding of the properties of the atmosphere.

Comparisons between the lidar data and the meteorological rocket data show generally good agreement. However, the lidar and rocket data from the February period has a significant (12-14%) relative offset. The March and April data, including fourteen sets of overlapping data, are generally in good agreement, within about 3% (excluding the high altitude portion of the April data).

The measurement campaign has resulted in the following new points relative to our understanding of the atmospheric properties:

(1) At each altitude, there is an irregularity, or granularity, to the horizontal density distribution which is modulated on any line-of-sight by the horizontal wind. This is an important perspective in understanding the small (few percent) variations in the density which are always present. The small variations are present in all known data sets of atmospheric structure with sufficient resolution, but the lidar data has provided the first opportunity to actually observe the background granularity of the atmosphere.

(2) Planetary waves are apparent throughout the middle atmosphere in the lidar data. The planetary waves may be associated with more than half of the total amplitude of the observed density variation. It may become possible, during the high latitude winter season, to follow the planetary waves to separate their phase and amplitude relationships. If the phase and amplitude of the planetary waves were used, then improved predictions of the middle atmosphere density and temperature could be expected (possibly allowing predictions of such variations as stratospheric warmings).

(3) The gravity wave variations in the high latitude winter atmosphere result in constructive and destructive interference of wave components, which can not be easily separated. The winter high latitude data which is available seldom exhibits the easily discernable, near monochromatic wave structure, which has been found in summer data. The number of sources, the intensity of the sources, and the lower atmosphere transmission of gravity waves are larger in the winter than during the summer. The interference of the waves and the extraction of wave energy by turbulence in the lower mesosphere prevent the amplitudes of the waves from growing to the intensity which they would if monochromatic waves were present.

(4) These measurements provide a major step toward developing the lidar as a tool for routine meteorological and atmospheric measurements in the future. Comparisons of the rocket and balloon measurements with the lidar lead to the conclusion that the lidar can provide comparable accuracies to the current techniques and at significantly less expense in manpower and hardware. It is expected that the lidar sounder will be developed as an operational tool to fulfill a major part of the requirements for meteorological rocket measurements by the mid-90's.

Acknowledgments

1. INTRODUCTION

LIDAR is an acronym, LIght Detection And Ranging, similar to the word 'radar', except that light is used instead of radio waves. The basic principles are similar, i.e. a short pulse of light is transmitted, scatters from an object and returns to the detector. In atmospheric sounding, the lidar pulse is scattered from molecules (Rayleigh or Raman scattering), from particles of dust or aerosols (Mie scattering), from species at specific wavelengths (resonance fluorescence), or from a target (path integrated attenuation). The range is determined by the delay time between transmit and receive. A very simplified description of an atmospheric sounding lidar is given by the equation,

$$(1) \qquad\qquad S = P_0 \, K \, n \, r^2$$

where S is the detected signal, P_0 is the transmitted power, K is a constant containing system parameters, n is the number of scatterers and r is the range of the scattering volume. In the radar equation the range dependence is usually r^4, but that is for a target which is small compared to the dimensions of the transmitted beam so that the illumination of the target depends on r^2 and the light scattered from the target into the detector is also proportional to r^2. In atmospheric measurements, the target completely fills the beam and only the scattered light has a range dependence. The number of Rayleigh scatterers is just the number density of the atmosphere. The parameter K includes such things as the optical system efficiency (both transmit and receive), extinction of the light by the atmosphere (mostly dust and aerosols in the lower atmosphere), and the molecular scattering cross section of the atmospheric molecules (basically a constant up to around 90 km).

Several different scattering processes are important for lidar measurements of the atmosphere:

> Rayleigh scattering
> Mie scattering
> Raman scattering
> Resonance scattering
> DIAL (DIfferential Absorption Lidar)

Rayleigh scattering is the scattering of light by molecules and is familiar to most people as the process that causes the blue color of the sky due to its wavelength dependence. Rayleigh scattering theory describes the scattering of electromagnetic radiation by particles which are small compared to the

1

wavelength of the radiation. In atmospheric sounding, the scattering particles are the atoms and molecules which make up the atmosphere. The scattering cross section is relatively small and varies as $1/\lambda^4$, where λ is the wavelength of the scattered radiation.

Mie scattering theory describes the scattering of electromagnetic radiation by particles with sizes on the order of the wavelength of the radiation or larger. This process is important in the lower regions of the atmosphere (from the ground to about 25 km) where dust and aerosols are significant components of the atmosphere. The wavelength dependence of this type of scattering is a complex function of particle size and wavelength but in general the scattering cross section is significantly larger than the Rayleigh cross section and varies approximately as $1/\lambda$.

Raman scattering is similar to Rayleigh scattering except that whereas Rayleigh scattering is an elastic process, Raman scattering is inelastic scattering. This means that a photon, when scattering from an atom or molecule, leaves some of its energy behind in the atom or molecule. Since only discrete energy levels are available and these depend on the electric dipole field of the particular molecule, the energy loss will be characteristic of the particle doing the scattering. The energy loss means that the wavelength of the scattered light will be longer (lower energy) than the light from the laser. Thus, by selecting a particular wavelength shift with an interference filter, measurements can be made on specific components of the atmosphere, for example, N_2, O_2, or H_2O. The Raman scattering cross section is small, about 10^{-3} of the Rayleigh cross section. This limits the utility of this process to lower altitudes where the signal is sufficient. However, this is just where this sort of measurement is needed, since the scattering is relatively insensitive to the presence of dust and aerosols.

Resonance scattering is another process that depends on specific energy levels in a scattering atom or molecule. If the laser can be tuned to a wavelength that represents the exact energy needed to raise the target atom to an excited state from the ground state through an allowed transition, then the cross section for absorption and reradiation of light will be very large. This large cross section makes this process suitable for the measurement of minor components of the atmosphere, such as free atomic sodium, which occurs in a thin layer between approximately 85 and 105 km altitude. The sodium density in this region is on the order of 10^4 cm^{-3} compared to the ambient atmospheric density of around 10^{14} cm^{-3}. However, the resonance cross section is about 11 orders of magnitude larger than the Rayleigh cross section, so measurements of sodium can be performed with moderate laser power. Other workers have used this same technique to look at calcium, potassium, lithium and iron. The technique can also be used on ions as well as neutrals.

2

The **DIAL** (DIfferential Absorption Lidar) technique is based on the detection of the absorption difference between two laser wavelengths. One wavelength is tuned to an absorption line of the species of interest, the second wavelength is chosen to be in an absorption free region. The wavelengths are chosen to be near each other, so that both experience the same broadband attenuation. The measurement results in a range resolved profile of species concentration. The technique is applicable to water vapor, ozone and other species. A measurement of the ozone concentration between 15 and 60 km should be routinely available using DIAL techniques.

We have developed the lidar system for measurements of atmospheric density and temperature to high altitudes. The system was used in this campaign to prove its capability. These and future efforts are intended to improve the system by extending the high altitude range of the lidar and by using additional technology. The field measurements are particularly important to provide correlative data for comparison of the measurements.

The results of this investigation have shown the great value of lidar as a tool that can eventually replace the meteorological rocket techniques fc   ddle and upper atmosphere density and temperature profiles. The comparisons of the simultaneous rocket and lidar measurements generally show good agreement. The differences, some due to deficiencies in the lidar instrument and some due to previously unrecognized deficiencies in the meteorological rocket techniques, have been studied.

The investigation has yielded significant understanding regarding the following points:

(1) small scale structure of the atmosphere includes a granularity in density and temperature, which moves in the background wind field, causing variations in the structure profiles when measured along a particular path;

(2) the middle atmospheric component of planetary scale waves, the higher altitude equivalent of tropospheric planetary waves, are associated with the larger variations in density and temperature of the high latitude middle atmosphere in winter;

(3) the constructive interference of several planetary wave components appear to determine the amplitude and occurrence of minor and major stratospheric warmings (leading to possible predictability);

3

(4) the mean gradients of the atmospheric structure profiles, which are determined by the seasonal and planetary wave activity, are most important in determining the stability of the atmosphere and defining the regions for gravity wave growth or wave breaking;

(5) the gravity wave transmission in the high latitude winter atmosphere is governed by the gradient of the mean structure profile determined by the longer wavelength/period structure, or planetary waves;

(6) the smaller scale features present in the atmosphere are frequently the result of constructive interference of several wave components;

(7) strong optical scattering in the 18-25 km altitude region, which is probably due to combination of polar stratospheric clouds and volcanic dust layers, was observed during the measurement period.

The high latitude middle atmosphere changes significantly from winter conditions in February to summer-like conditions after the equinox. The large seasonal changes, which have been observed, follow the general trends which can be found in reference models of the high latitude region. That is, the winter mesosphere density is about half of the density described by the U.S. Standard Atmosphere and the density profiles around equinox period are in very close agreement to the model.

2. DESCRIPTION OF THE GLINT SOUNDER

The Ground-based Lidar INvestigation - Transportable (GLINT) sounder is a scaled, mobile version of the rooftop laboratory lidar sounder used at AFGL. Hardware testing was begun in June 1985 and the instrument was taken to the NASA Wallops facility in September 1985 for tests and comparisons with standard meteorological techniques. In Phase I of the lidar program, the molecular and particulate scattering measurements in the visible and ultraviolet were used to determine the density and temperature of the atmosphere. This two-color approach allows the recognition of regions in which the molecular (Rayleigh) scattering signal is contaminated by particulate (Mie) scattering due to the presence of aerosols or dust.

The AFGL laboratory facility, referred to as GLEAM (Ground-based Lidar Experiment for Atmospheric Measurements), consists of transmitter, receiver, data and safety systems. The transmitter is a 2 joule per pulse Nd:YAG laser with a doubler (532 nm) and tripler (355 nm) that outputs 10 nsec pulses at a rate of 10 per second. The receiver is a 92 cm Dall-Kirkham telescope that collects the backscattered light, and a 6-channel detector system with a mechanical shutter, which measures the return signal using photon counting techniques. The data system uses a LeCroy 3500 microprocessor to accumulate the counts from the detectors during periods of laser firing and during background measurement periods. The LeCroy 3500 is also used to display and store the accumulated signal for later processing into scientific results. The safety system consists of a number of internal laboratory interlocks and an automatic shut-down of the laser beam if the co-aligned X-band radar detects an aircraft near the beam.

The mobile lidar facility has been prepared as a scaled version of the fixed laboratory facility. The initial capability is similar to the Phase I measurements of the laboratory facility, but the overall sensitivity is reduced by a factor of between 3 and 5 (that is, about the same sensitivity at one to two density scale heights lower altitude). The mobile instrument is not restricted to vertical measurements. That restriction was necessary for the laboratory facility because of its location at Hanscom AFB, in the landing pattern for the air field, and in the approach pattern for Logan Airport in Boston. In the design of the mobile sounder, care has been taken to minimize difficulties in extending the capabilities to Phase II (resonance fluorescence) and Phase III (Raman) measurements.

The preparation of the trailer and support electronics for the mobile lidar sounder was primarily a contractual effort by Tri-con Associates, Inc. Design and development of a detector system for a 32 cm telescope was carried out by their subcontractor, KEO Associates. The contractual effort was initiated

AFGL MOBILE
LIDAR
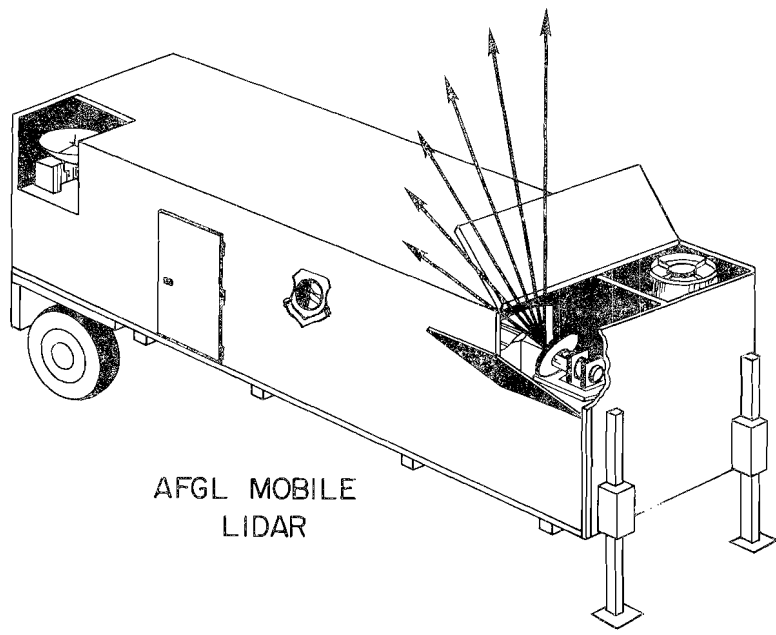
Figure 1. An Artist Sketch of the GLINT Trailer. The laser beam and primary telescope are co-aligned and the beam direction can be pointed at any angle from the horizon to the zenith. The high altitude telescope and the safety radar are indicated.

(GROUND - BASED LIDAR INVESTIGATION — TRANSPORTABLE)
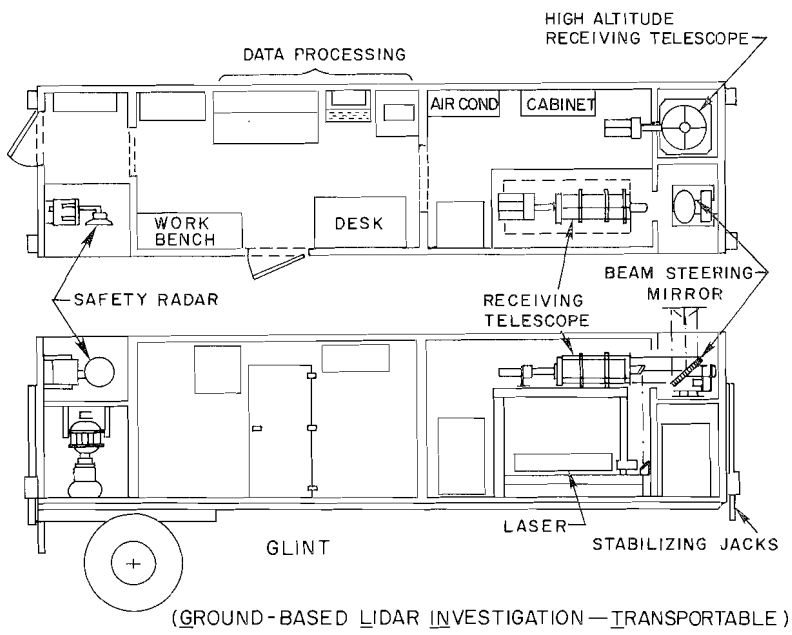
Figure 2. Top and Side Views of the Equipment Lay-out in the Trailer.

in June 1983. The final system-level equipment testing of the lidar was begun during June 1985. Figure 1 shows a drawing of the trailer configuration and Figure 2 shows a layout of the hardware within the facility. A photograph of the trailer is shown in Figure 3. The lidar beam can be steered from the horizon past the zenith by approximately 20°. The azimuth of the beam can also be steered by approximately 20° by tilting the steering mirror. The lidar consists of two receiver assemblies. A 32 cm telescope is co-aligned with the laser beam and its pointing direction is steered over the full range of elevation and azimuth. A 62 cm diameter telescope is used to measure near the zenith with higher sensitivity in a bi-static mode similar to that used in the laboratory sounder. In Table 1, the typical accuracy limits expected from the signal to noise are shown. The estimates are based on the preliminary analysis of the data obtained during a test period in December 1985, at Wallops Island, Va. The length of the filter interval is automatically changed in relation to the signal strength. The length of the filter and the criteria for changing the interval are described in Section 3.1.

Table 1. Estimate of Measurement Accuracy Obtained From 1/(Signal/Noise). These calculations are based on the 532 nm Rayleigh backscatter signal. Note that the altitude resolution is traded off for signal improvement at the higher altitudes. The 3000 and 9000 shot columns correspond to data runs of 5 and 15 minutes, respectively.

		32 cm Telescope		62 cm Telescope	
Altitude	Channel Width	3000 Shots	9000 Shots	3000 Shots	9000 Shots
20	0.3	0.03	0.03	0.03	0.03
30	0.3	0.03	0.03	0.03	0.03
40	0.3	0.03	0.03	0.03	0.03
50	0.6	0.03	0.03	0.03	0.03
60	0.6	0.04	0.04	0.04	0.03
70	1.2	0.12	0.07	0.05	0.03
80	2.4	0.26	0.15	0.12	0.07
90	2.4	0.80	0.45	0.35	0.20

NOTE: The table values represent the errors expected in the experiment. An error due to tie-on to a rawinsonde measurement in the 20 to 30 km altitude region contributes a bias error, estimated to be between 2 and 3 percent. The tie-on comparison is necessary to account for the tropospheric transmission. The lines in the tables indicate the region of comparable accuracy to the meteorological rocket techniques.

Figure 3. Side view of the GLINT Lidar Trailer. The running gear, corner jacks, tie down rings, and openings for the laser and the radar are clearly shown.

The principal subsystems of the mobile lidar sounder are the transmitter, the receiver and detectors, data system, and safety system.

2.1 Transmitter

The transmitter consists of four components: laser, beam expanding telescope, energy monitor, and beam steering optics. The laser used in the transmitter is a Quantel model YG581 laser (see Table 2)

that can transmit 1.5 joule energy pulses at 1064 nm at a pulse rate of 10 Hz. The Nd:YAG laser output is transformed by nonlinear optics to provide output at 532 nm (green) and 355 nm (ultraviolet). The normal operating energy output at 532 nm is typically 400-600 mJ and at 355 nm the typical output is 170-250 mJ. Figure 4 shows the arrangement of the transmit and receive components for the primary system. The laser beam is expanded in a 5X telescope that uses hard coated optics to expand the beam from 1 cm diameter to 5 cm diameter. The expansion also reduces the beam divergence by a factor of 5. The laser output has a beam divergence full angle of 0.7 mrad. After the beam expander, the beam divergence is 0.14 mrad. The expanded laser beam is folded onto the optical axis of the primary telescope and aligned with the optical axis to allow the scanning mechanism to point the laser beam and the telescope field of view in the same direction.

2.2   Receiver and Detectors

The primary receiving telescope is a 32 cm diameter Dall-Kirkham design supported and stabilized by invar rods. The advantages of the Dall-Kirkham configuration in lidar applications are its lower cost, narrow field of view, long focal length, and simple alignment and focusing. The steering optics for the receiver and transmitter cover the elevation range from horizontal to ±20° beyond the zenith using a motor controlled from the test console. The azimuth can be adjusted by an angle ±20° using a manually adjusted control mounted on the steering assembly. The transmitted beam is hidden from the sensitive detector by the mechanical shutter and the obscuration of the secondary mirror. In addition, the transmitted beam is reflected from a separate hard coated mirror at the center of the steering flat, to prevent multiple scattering and fluorescence in the large steering mirror from contaminating the signal. The received signal is focused through a detector assembly that includes a dichroic beam splitter and narrow-band interference filters to separate the green and ultraviolet wavelength returns. The large dynamic range for this detector is made possible by a calibrated variable aperture slot on a high speed rotating disk. Figure 5 shows the configuration of the shutter disk and representations of the optical image at the plane of the shutter wheel. The telescope primary is focused to an image of about 1 cm diameter on the plane of the mechanical shutter. The shutter is therefore acting as a variable neutral density filter by vignetting the light that uniformly illuminates the primary mirror. The mechanical approach taken to obtain the large dynamic range needed for the measurements should provide a more stable result than electrical switching techniques. The timing of the instrument is tied to the shutter. The shutter motor speed is 3600 rpm (60 rps) and thus the shutter is opened 120 times per second (2 open slots are located in the shutter). The laser fires at a rate of 10 Hz and therefore the program cycle is 12 shutter openings. The laser is always fired on the same shutter opening. One of the shutter periods is used to read out the energy monitor and 10 of the shutter openings are used to obtain data

Table 2. Properties of YAG Laser Used in the GLINT Facility

Manufacturer & Address: Quantel International
                           385 Reed Street
                           Santa Clara, CA 95050

Model & Serial Number: Model YG 581C; S/N 110
Laser Classification: AF Category D / Class IV
Description: Nd:YAG w/SHG, THG pulsed laser
Laser Output Energy:

Wavelength	Energy	Pulse Length
1064 nm	1.20 J (1.5 J max.)	10 nsec
532 nm	0.47 J (0.6 J max.)	9 nsec
355 nm	0.18 J (0.25 J max.)	8 nsec
	(Peak power 150 megawatts)	

Laser Pulse Length and Rate: τ, ν 10 nsec; 10 Hz
Beam Diameter at Laser: 0.95 cm at $1/e^2$ points
Beam Divergence of Laser: 0.7 mr at $1/e^2$ points
Beam Diameter after Beam Expander: 5 cm
Beam Divergence after Beam Expander: 0.14 mr
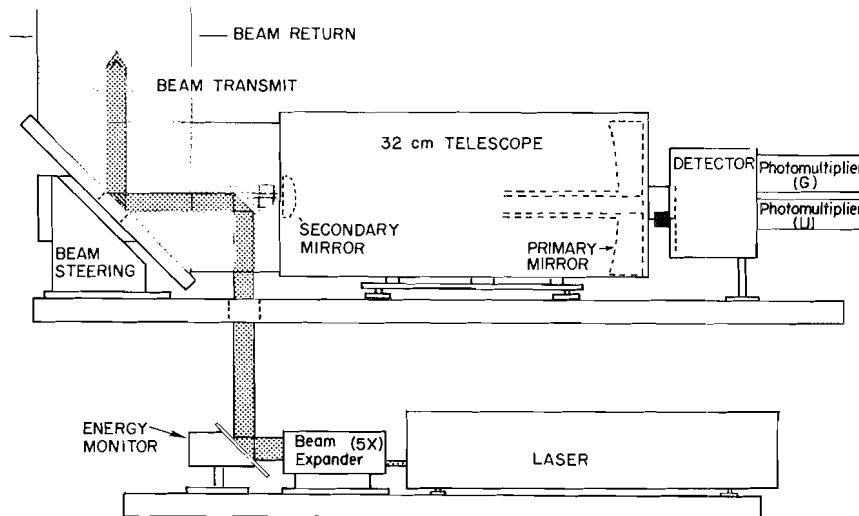
Figure 4.   A Side View of the Optical Layout of the Lidar.   The principal components and the relationship of the transmit beam path and the collected signal are shown.

10

SEGMENT OF SHUTTER WHEEL

PROPER IMAGE

~ 5.2mm
6 mm

IMAGE WITH ADDITIONAL
LIGHT SCATTING CONE ABOUT
SECONDARY MIRROR AND GREY
SCATTERING REGION AROUND
PRIMARY IMAGE
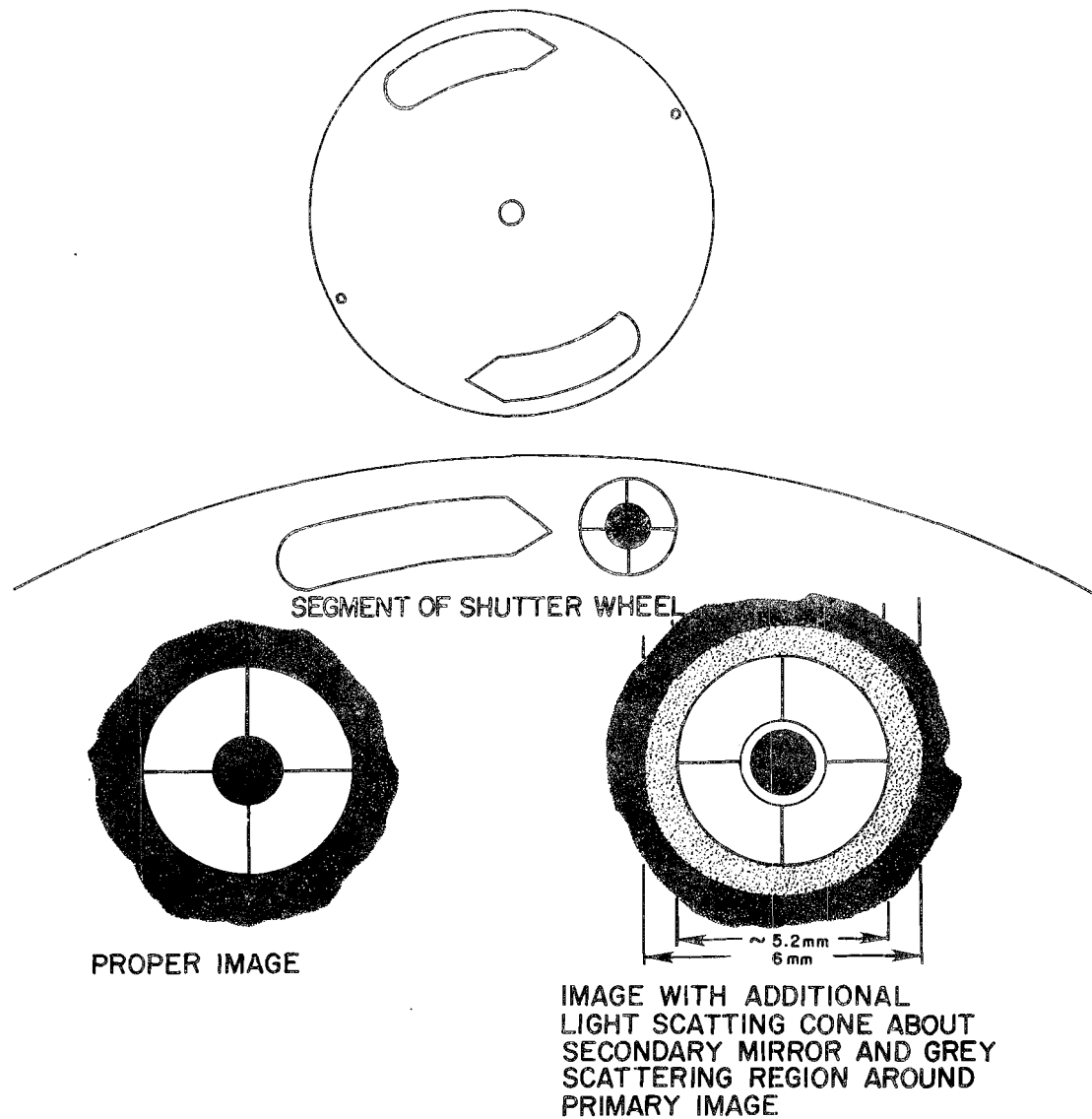
Figure 5. Representation of the Detector Shutter. (a) Two slots on the shutter wheel measure the sky background intensity during 10 periods of opening between each laser shot. The laser firing is timed in relation to the passage of the small timing slot. (b) The images at the plane of the shutter wheel are shown; the proper image, and the image resulting from off-axis double scattering off the secondary mirror and from grazing incidence scattering in the baffle tube.

11

on the sky background intensity. The, higher number of sky background measurements is important in order for the background correction to be statistically significant. The photomultiplier tubes used in the detector for both wavelengths are EMI tubes that have high sensitivity and are cooled to reduce the dark count. Photon counting techniques are used to measure the backscattered photons for altitudes above 10 km. In addition to the 32 cm primary receiving telescope, the trailer also houses a 62 cm telescope to extend the altitude range for measurements near the zenith and to provide additional flexibility for future detectors. The 62 cm telescope was designed in house, fabricated on an AF machine shop contract and was completed in November 1985. The initial task for this receiver is to extend the altitude range of the Rayleigh measurements and extend the capability for use under day-sky background conditions.

2.3 Data System

A LeCroy 3500 system provides the high speed data accumulation for the measurement. The multichannel scaler used in the LeCroy 3500 has a theoretical capability of 100 MHz count rates. Data from the two wavelength channels can be simultaneously stored in 2 μsec channels that provide 300 meter range resolution. The LeCroy system can accumulate and store the data as well as provide quick plots of the count rate versus channel number. Figure 6 shows the type of display available from the LeCroy for real time evaluation. To process the data in near real time, the data will be transferred into a desk computer for analysis. The desk computer can access or provide data with a standard modem interface. An example of the output screen dump from the quick-look analysis program is shown in Figure 7. Software that has been developed includes flexible programs for analysis, comparison and display of the results.

2.4 Safety System

Numerous safety interlocks and safety precautions are included in the design of the equipment and in the operating procedures used. The principal hazard for the lidar outside of the trailer is the eye safety hazard of the intense laser beam. The beam is sufficiently intense that looking into the beam or looking at a specular reflection or a near field diffuse reflection can cause temporary or permanent blindness. The eye safe distance for this lidar is about 35 km. A small radar unit has been included to shut the laser beam down when an aircraft enters the field of view within a few degrees of the beam. The safety radar used is an AN/APS-42 search radar with collision avoidance warning. The radar is used to disable the laser Q-switch automatically if a return pulse is detected. The transmitter uses an 18 inch diameter antenna dish with a 5.5° angle between the half power points. The receiver sensitivity

12
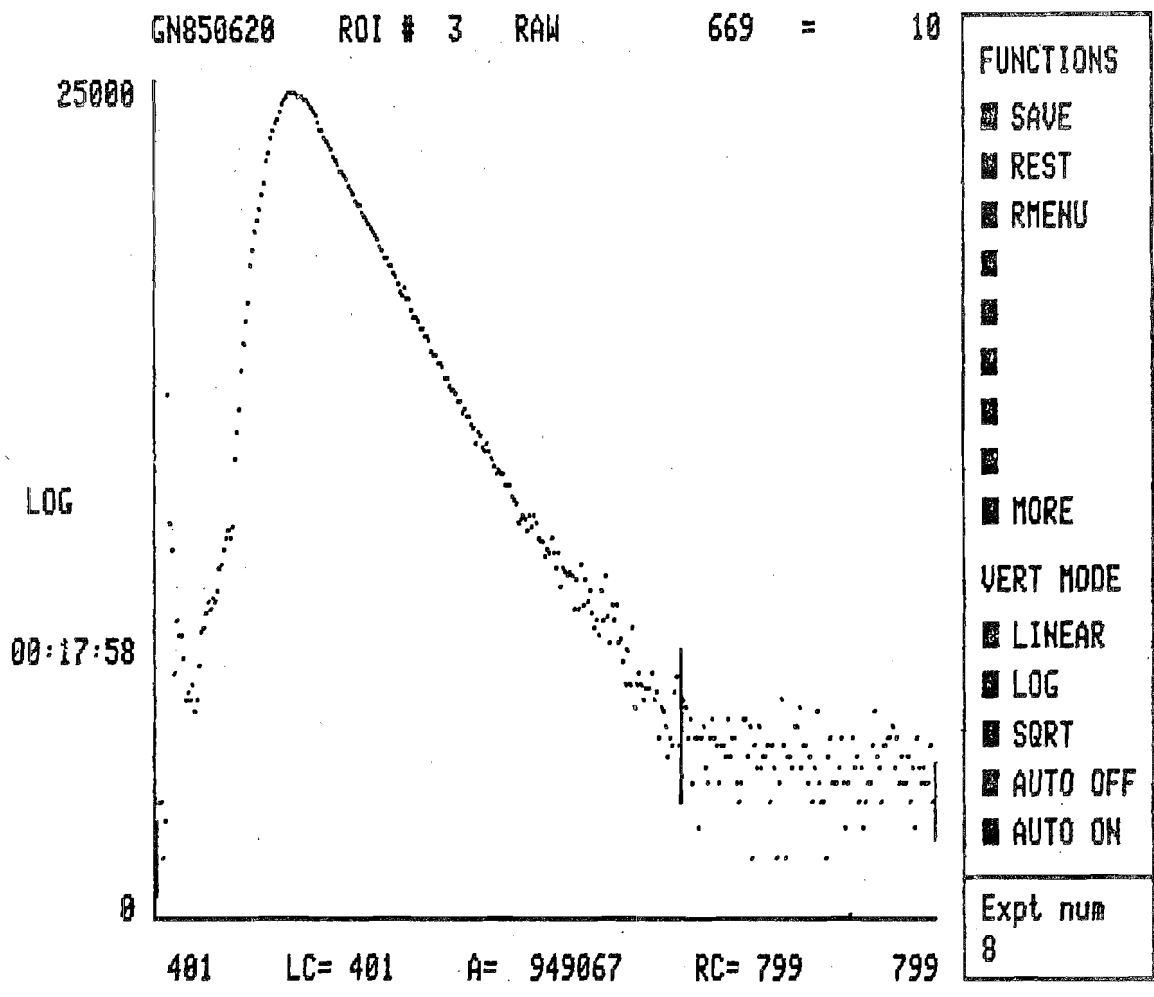
Figure 6. Example of the Real-time Screen Display. The vertical scale shows the log of the photon counts accumulated as a function of channel number (horizontal scale). The peak signal occurs near 20 km as the shutter opens; the full opening occurs near 45 km.

13
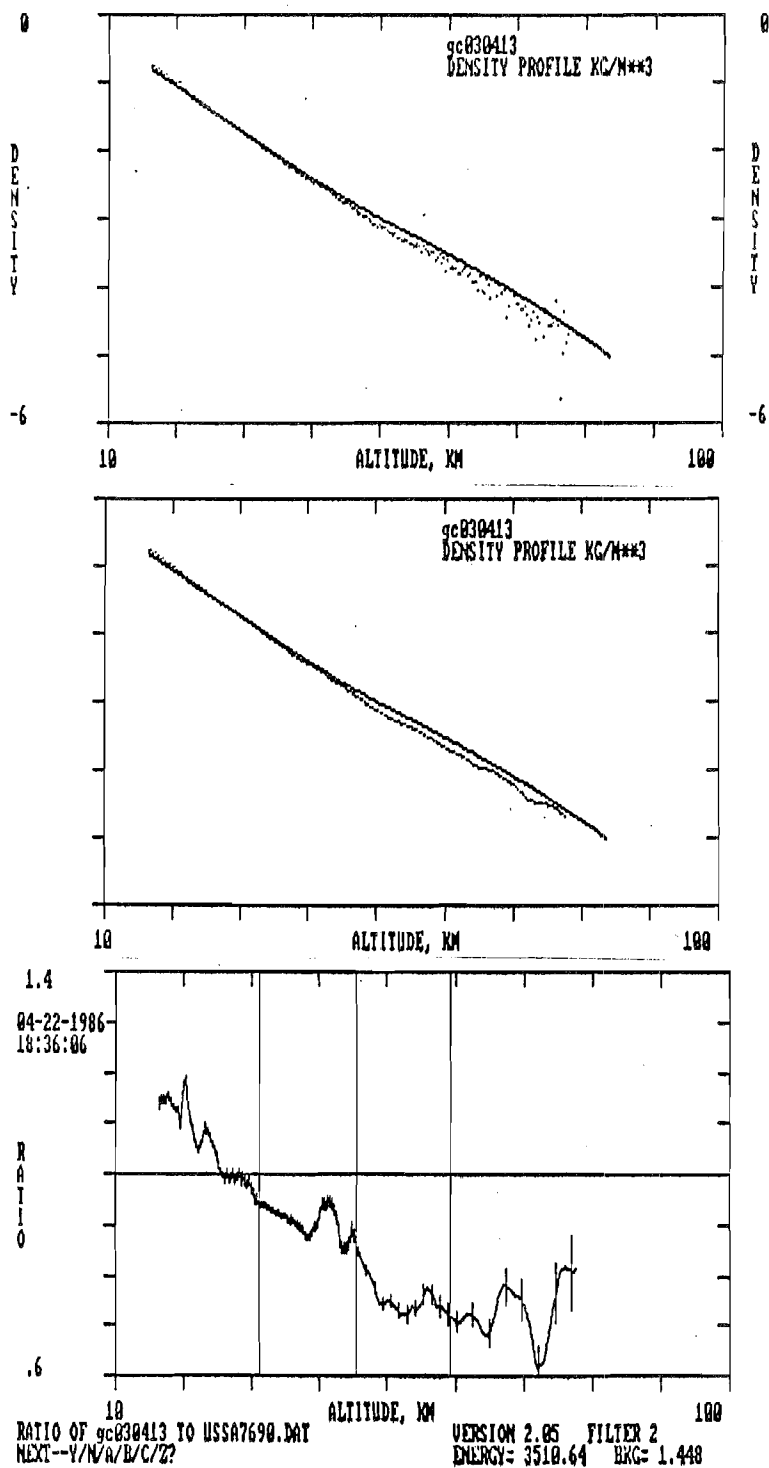
Figure 7. Example of the display from the Quick-look analysis that was applied in the field. The results are shown as (a) unsmoothed density calculated for each data channel compared to the USSA76 model, (b) smoothed density, and (c) as a ratio to the USSA76 model with the $\pm 1\sigma$ error bars (from photon count statistics).

14

will allow an automatic switch at 15 db signal to noise ratio which corresponds to detection of a 1 m^2 target at 25Kft. The smallest cross section of a typical single engine private plane is approximately 1.5 m^2. For altitudes below about 15Kft (near the upper limit for private planes), the radar should provide automatic turnoff with a safety margin of 10 msec for elevation angles from 90° to approximately 30°. During the operations in Alaska, daily contact was maintained with the FAA coordinator in Anchorage and AIR NOTAMS were issued each day of operation.

2.5 Field Requirements for Mobile Lidar Operation

The trailer has manually operated jacks on each corner that are used to raise and lower the body of the trailer during preparation for transport. The trailer specifications are summarized in Table 3. The wheel section can be removed which allows the unit to be transported in either C-130 or C-141 aircraft. At the destination airfield the wheels can be attached and the unit trucked to a final measurement location. The running gear can be installed by elevating the trailer which also allows a tractor to engage the fifth wheel connection. Once at a location, the corner jacks again are used to elevate the trailer for removal of the running gear undercarriage and to lower the trailer frame onto a level platform. Leveling can be accomplished with blocks and various thickness boards. The total weight for the trailer, its undercarriage, and equipment is about 19,000 pounds. Figure 3 shows the location of the cargo tie down rings. Four tie rings are located at floor level and evenly spaced on each side of the trailer. Four additional tie rings are located 24 in. above the skid (that is, about 12 in. above the center of gravity.) These rings were added to provide the required tie down points for air transport. They are located opposite each other and are tied together with internal structure when the trailer is to be transported. The design will allow a 10,000 lb. static pull to be applied to the rings in any direction when the internal structure is in place. The locations of these rings (see Figure 3) are at the corners and at locations 8 ft. 4 in. and 17 ft. 6 in. from the rear end of the trailer. The trailer center of gravity is located approximately 12 in. above the skid, 20 ft. from the rear end and on the centerline between the sides. The power requirement for electrical service is 208 volts, three phase, 100 amps with four conductors. The estimated requirement for all equipment operating and with sufficient heating or air conditioning for most applications is about 55 amps. The connectors used are standard 100 amp, four conductor connectors. A 75-ft. cable is available for connection directly to a fuse box or to a suitable connector. The severe weather conditions in Alaska made it necessary to prepare an arctic entryway for the trailer.

Table 3.   Summary of the Mobile Lidar (GLINT) Trailer Specifications.

Exterior Length   32 ft. (410 in. max.)
         Width   8 ft. (100.5 in. max.)
         Height   99.5 in. (101.5 in. max.)

Interior   Length   31 ft. 2 in.
           Width   7 ft. 4 in.
           Height   7 ft. 4 in.

Rear Door   7 ft. 0 in. X 3 ft. 5 in.
Side Door   6 ft. 6 in. X 3 ft. 5 in.

Exterior Wall   0.050 in. Thick Aluminum

Insulation   1-3/8 in. of Polyurethane foam (R-Value 10)

Tie Down Rings: 4 on each side welded to skids
                           4 on each side at height of 2 ft.

         Total 16 rings, each rated for 10,000 lb

Weight   Trailer   4300 lb
         Running Gear   2000 lb
         Equipment   13000 lb
         Total   19300 lb

Electrical Power   3 Phase
                           208 V
                           100 A (Estimate 55 A for normal operation)
                           4 Conductor

16

3. OVERVIEW OF THE MEASUREMENT PROGRAM

An AFGL effort was started in 1979 to develop a lidar sounder for remote sensing of the atmospheric properties. This effort included the development of a transportable lidar to provide information on atmospheric structure and variability at various locations in support of test programs and scientific field programs. The test in Alaska was carried out to provide additional data on the high latitude density variability. Shuttle flights had encountered significant perturbations in the aerodynamic forces in the altitude region between 60 and 90 km. The concern to be addressed was the larger variability in the atmospheric density at the higher latitudes that would be encountered during descent from polar orbit. The comparison with the current meteorological rocket and balloon techniques was included as an important part of such a test because of the need to compare and validate each of the techniques. Measurements obtained over the extended period are expected to provide information on the following topics:

(1) Data can be used for testing the current high latitude models of density and temperature between 20 and 80 km. The large data   could be used to add variability information (upper and lower deciles, or other statistical information) to the models.

(2) Measurements over an extended winter period are likely to provide some additional information on minor stratospheric warmings which cause rather significant perturbations of the structure parameters.

(3) Correlation of the structure of the density waves with the waves and shears observed in the wind field by the MST radar is important to developing and testing the ideas relating to growth and dissipation of atmospheric waves.

(4) The measurements would provide the first opportunity to study the sources of the wave generation and separate the contributions of the propagating waves, standing waves, and other irregularities in the atmospheric structure.

(5) A test of the limitations of various techniques could be made from the comparisons. The valid range and accuracy of each technique can be addressed.

The major objective of the experiment was to obtain a substantial number of profiles of the atmospheric structure parameters, which can be used to provide statistical envelopes of the variations

17

caused by waves and irregularities. The profiles are used to test models of the atmosphere and to study the aeronomy questions associated with the high latitude atmosphere. The winter season is usually considered to have the largest variations in the stratosphere and lower mesosphere. The measurements were obtained during a period when strong planetary wave activity and intense winter storms should result in enhanced gravity wave activity in the lower mesosphere.

4. DESCRIPTION OF THE METEOROLOGICAL MEASUREMENTS

The standard meteorological techniques currently used in the United States include the rawinsonde balloon for measurements between the surface and 30 km, the datasonde rocket for measurements between 20 and 65 km, and the passive sphere for altitudes between 30 and 90 km.

4.1 Rawinsonde

The rawinsonde balloons are normally released at 0000Z and 1200Z from the NOAA weather site at the Fairbanks Airport. The typical measurement times for the lidar were between 0400 and 1500Z. On the nights when the lidar measurements were being made, an additional rawinsonde balloon was released between 0600 and 0800Z. For each date that measurements were obtained, the rawinsonde preceding the measurement period and the two rawinsondes released during the measurement period were compared and used to provide a calibration reference for the lidar data set obtained during that time. In most cases, data are available in the altitude region between 25 and 35 km that can be used to calibrate the lidar data. Figure 8 shows an example plot of the three rawinsonde profiles on one night. The data were compared for each night of observation to select the tie-on region. The upper two kilometers of the balloon data were generally used to provide the reference for the lidar data and effectively remove the transmission variation of the lower atmosphere. The two assumptions that are necessary but can lead to errors in taking this approach are:

(1) the atmospheric variations in a thick layer of the atmosphere are stable to within a couple of percent for periods of a few hours in the altitude region near 30 km; and

(2) the backscatter intensity from the tie-on region is purely due to Rayleigh scatter.

Assumption (1) is apparently valid from an examination of the rawinsonde data that was collected. Assumption (2) has been tested on each data-taking night by comparing the signal intensities and profile shapes of the visible and ultraviolet returns. The cross section difference for Rayleigh and Mie scattering at the two wavelengths provides a sensitive indicator of the presence of aerosols. Generally, the aerosol contributions are not detected above 28 km. A comparison of the visible and ultraviolet profiles is shown in the data analysis section of this report (see Section 5.1).

The errors expected in the meteorological data are summarized in Table 4. The density error in the lidar profile resulting from the combination of rawinsonde accuracy and the tie-on procedures is

19

estimated to be less than 3 percent in all cases. On specific nights, the measurements can be used to argue that the stability of the atmosphere and the performance of the instrument would support conclusions of an accuracy approaching 2 percent. The statistical accuracy based upon the photon counting measurements adds to the error at higher altitudes. One additional source of error in the rawinsonde data is the fact that pressure heights only were used in the analysis since no radar track was available.

4.2   Datasonde

Ten datasonde payloads were launched on Super-Loki motors to provide measurements in the 20 to 65 km region during the lidar operations. Nine profiles were obtained. The Dart payload expels a metallized mylar parachute near an apogee of 75-80 km. The payload consists of a miniature bead thermistor, small telemetry transmitter, and parachute. Figures 9a through 9d show the payload configuration, parachute, and bead thermistor arrangement respectively. Radar tracking of the parachute can be used to determine the horizontal wind velocity. The bead thermistor signal which is transmitted to ground provides a temperature measurement from about 65 km (nighttime) down to the vicinity of 20 km. By using a measured pressure at lower altitudes from a rawinsonde profile, the density and pressure can be derived from the bead thermistor temperature under the assumption of hydrostatic equilibrium. The errors expected in this measurement are shown in Table 4.

4.3   Passive Sphere

Ten passive sphere payloads were launched on Super Loki motors and useful results were obtained in eight cases. The passive sphere payload provides a technique that can measure the horizontal wind velocity and density from radar tracking data. The payload consists of a 1 meter diameter metallized mylar sphere that is ejected from a Dart near apogee (95 km) and immediately inflates to a spherical radar target. Figure 10 shows the passive sphere payload configuration. The radar track of the horizontal motion provides a measure of the horizontal wind field and the vertical acceleration provides a measure of the atmospheric density. The temperature can be obtained by integrating the density profile under the assumption of hydrostatic equilibrium. The accuracy of the passive sphere results depends strongly upon the accuracy of the tracking radar. The errors associated with the passive sphere results are shown in Table 4. The errors in this table are based upon the standard analysis filters applied to typical range radar results. In this particular case, the radar used is not typical and the noise in the radar data appears to be larger than normally expected. A heavier smoothing of the radar

data would probably be justified in this case. The actual error in the passive sphere results is probably slightly larger than indicated in the table.

4.4 Other Supporting Measurements

During the measurement periods in February and March, the MST Radar located at Poker Flat Alaska was run continuously by the University of Alaska. It is expected that some periods of overlapping data will be found. Most of the winter period does not produce useful data because of the low radar signal strength when the sun is shadowed from producing electrons in the D-Region. The opportunities for data collection are during periods of particle precipitation into the mesosphere as indicated by the increase in riometer absorption. The MST data base is being examined by scientists at the University of Alaska to find periods for a comparison study.

Also, during the campaign period, scientists from Utah State University obtained data on the atmospheric temperature in the 85 km altitude region from measurements of the OH vibrational rotational band of the infrared emission at 1.5 μ. A comparison study of OH temperature data on wave activity with the lidar results is planned.
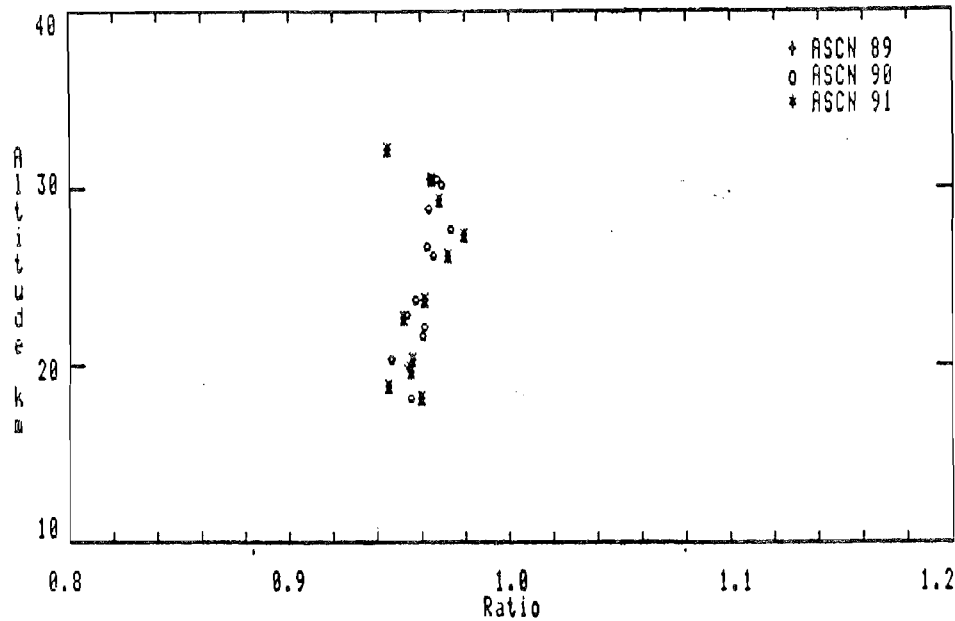
Figure 8. Example of the Rawinsonde Data Gathered on Each Day of the Measurement Period. The three profiles were obtained at 0000, 0600 and 1200 Z on each day. The 0600 balloon was usually chosen for the lidar profile tie-on at an altitude between 28 and 32 km. The results show the actual measured points for the altitudes above 18 km from ascents on 14 February 1986 from the Fairbanks NOAA station.

21

Table 4. Measurement accuracy of atmospheric density for the standard meteorological techniques (Source A - Range Commanders Council Document 110-81 "Meteorological Data Error Estimates" & Source B - AFGL-TR-78-0195 "Atmospheric Properties From Measurements at Kwajalein Atoll on 5 April 1978").

Altitude (km)	Rawinsonde A (%)	Rawinsonde B (%)	Datasonde A (%)	Datasonde B (%)	Sphere A (%)	Sphere B (%)
10	0.6	0.20	-	-	-	-
20	1.0	0.30	-	0.3	-	-
30	1.5	0.42	3.0	0.42	3.0	-
40	-	-	3.6	1.0	3.7	5.0
50	-	-	4.1	1.6	4.3	5.1
60	-	-	4.7	1.8*	5.0	5.4
70	-	-	-	3.0*	5.7	6.5
80	-	-	-	-	6.3	6.3
90	-	-	-	-	7.0	10.7

* Night time value (radiation corrections cause large errors in the day measurements)

Datasonde Dart	Weights
Dart Hardware (kg)	4.04
Parachute (kg)	0.154
Instrument (kg)	0.040
Complete Dart (kg)	4.53
Booster Rocket Motor (kg)	22.68
(kg)
Interstage (kg)	3.06

Rocket Motor Without Interstage Characteristics

Length (cm)	200.33
Diameter (cm)	10.16
Inert Weight (kg)	5.90
Propellant Weight (kg)	17.01

114.60 cm

OGIVE, INSTRUMENTATION AND PARACHUTE

3.92 cm Dia. with thermolag ablative coating

FIN SPAN 11.71 cm

140.72 cm VEHICLE BURNOUT Center of Gravity

321.31 cm

186.18 cm VEHICLE LAUNCH Center of Gravity

10.16 cm

SUPER LOKI ROCKET MOTOR

Complete Launch Weight (kg)   30.27

FIN SPAN 20.32 cm

NOSE ASSEMBLY

ABLATIVE COATING

INSTRUMENT, METEOROLOGICAL

STAVES, INSTRUMENT

STAVES, STARUTE

PISTON

PARACHUTE, STARUTE

DART BODY

ABLATIVE COATING

Payload Ejection Time (Seconds)   (120)

Figure 9.   Datasonde Payload.   (a) Super-Loki launch vehicle; (b) Datasonde separation from launch vehicle at apogee.

23

Descent System Characteristics

Parachute Type	Ram-air inflated
Canopy Material	1/4 mil mylar
Flying Width (m)	1.3
Flying Area (m²)	4.55
Parachute Weight (grams)	155
Parachute-Sonde Ballistic Coefficient (kg/m²)	.146
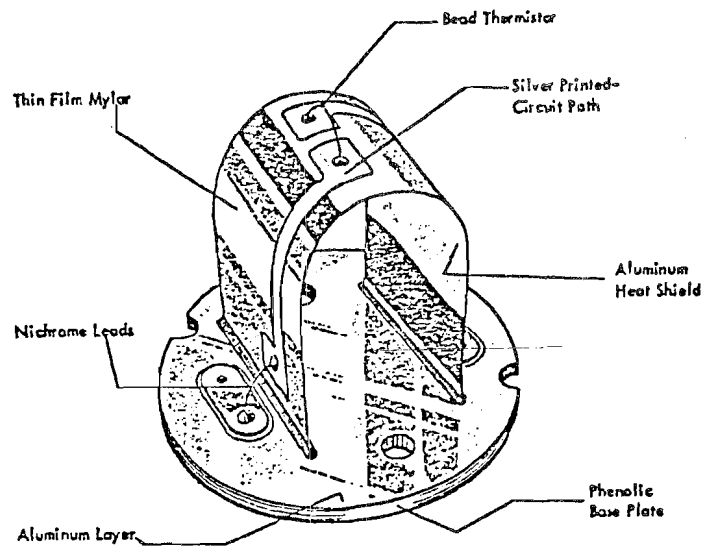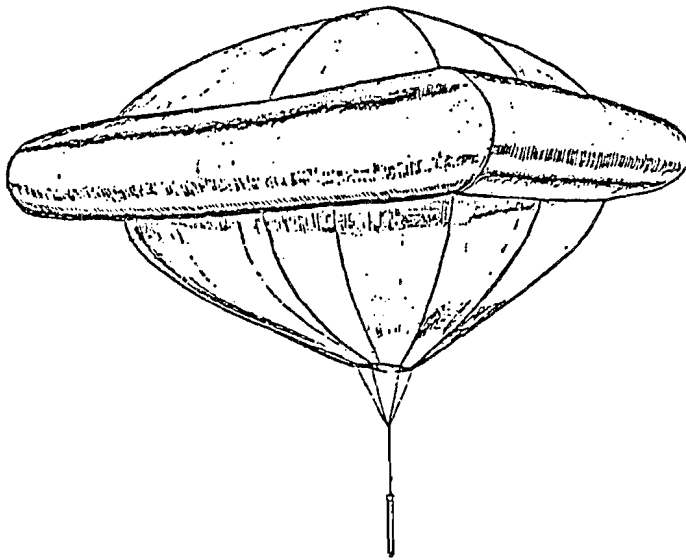
Figure 9.   Datasonde Payload.   (c) Parachute of metallized mylar that is tracked for a wind profile; (d) Bead thermistor that measures the ambient temperature.

Super-Loki Sphere

	Weights
Dart Hardware	5.954 kg
Sphere System	.168 kg
Complete Dart	6.122 kg

4.128 cm

110.88 cm

SPHERE PAYLOAD

10.16 cm

SUPER LOKI MOTOR

204.08 cm

Figure 10. Payload and Launch Vehicle for the Passive Sphere. At apogee the 1 meter metallized mylar sphere is ejected and inflated. The data are the horizontal velocity and the vertical acceleration from the radar track, which are used to determine the wind velocity and the atmospheric density profiles.

25

5. MEASUREMENT RESULTS

Measurements were taken on all clear evenings between 14 February and 9 March, when the laser power supply failed. The repairs and tests were completed between 10 March and 22 March. The operations were halted between 25 March and 15 April since the range resources were committed to other programs for that period. The nights of 27 and 28 April provided an opportunity for a concentrated set of measurements together with meteorological rocket launches. Table 5 summarizes the information on the number of lidar profiles which were obtained on each night. Table 6 summarizes the meteorological rocket launchings which were carried out during the campaign.

The LeCroy 3500 multichannel scaler is used to collect the return photon count signal in range bins set for 2 μsec intervals. The data system can accumulate the data in two counters simultaneously (however the actual timing relationship between the channels of the two scalers is offset by 1 μsec). A listing of an individual data run is shown in Table 7. Channel 0 provides the count of the number of measurement triggers (laser shots) included in the data set. However, the channel 0 also accumulates a signal from the sky background light as do the next channels. Thus it seldom reads the value of exactly 3,000 shots that were accumulated in most of the data runs. Channels 1 though 414 provide information on the sky background count rate. Channel 415 shows a large count rate due to the laser firing, principally noise pickup fro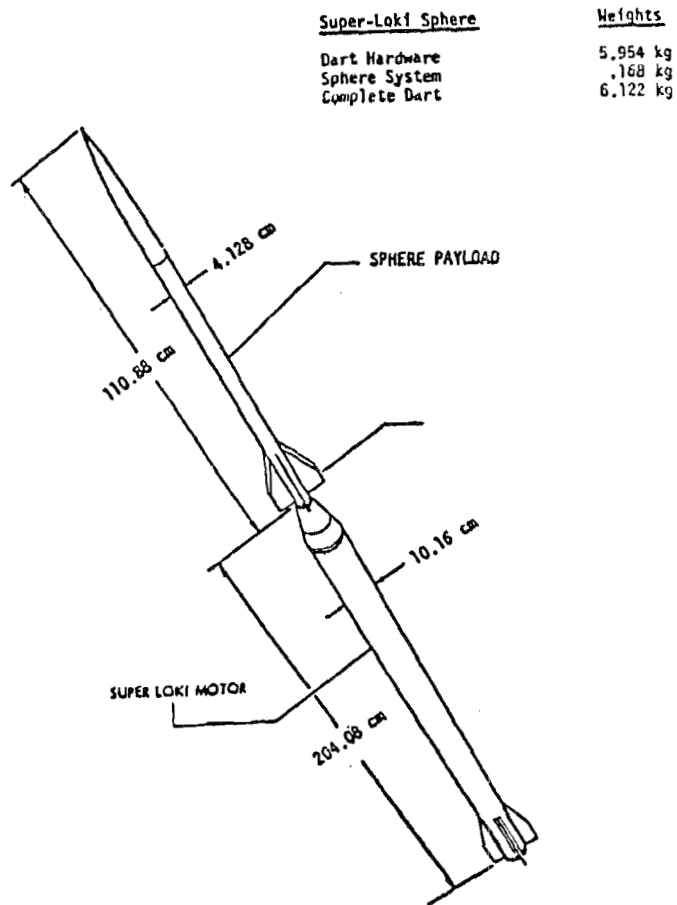m the Pockels cell. The beginning of the shutter opening is observed to start near channel 460. The shutter was fully open by channel 565 and the maximum count rate is observed near channel 480 because of the combined effect of the exponentially decreasing atmospheric density and the rapidly opening shutter. Channels beyond 800 are used to store the frequency that is generated from a photodiode signal in the energy monitor and provides a relative measure of the laser output energy.

One channel of the LeCroy system was always used for the output of the green detector on the 32 cm telescope. The second channel could be used to make measurements either from the ultraviolet channel of the 32 cm telescope or the green detector on the 62 cm telescope. The general measurement philosophy was to obtain three or four sets of ultraviolet profiles on each night and use the multi-channel scaler for the green channel on the 62 cm telescope for most of the nighttime measuring period.

Sky background from starlight, moonlight and other scattered light sources produce a limiting signal in the detector. The counts accumulated in data channels 1-399 (see Table 7) provide a measure of this background signal. This is used in the analysis to correct the results.

26

Table 5. Summary of Lidar Measurement Periods

DATE(Z)	START	END	GREEN	UV	HIGH ALT	COMMENTS
14 FEB	0405	1235	60	7	53	Datasonde & Sphere
15 FEB	0413	1232	61	8	53	Sphere
16 FEB	0508	1259	53	9	44	Sphere
17 FEB	0356	0910	34	5	29	Sphere
18 FEB	0500	1121	35	2	33	
19 FEB	0617	1449	40	3	37	
21 FEB	0450	1003	22	3	19	Overcast at 1000Z
22 FEB	0501	1400	62	3	59	
23 FEB	0511	0830	7	3	4	Overcast at 0630Z
24 FEB	0425	1356	70	7	63	Hazy/Full Moon
26 FEB	0525	0640	4	4	0	Clouds
27 FEB	0935	1448	39	6	33	
2 MAR	0437	1401	54	6	48	
3 MAR	0525	1301	57	8	49	
4 MAR	0516	1151	55	4	51	
5 MAR	0516	1351	64	8	56	
6 MAR	0607	1342	67	8	59	
7 MAR	0538	1337	76	8	68	
8 MAR	0529	1338	69	8	61	
9 MAR	0513	0630	12	4	8	Laser Failed
23 MAR	0700	1253	12	0	12	Laser Repaired
24 MAR	0611	0956	42	3	39	
16 APR	0914	1202	8	1	7	
24 APR	0856	1204	27	3	24	Clouds
26 APR	0549	0930	10	3	7	Clouds
27 APR	0623	1232	141*	6	135	2 Datasondes/5 Spheres
28 APR	0652	1223	152*	0	152	4 Datasondes
			1333	130	1203	

* Profiles of 1000 laser shots rather than 3000 shots

(1)   Total 2666 profiles (estimate 9 million laser firings)

(2)   Launched a total of 20 met rockets together with lidar measurements (17 flights were successful)

(3)   Rawinsonde balloon releases were made by the NOAA site at Fairbanks

(4)   MST radar measurements collected by the University of Alaska during all lidar measurement periods until 22 April

(5)   Mesospheric OH temperature measurements were obtained by Utah State University during the Lidar measurement periods of February and March

Table 6. Summary of the Meteorological Rocket Launches at Poker Flat Rocket
Range Alaska During February - April 1986

L1D 14 FEB (Z)   Datasonde #1   Wallops #DM1-1399
     0600Z   Sonde 26536
                    Good TM and radar data

L2S 14 FEB (Z)   Sphere #1   Wallops #DM1-1409
     0800Z   Sphere 4518   152.8g
                    Good data track, collapse 32 km, apogee 88 km, no upleg track

L3S 15 FEB (Z)   Sphere #2   Wallops #DM1-1410
     0600Z   Sphere 4566   151.7g
                    Good data track, collapse 33 km, apogee 90 km, no upleg track

L4S 16 FEB (Z)   Sphere #3   Wallops #DM1-1411
     0609Z   Sphere 3996   159.3g
                    No track

L5S 17 FEB (Z)   Sphere #4   Wallops #DM1-1412
     0600Z   Sphere 2420   162.9g
                    Upleg track, flight to left, no data, booster found near Chatanika Lodge

          (Moved launch tube to the rail on pad 1)

L6D 5 MAR (Z)   Datasonde #2   Wallops #DM1-1400
     1200Z   Sonde 26537
                    No radar track, TM track shows its flight path was toward right, Sonde
                    separated from starute, no data

(Disassembled datasondes and added 50 lb test fishing line to the shroud line --- shim and firmly mount
launch rail on pad 1)

L7D 6 MAR (Z)   Datasonde #3   Wallops #DM1-1401
     1220Z   Sonde 26539
                    Good radar and TM date, upleg radar track

L8S 8 MAR (Z)   Sphere #5   Wallops #DM1-1413
     1200Z   Sphere 4567   153.1g
                    Good track, collapse <35 km, good upleg radar track

L9S 9 MAR (Z)   Sphere #6   Wallops #DM1-1414
     0600Z   Sphere 3971   158.2g
                    Good track, collapse 32 km, good upleg radar track

L10D 27 APR (Z)   Datasonde #4(1)   Wallops #DM1-1403
     0730Z   Sonde 26538
                    Good radar and TM data

28

Table 6. (continued) Summary of the Meteorological Rocket Launches at Poker Flat Rocket Range Alaska During February - April 1986

L11S	27 APR (Z) 0810Z	Sphere #7(1) Sphere 3993 Good radar data	Wallops #DM1-1415 159.4 g
L12S	27 APR (Z) 0850Z	Sphere #8(2) Sphere 4509 Good radar data	Wallops #DM1-1416 153.7g
L13S	27 APR (Z) 0930Z	Sphere #9(3) Sphere 2421 Good radar data	Wallops #DM1-1417 163.1g
L14S	27 APR (Z) 1010Z	Sphere #10(4) Sphere 2416 Good radar data	Wallops #DM1-1418 162.4g
L15S	27 APR (Z) 1050Z	Sphere #11(5) Sphere 2417 Good radar data	Wallops #DM1-1419 161.8g
L16D	27 APR (Z) 1135Z	Datasonde #5(2) Sonde 26540 Good TM and radar data	Wallops #DM1-1402
L17D	28 APR (Z) 0730Z	Datasonde #6(3) Sonde 26596 Good TM and radar data	Wallops #DM1-1404
L18D	28 APR (Z) 0840Z	Datasonde #7(4) Sonde 26597 Good TM and radar data	Wallops #DM1-1405
L19D	28 APR (Z) 0950Z	Datasonde #8(5) Sonde 26541 Good TM and radar data	Wallops #DM1-1406
L20D	28 APR (Z) 1112Z	Datasonde #9(6) Sonde 26543 Good TM and radar data	Wallops #DM1-1407

29

Table 7. Data File List From a Typical Run, G6021407.

Channel				Counts Per Bin		
0	3005	7	7	3	9	Begin
5	5	3	5	5	0	Sky
10	1	2	1	2	4	Background
15	7	4	3	9	5	Measurement
20	5	4	6	4	10	
25	5	5	6	5	4	
30	7	10	6	7	2	
35	5	5	3	6	5	
40	3	2	6	3	5	
45	1	3	1	2	6	
50	3	6	4	5	5	
55	2	7	6	4	7	
60	2	3	8	4	6	
65	8	7	6	5	5	
70	6	4	6	4	4	
75	5	9	3	10	6	
80	4	7	3	3	5	
85	7	8	8	6	3	
90	2	4	4	6	6	
95	3	8	5	6	6	
100	9	5	4	4	2	
105	1	5	0	5	7	
110	8	4	5	3	5	
115	8	4	9	4	5	
120	4	7	2	6	4	
125	3	2	6	9	5	
130	5	11	4	6	2	
135	8	4	6	7	6	
140	4	4	3	5	10	
145	5	3	6	4	9	
150	6	6	6	5	3	
155	4	4	8	9	3	
160	2	5	7	0	8	
165	4	4	4	7	11	
170	5	5	2	8	4	
175	5	2	6	7	6	
180	6	6	9	6	6	
185	11	4	2	5	2	
190	8	8	6	5	9	
195	6	5	8	3	2	
200	6	5	6	7	5	
205	1	2	12	4	5	
210	5	1	5	2	6	
215	7	0	9	3	6	
220	5	3	4	5	3	
225	6	7	4	4	3	
230	3	3	6	3	4	
235	4	3	4	4	7	

Table 7. Data File List From a Typical Run, G6021407 (continued.)

Channel			Counts Per Bin			
240	6	8	5	3	3	
245	5	6	1	5	2	
250	10	2	3	3	6	
255	1	7	4	5	9	
260	3	9	6	6	6	
265	3	6	2	3	4	
270	4	1	8	5	2	
275	10	5	5	1	4	
280	8	4	3	8	3	
285	5	5	0	4	6	
290	3	2	5	6	6	
295	7	4	7	7	9	
300	3	3	5	5	5	
305	4	4	3	6	6	
310	3	6	8	6	2	
315	7	9	3	5	13	
320	11	10	13	11	10	
325	9	11	8	7	10	
330	12	7	8	13	9	
335	13	8	8	4	10	
340	9	4	16	4	8	
345	3	6	10	9	5	
350	11	5	6	12	9	
355	9	6	7	4	10	
360	4	6	4	9	8	
365	4	10	7	8	7	
370	7	7	11	7	5	
375	9	7	10	7	3	End
380	12	6	11	6	5	Sky
385	4	6	8	10	10	Background
390	8	8	6	9	6	Measurement
395	7	6	5	5	6	
400	29	0	0	0	0	Begin
405	0	1	0	0	0	Lidar
410	0	2	0	0	0	Profile
415	31302	811	339	189	101	--Laser Fire
420	77	56	43	23	30	
425	18	13	11	15	16	
430	8	15	13	11	14	
435	10	10	5	6	5	
440	15	12	13	16	14	
445	27	24	30	32	76	10 km
450	38	41	66	73	73	
455	78	64	87	77	101	
460	120	121	194	590	1380	
465	2668	4174	5738	7282	8518	
470	9942	11089	12360	13034	13543	
475	13911	14386	14482	15130	15542	

Table 7. Data File List From a Typical Run, G6021407 (continued.)

Channel				Counts Per Bin	
480	15758	16020	16288	16017	15043 20 km
485	14725	14879	14867	14683	14516
490	14792	14405	14035	13801	13538
495	13086	12138	11951	11850	11698
500	10496	9853	9672	9210	9165
505	8666	8064	7699	7413	7012
510	6657	6300	5906	5589	5338
515	5261	5038	4747	4388	4230 30 km
520	4008	3816	3657	3638	3221
525	3175	3113	2887	2765	2606
530	2491	2221	2197	2080	1979
535	1952	1839	1721	1647	1562
540	1544	1395	1362	1267	1157
545	1140	1037	1028	929	899 40 km
550	809	804	771	702	670
555	622	597	576	501	480
560	450	442	433	376	340
565	293	298	279	280	255
570	245	243	198	218	187
575	193	172	178	176	154
580	155	133	135	136	132 50 km
585	106	123	96	90	94
590	96	80	83	77	66
595	63	61	49	55	46
600	55	41	44	37	43
605	31	36	27	40	28
610	23	40	17	33	23
615	22	33	23	18	17 60 km
620	18	14	16	8	17
625	13	15	10	15	11
630	12	9	11	8	8
635	7	9	4	8	7
640	8	9	12	5	2
645	7	5	8	6	7 70 km
650	3	4	9	2	6
655	5	6	7	3	3
660	3	5	2	2	5
665	2	1	2	0	2
670	2	2	4	0	0
675	2	1	2	3	3
680	1	1	1	2	1 80 km
685	0	1	3	3	1
690	1	0	1	0	0
695	3	1	1	0	2
700	0	1	0	0	2
705	0	0	1	1	0
710	0	0	0	3	0
715	0	1	0	1	0 90 km

32

Table 7. Data File List From a Typical Run, G6021407 (continued.)

Channel			Counts Per Bin			
720	1	0	0	1	0	
725	1	0	1	0	0	
730	1	3	2	0	0	
735	0	0	0	1	0	
740	0	2	0	1	1	
745	2	0	0	1	0	100 km
750	0	0	0	0	1	
755	0	1	0	0	0	
760	0	0	0	1	0	
765	0	0	0	1	0	
770	0	0	0	0	0	
775	0	1	0	1	0	End
780	0	0	0	0	0	Lidar
785	1	0	2	0	1	Profile
790	1	2	0	1	0	Measurement
795	1	0	1	3	0	
800	1568	1190	1177	1151	1195	Begin
805	1152	1185	1164	1142	1213	Energy
810	1154	1175	1177	1119	1236	Monitor
815	1152	1150	1191	1148	1192	Measurement
820	1166	1153	1182	1149	1181	
825	1177	1184	1155	1174	1164	
830	1166	1182	1160	1174	1172	
835	1152	1198	1183	1140	1199	
840	1146	1173	1172	1151	1212	
845	1131	1167	1191	1144	1209	
850	1142	1157	1198	1182	1149	
855	1151	1173	1182	1198	1125	
860	1176	1183	1159	1207	1136	
865	1175	1194	1138	1191	1156	
870	1166	1198	1133	1193	1176	
875	1147	1194	1138	1177	1195	
880	1157	1174	1179	1137	1210	
885	1152	1174	1166	1153	1198	
890	1162	1173	1181	1131	1207	
895	1160	1136	1210	1150	1235	
900	1180	1145	1183	1151	1197	
905	1189	1127	1186	1160	1175	
910	1194	1141	1186	1160	1159	
915	1201	1163	1166	1175	1153	
920	1196	1154	1167	1184	1154	
925	1186	1153	1155	1198	1158	
930	1194	1136	1165	1201	1137	
935	1196	1155	1167	1186	1146	
940	1199	1173	1159	1166	1163	
945	1176	1190	1154	1181	1155	
950	1172	1188	1139	1178	1178	
955	1173	1156	1185	1154	1194	

Table 7. Data File List From a Typical Run, G6021407 (continued.)

Channel				Counts Per Bin	
960	1155	1177	1160	1161	1187
965	1165	1167	1177	1154	1193
970	1162	1162	1193	1138	1192
975	1167	1151	1196	1143	1173
980	1182	1154	1181	1168	1177
985	1167	1152	1191	1171	1157
990	1189	1149	1191	1163	1172
995	1168	1170	1164	1183	1175
1000	1156	1177	1158	1162	1202
1005	1141	1184	1157	1160	1194
1010	1150	1189	1159	1175	1177
1015	1145	1182	1169	1155	1197
1020	1164	1174	1194	1126	0

6. DATA ANALYSIS APPROACH

The primary data from the lidar consists of photon counts measured by the photomultiplier tubes, which are accumulated into channels of the multichannel scaler and later transferred to floppy discs for storage at the end of a data run. The data was collected as 2 μsec channel widths, representing 300 m range bins. Two data inputs were simultaneously measured, usually the 532 nm return measured by the detectors on the 32 cm telescope and 62 cm telescope. The input from the 62 cm telescope was changed to measure the ultraviolet signal (355 nm) for several data runs (typically 3 to 5) on each night. The data accumulated in the multichannel scalers for a fixed time period (usually 3,000 laser shots or 5 minutes) was transferred to an 8-inch floppy disc at the end of each data run. The LeCroy 3500 system uses a version of CPM for an operating system. Because of limitations in the hardware and software, a rather cumbersome procedure of transferring the data from a compressed format on SSDD 8 inch floppy discs to a permanent storage record as ASCII files on 5.25 inch floppy disks was necessary. The transfer procedure took almost as much time as the original data runs. Therefore, a semi-automatic procedure was devised to allow transfer of the data files during crew rest periods. The difficulties in handling the data have been addressed so that we will be able to store and use the data in near real time for the next measurement period.

Data files in ASCII format which contain the information on the backscatter photons, the laser energy monitor, and the sky background count rate provide the data input for the analysis procedures. The analysis is carried out using a program written in BASIC which has evolved through more than twenty-five versions and updates since the beginning of its development in July 1985. Development of the analysis program in the BASIC programming language proved to be a great advantage in the processes of the interactive development of the analysis program. Several individuals contributed to the development of the analysis program, which evolved significantly during the field program. The current program used to analyze this data set has evolved from the program developed during the field measurement program. The major point which has been added is the capability for editing the data, processing multiple data files, and significantly improved displays with plots. The programs have also been transferred into the more powerful Pascal language. In addition, examination of the data revealed that there were problems involving the drift of the synchronous motors that rotated the shutter wheels in the detectors of both the 32 and 62 cm telescopes. Additional analysis procedures have been developed to account for these errors created by the shutter. It should be noted that these problems appear to be resolvable in this data set and can be avoided in the future by using a crystal controlled power source for the motor and by providing improved EMI suppression.

6.1. Outline of Data Reduction

The general outline for the analysis is as follows:

A.   Load the following files with the analysis program:

    a.   ASCII data files - the data base;

    b.   GPAR.BAS - A parameter file for processing the 532 nm return of the 32 cm telescope;

    c.   HPAR.BAS - A parameter file for the 532 nm data of the high altitude (62 cm) telescope;

    d.   SUMG - An ASCII list of the data files where the run time and date are added to the file from the data log;

    e.   Shutter file - A listing of the shutter function, which is derived from the white light calibration curves and smoothed using a mathematical function derived from the shutter geometry;

    f.   USSA7690 - A data file which provides the density profile of the US Standard Atmosphere at the altitude intervals of the lidar range bins,

    g.   Calibration file - The calibration file for each night was based upon the NOAA Rawinsonde measurement for each night that the lidar was operated;

    h.   DATA98 - An effective shutter file for the high altitude detector (this file will be modified to provide a correction for the shutter drift when that analysis is complete).

B.   Run a program called FILTNEW to create a run file, RUNXXXX, which eliminates data runs with obvious errors. Here XXXX represents the data date.

C.   Run a program called EDITDATA to generate an edited file, EDITXXXX.

D.   Run a program called RAWSHFT to calculate the shutter drift error in the 32 cm telescope detector and record the shift correction as SHFTXXXX.

E.   Run a program called SHIFTADD to create an additional column to the run file, RUNXXXX.

F.   Run the main data analysis program, D320, to generate density data files *.DEN for all data files contained in the data file list RUNXXXX.

G.   Run COMBOH2 to produce a file with combined raw data which has been accumulated into one-hour periods for each GMT hour.

H.   Run RAWSHFT to create a file SHFTHXXX which calculates the shutter bias for the one-hour period.

I.   Run a program called SHIFTADD to generate a run file RUNHXXXX which contains a column for the shift of the shutter for the one-hour data.

J.   Run the main data analysis program, D320, to create density data files GH*.DEN and HH*.DEN which are mean profiles for each one-hour period.

K. Run a program called COMBOF2 to create a run file for the full night, RUNFXXXX.

L. Run a program called RAWSHFT to create a file, SHFTFXXX, which is the shift for the 32 cm telescope shutter for analysis of the full night data.

M. Run a program called SHIFTADD to add the shift for 32 cm telescope detector to RUNFXXXX.

N. Run the analysis program, D320F, to create the full night mean density profiles GF*.DEN and HF*.DEN.

The procedure results in a data set that includes profiles for each individual data run as well as profiles for each hour in which the lidar was operated and a summary mean profile for the night. The main elements of the data analysis program are summarized in Table 8. The labels used to identify the data run and results files are shown in Table 9. A typical data file output from the analysis program is given in Table 10. The full night summary data plots are in Appendix C.

Table 8. Outline of the Data Analysis Program

_____

Program D320.BAS

Mobile Lidar Density Reduction

Input Data

Lidar site altitude in km

Calibration altitude range in km

Output Density in kg/m^3

Model Density in cm^{-3}

S1	=	Top Thumbwheel Switch Setting (Max Range)
S2	=	Second Switch Setting (Min Range)
S3	=	Third Switch Setting (Laser Fire Timing)
S4	=	Bottom Switch Setting (Flash Lamp Fire Timing)
ITIME0	=	# Channels from Start of Data Block to Laser Firing
ISHFT	=	# Channels from Start of Data Block to Start of Useful Data
ZM,TM,DM	=	Model Altitude, Temperature, Density
DMX	=	Model Density Shifted to Correspond to Data
ZC,CDENS	=	Calibration Model Altitude, Density
DCX	=	Calibration Model Density Shifted
SIGMA	=	SQRT(Counts+1)
TEMP	=	Smoothed Density from Raised Cosine Routine

Preliminaries

Setup and Dimension all Arrays
Input Constants, r, Gas Constant, Altitude of Trailer, Size of Altitude Bins
Input Length of Smoothing Intervals to use

Parameter Input

Input from Gpar and Hpar Files
    Check Flags in run File (Flags were set by the Filter Program to Remove Bad Data Files)

Data Input

Separate the Data in the File into Profile Counts, Sky Background Counts, and Energy Monitor Counts

38

Table 8. Outline of the Data Analysis Program (continued)

_____

Calculations

    Range for each Data Bin

    Altitude Corresponding to each Data Bin

    Sky Background Intensity

    Signal to Noise Ratio

        Shift Shutter

            Shift Data to Correspond to Selected Starting Point

            Shutter, Background, 1/R and Deadtime Corrections

            Normalize Lidar Data to Comparison Density Array

    Smooth Profile

    Store Final Profile on Disk with Header Data

Plot Data and Model

Subroutines

    Smoothing Routine Determine the Smoothing Interval to Apply as Signal Level Changes with Altitude

    Raised Cosine Smoothing (Hanning filter)

    File Reading Subroutine

    Density Plot Subroutine

    Edit Single Data Points Outside of 4 Sigma

    Screen Dump Routine

    Subroutine Makecal   (Makes a Calibration File from a Green Data File for Normalization of High Altitude (H) File)

    Plotting Routines

Table 9. Example of the File Label Approach Chosen to Identify the Data Run and Results Files.

Example

G6021401.DEN

          (Blank) = Raw Data File
          Den = Density Profile

          Run Number[*]

          Day (GMT)

          Month

          6 = Year 1986
          H = Hour Mean (Run = Hour)
          F = Full Night Mean

          G = Green - 32 CM Telescope
          U = UV Data 32 CM Telescope
          H = Green - 62 CM Telescope
          W = Sky Light Calibration

[*] If the Run Number Exceeds 80 then Add 30 to the Date

Table 10. List of a Typical Density File Output From the Data Analysis Program.

G6021446.DEN   860214   1001 UTC   Version   3.20 (86 NOV 24)
Shutter File S6021301.FIT   Model File USSA7690.DAT   Filter Level 2
Calibration File R021490.DAT   Calibration Altitudes 30 km to 32 km
Site Altitude 0.393 km   Elevation Angle 90.0   Deadtime 25.0 nsec
Background 0.28 Energy 1080.3

#	Altitude km	Raw Density	Filtered Density	Ratio To Model	Sigma	NF	Temp K	S/N Ratio
1	16.432	6.848284E-02	6.848284E-02	0.440224	0.011818	0	-999.9	93.8
2	16.732	7.427377E-02	7.427377E-02	0.500440	0.010665	0	-999.9	101.2
3	17.032	7.999128E-02	7.999128E-02	0.564913	0.009879	0	-999.9	107.8
4	17.331	8.351486E-02	8.351486E-02	0.618191	0.009274	0	-999.9	111.7
5	17.631	8.528198E-02	8.528198E-02	0.661659	0.008950	0	-999.9	114.7
6	17.931	8.652426E-02	8.652426E-02	0.703608	0.008718	0	-999.9	118.0
7	18.231	8.671306E-02	8.671306E-02	0.739081	0.008474	0	-999.9	120.2
8	18.531	8.659356E-02	8.659356E-02	0.773581	0.008323	0	-999.9	122.5
9	18.830	8.622703E-02	8.622703E-02	0.807373	0.008166	0	-999.9	124.5
10	19.130	8.570483E-02	8.570483E-02	0.841094	0.008032	0	-999.9	126.4
11	19.430	8.474816E-02	8.474816E-02	0.871719	0.007912	0	-999.9	127.6
12	19.730	8.332837E-02	8.332837E-02	0.898346	0.007834	0	-999.9	128.4
13	20.030	8.311348E-02	8.311348E-02	0.939129	0.007788	0	-999.9	131.2
14	20.329	8.289859E-02	8.289859E-02	0.982927	0.007624	0	-999.9	128.9
15	20.629	7.739726E-02	7.739726E-02	0.963066	0.007759	0	-999.9	126.3
16	20.929	7.271138E-02	7.271138E-02	0.949417	0.007918	0	-999.9	124.7
17	21.229	7.063090E-02	7.063090E-02	0.967709	0.008018	0	-999.9	126.8
18	21.529	6.855042E-02	6.855042E-02	0.985428	0.007889	0	-999.9	126.0
19	21.828	6.601489E-02	6.601489E-02	0.995612	0.007934	0	-999.9	127.0
20	22.128	6.629151E-02	6.629151E-02	1.048845	0.007875	0	-999.9	129.4
21	22.428	6.436563E-02	6.436563E-02	1.068268	0.007729	0	-999.9	126.9
22	22.728	6.201005E-02	6.201005E-02	1.079522	0.007882	0	-999.9	125.4
23	23.028	6.011090E-02	6.011090E-02	1.097576	0.007975	0	-999.9	125.0
24	23.327	5.785159E-02	5.785159E-02	1.107850	0.007998	0	-999.9	123.3
25	23.627	5.561706E-02	5.561706E-02	1.116930	0.008110	0	-999.9	121.8
26	23.927	5.253495E-02	5.253495E-02	1.106346	0.008210	0	-999.9	118.2
27	24.227	5.004042E-02	5.004042E-02	1.104985	0.008460	0	-999.9	116.6
28	24.527	4.762360E-02	4.762360E-02	1.102611	0.008573	0	-999.9	114.4
29	24.826	4.549089E-02	4.549089E-02	1.104228	0.008739	0	-999.9	112.7
30	25.126	4.274489E-02	4.274489E-02	1.087738	0.008876	0	-999.9	108.8
31	25.426	4.140004E-02	4.140004E-02	1.104371	0.009189	0	-999.9	109.3
32	25.726	3.971906E-02	3.971906E-02	1.110603	0.009152	0	-999.9	106.9
33	26.026	3.788623E-02	3.788623E-02	1.110345	0.009353	0	-999.9	104.5
34	26.325	3.544039E-02	3.544039E-02	1.088588	0.009571	0	-999.9	100.4
35	26.625	3.355933E-02	3.355933E-02	1.080281	0.009963	0	-999.9	98.6

Table 10. List of a Typical Density File Output From the Data Analysis Program (continued.)

#	Altitude km	Raw Density	Filtered Density	Ratio To Model	Sigma	NF	Temp K	S/N Ratio
36	26.925	3.187614E-02	3.187433E-02	1.075212	0.007175	1	-999.9	96.5
37	27.225	3.018570E-02	3.019823E-02	1.067420	0.007331	1	-999.9	94.0
38	27.525	2.854538E-02	2.851377E-02	1.056041	0.007517	1	-999.9	91.6
39	27.824	2.677862E-02	2.677862E-02	1.039097	0.007731	1	-999.9	88.5
40	28.124	2.501187E-02	2.530364E-02	1.028643	0.007939	1	-999.9	87.6
41	28.424	2.441222E-02	2.423066E-02	1.031891	0.008104	1	-999.9	85.3
42	28.724	2.308635E-02	2.321772E-02	1.035729	0.008249	1	-999.9	84.7
43	29.023	2.228593E-02	2.216655E-02	1.035744	0.008389	1	-999.9	82.5
44	29.323	2.100798E-02	2.100798E-02	1.028108	0.008597	1	-999.9	79.2
45	29.623	1.973002E-02	1.984212E-02	1.016987	0.008876	1	-999.9	77.6
46	29.923	1.890044E-02	1.873180E-02	1.005428	0.009150	1	-999.9	74.6
47	30.223	1.739628E-02	1.756718E-02	0.987387	0.009434	1	-999.9	72.9
48	30.522	1.657571E-02	1.657851E-02	0.975705	0.009694	1	-999.9	71.3
49	30.822	1.576633E-02	1.583900E-02	0.976025	0.009898	1	-999.9	70.3
50	31.122	1.524761E-02	1.509932E-02	0.974139	0.010111	1	-999.9	67.9
51	31.422	1.413570E-02	1.424965E-02	0.962439	0.010371	1	-999.9	66.6
52	31.722	1.347957E-02	1.341095E-02	0.948209	0.010659	1	-999.9	64.2
53	32.021	1.254896E-02	1.253690E-02	0.927860	0.010984	1	-999.9	62.5
54	32.321	1.157013E-02	1.164844E-02	0.903472	0.011352	1	-999.9	59.9
55	32.621	1.090455E-02	1.089527E-02	0.886425	0.011707	1	-999.9	59.2
56	32.921	1.020188E-02	1.025013E-02	0.874606	0.012004	1	-999.9	57.3
57	33.221	9.692216E-03	9.665290E-03	0.864771	0.012284	1	-999.9	56.5
58	33.520	9.074844E-03	9.107858E-03	0.854339	0.012584	1	-999.9	54.4
59	33.820	8.589527E-03	8.625980E-03	0.848153	0.010533	2	-999.9	53.5
60	34.120	8.172473E-03	8.168123E-03	0.841717	0.010784	2	-999.9	52.5
61	34.420	7.719486E-03	7.733989E-03	0.835125	0.011034	2	-999.9	51.0
62	34.720	7.325701E-03	7.302441E-03	0.826126	0.011304	2	-999.9	49.9
63	35.019	6.845876E-03	6.877652E-03	0.815033	0.011616	2	-999.9	48.0
64	35.319	6.457923E-03	6.467849E-03	0.802750	0.011953	2	-999.9	47.0
65	35.619	6.077970E-03	6.074558E-03	0.789492	0.012305	2	-999.9	45.6
66	35.919	5.685248E-03	5.704923E-03	0.776290	0.012678	2	-999.9	44.1
67	36.219	5.307428E-03	5.375436E-03	0.765698	0.013059	2	-999.9	42.6
68	36.518	5.103979E-03	5.083459E-03	0.757885	0.013409	2	-999.9	42.5
69	36.818	4.829875E-03	4.809529E-03	0.750373	0.013748	2	-999.9	41.0
70	37.118	4.488438E-03	4.543967E-03	0.741770	0.014123	2	-999.9	39.1
71	37.418	4.310166E-03	4.300233E-03	0.734375	0.014539	2	-999.9	39.0
72	37.718	4.049749E-03	4.086641E-03	0.729987	0.014936	2	-999.9	37.3
73	38.017	3.917686E-03	3.883321E-03	0.725448	0.015297	2	-999.9	37.3
74	38.317	3.668710E-03	3.680282E-03	0.718905	0.015711	2	-999.9	35.4
75	38.617	3.463570E-03	3.483493E-03	0.711418	0.016188	2	-999.9	34.5

Table 10. List of a Typical Density File Output From the Data Analysis Program (continued.)

#	Altitude km	Raw Density	Filtered Density	Ratio To Model	Sigma	NF	Temp K	S/N Ratio
76	38.917	3.295030E-03	3.300833E-03	0.704671	0.016685	2	-999.9	33.7
77	39.217	3.138728E-03	3.129635E-03	0.698303	0.017174	2	-999.9	32.8
78	39.516	2.954266E-03	2.963173E-03	0.690921	0.017686	2	-999.9	31.5
79	39.816	2.789256E-03	2.812521E-03	0.685209	0.015796	3	-999.9	30.5
80	40.116	2.662033E-03	2.665170E-03	0.678333	0.016300	3	-999.9	29.8
81	40.416	2.530329E-03	2.525382E-03	0.671386	0.016839	3	-999.9	28.8
82	40.716	2.389549E-03	2.394780E-03	0.664926	0.017409	3	-999.9	27.7
83	41.015	2.229710E-03	2.275977E-03	0.659893	0.017995	3	-999.9	26.4
84	41.315	2.166526E-03	2.171018E-03	0.657211	0.018571	3	-999.9	26.4
85	41.615	2.074933E-03	2.077099E-03	0.656405	0.019116	3	-999.9	25.4
86	41.915	1.999840E-03	1.988619E-03	0.655959	0.019651	3	-999.9	24.9
87	42.215	1.898645E-03	1.901788E-03	0.654690	0.020218	3	-999.9	23.9
88	42.514	1.796745E-03	1.815057E-03	0.652005	0.020834	3	-999.9	23.0
89	42.814	1.739929E-03	1.729974E-03	0.648375	0.021500	3	-999.9	22.8
90	43.114	1.660731E-03	1.650807E-03	0.645427	0.022193	3	-999.9	21.9
91	43.414	1.526928E-03	1.585823E-03	0.646712	0.018591	5	-999.9	20.4
92	43.714	1.523903E-03	1.516661E-03	0.645044	0.019145	5	-999.9	21.2
93	44.013	1.472778E-03	1.451587E-03	0.643768	0.019705	5	-999.9	20.4
94	44.313	1.380387E-03	1.390071E-03	0.642761	0.020272	5	-999.9	19.3
95	44.613	1.295344E-03	1.330993E-03	0.641587	0.020850	5	-999.9	18.5
96	44.913	1.286019E-03	1.273272E-03	0.639749	0.021453	5	-999.9	18.9
97	45.213	1.208439E-03	1.216099E-03	0.636807	0.022091	5	-999.9	17.7
98	45.512	1.186361E-03	1.159645E-03	0.632785	0.022774	5	-999.9	17.8
99	45.812	1.103112E-03	1.105088E-03	0.628295	0.023496	5	-999.9	16.6
100	46.112	1.015486E-03	1.053416E-03	0.623945	0.024236	5	-999.9	15.7
101	46.412	1.006343E-03	1.005642E-03	0.620457	0.024984	5	-999.9	16.2
102	46.711	9.367772E-04	9.623938E-04	0.618425	0.025721	5	-999.9	15.0
103	47.011	8.938958E-04	9.226888E-04	0.617446	0.026432	5	-999.9	14.8
104	47.311	9.076302E-04	8.849080E-04	0.616590	0.027142	5	-999.9	15.3
105	47.611	8.681974E-04	8.477927E-04	0.613412	0.027884	5	-999.9	14.4
106	47.911	8.354422E-04	8.105987E-04	0.608777	0.028680	5	-999.9	14.1
107	48.210	7.500697E-04	7.750792E-04	0.604209	0.025549	7	-999.9	12.7
108	48.510	7.052915E-04	7.399384E-04	0.598721	0.026304	7	-999.9	12.6
109	48.810	6.912209E-04	7.053186E-04	0.592379	0.027108	7	-999.9	12.7
110	49.110	6.840975E-04	6.712248E-04	0.585149	0.027961	7	-999.9	12.6
111	49.410	6.479687E-04	6.377592E-04	0.577082	0.028865	7	-999.9	11.9
112	49.709	6.030299E-04	6.053774E-04	0.568576	0.029820	7	-999.9	11.3
113	50.009	5.750933E-04	5.744311E-04	0.559990	0.030810	7	-999.9	11.1
114	50.309	5.397929E-04	5.451262E-04	0.551591	0.031826	7	-999.9	10.6
115	50.609	5.070391E-04	5.178362E-04	0.543863	0.032867	7	-999.9	10.2

43

Table 10. List of a Typical Density File Output From the Data Analysis Program (continued.)

#	Altitude km	Raw Density	Filtered Density	Ratio To Model	Sigma	NF	Temp K	S/N Ratio
116	50.909	4.682695E-04	4.931197E-04	0.537556	0.033925	7	-999.9	9.7
117	51.208	4.467874E-04	4.797323E-04	0.542805	0.030986	9	-999.9	9.6
118	51.508	4.268153E-04	4.610443E-04	0.540927	0.031864	9	-999.9	9.3
119	51.808	4.287044E-04	4.445905E-04	0.539808	0.032722	9	-999.9	9.5
120	52.108	4.105384E-04	4.301418E-04	0.540527	0.033542	9	-999.9	9.0
121	52.408	4.182992E-04	4.173174E-04	0.542803	0.034318	9	-999.9	9.4
122	52.707	4.260600E-04	4.057653E-04	0.546346	0.035051	9	-999.9	8.6
123	53.007	4.036335E-04	3.950268E-04	0.550656	0.035756	9	-999.9	8.8
124	53.307	3.812070E-04	3.846919E-04	0.555230	0.036445	9	-999.9	8.1
125	53.607	3.804676E-04	3.743453E-04	0.559480	0.037135	9	-999.9	8.6
126	53.907	3.797282E-04	3.636591E-04	0.562866	0.037847	9	-999.9	8.0
127	54.206	3.274511E-04	3.524566E-04	0.565015	0.038599	9	-999.9	8.3
128	54.506	3.570979E-04	3.405487E-04	0.565489	0.039412	9	-999.9	7.4
129	54.806	2.874929E-04	3.277862E-04	0.563862	0.040308	9	-999.9	8.2
130	55.106	3.544282E-04	3.142002E-04	0.559981	0.041302	9	-999.9	7.7
131	55.406	3.207210E-04	3.001092E-04	0.554216	0.042400	9	-999.9	7.2
132	55.705	2.807854E-04	2.857416E-04	0.546829	0.043611	9	-999.9	7.4
133	56.005	3.003044E-04	2.711937E-04	0.537881	0.044950	9	-999.9	6.5
134	56.305	2.314255E-04	2.566816E-04	0.527687	0.046419	9	-999.9	6.9
135	56.605	2.675596E-04	2.425366E-04	0.516872	0.048002	9	-999.9	6.1
136	56.905	2.080791E-04	2.289209E-04	0.505784	0.049684	9	-999.9	5.6
137	57.204	1.816559E-04	2.159423E-04	0.494697	0.051445	9	-999.9	5.2
138	57.504	1.546395E-04	2.038885E-04	0.484359	0.053250	9	-999.9	5.9
139	57.804	2.030571E-04	1.929426E-04	0.475362	0.055059	9	-999.9	6.1
140	58.104	2.229141E-04	1.833943E-04	0.468656	0.056805	9	-999.9	4.8
141	58.404	1.356634E-04	1.754583E-04	0.465119	0.058416	9	-999.9	5.4
142	58.703	1.732682E-04	1.689893E-04	0.464754	0.059872	9	-999.9	5.2
143	59.003	1.628636E-04	1.637731E-04	0.467338	0.061169	9	-999.9	5.4
144	59.303	1.768499E-04	1.593802E-04	0.471952	0.062354	9	-999.9	3.7
145	59.603	8.534727E-05	1.553611E-04	0.477457	0.063498	9	-999.9	5.3
146	59.903	1.741843E-04	1.513469E-04	0.482775	0.064671	9	-999.9	4.6
147	60.202	1.315128E-04	1.470809E-04	0.487035	0.065939	9	-999.9	4.8
148	60.502	1.456564E-04	1.425455E-04	0.490052	0.067317	9	-999.9	5.3
149	60.802	1.794891E-04	1.377303E-04	0.491650	0.068821	9	-999.9	5.1
150	61.102	1.681956E-04	1.325169E-04	0.491235	0.070498	9	-999.9	4.4
151	61.402	1.302353E-04	1.267498E-04	0.487990	0.072428	9	-999.9	4.3
152	61.701	1.248493E-04	1.205662E-04	0.482158	0.074625	9	-999.9	3.3
153	62.001	7.219917E-05	1.142346E-04	0.474587	0.077053	9	-999.9	3.8
154	62.301	1.001030E-04	1.078479E-04	0.465521	0.079722	9	-999.9	3.6
155	62.601	8.734297E-05	1.014087E-04	0.454850	0.082670	9	-999.9	4.2

44

Table 10. List of a Typical Density File Output From the Data Analysis Program (continued.)

#	Altitude km	Raw Density	Filtered Density	Ratio To Model	Sigma	NF	Temp K	S/N Ratio
156	62.901	1.228486E-04	9.511565E-05	0.443368	0.085850	9	-999.9	3.6
157	63.200	8.903480E-05	8.916207E-05	0.431986	0.089181	9	-999.9	2.8
158	63.500	6.162394E-05	8.359661E-05	0.421029	0.092630	9	-999.9	2.6
159	63.800	5.507797E-05	7.848315E-05	0.410950	0.096130	9	-999.9	3.7
160	64.100	9.880375E-05	7.370630E-05	0.401295	0.099729	9	-999.9	3.4
161	64.400	8.519852E-05	6.918055E-05	0.391695	0.103494	9	-999.9	3.4
162	64.699	8.599850E-05	6.489807E-05	0.382172	0.107451	9	-999.9	2.0
163	64.999	3.496572E-05	6.091775E-05	0.373157	0.111565	9	-999.9	2.4
164	65.299	5.023887E-05	5.749125E-05	0.366379	0.115566	9	-999.9	2.0
165	65.599	3.561774E-05	5.480027E-05	0.363371	0.119140	9	-999.9	2.4
166	65.898	5.117136E-05	5.291981E-05	0.365162	0.122024	9	-999.9	2.0
167	66.198	3.627580E-05	5.171078E-05	0.371371	0.124215	9	-999.9	2.2
168	66.498	4.435972E-05	5.096664E-05	0.381006	0.125867	9	-999.9	1.7
169	66.798	2.911683E-05	5.056536E-05	0.393532	0.127064	9	-999.9	3.4
170	67.098	9.253295E-05	5.039511E-05	0.408374	0.127898	9	-999.9	1.4
171	67.397	2.168012E-05	5.033647E-05	0.424772	0.128523	9	-999.9	3.3
172	67.697	8.616709E-05	5.014464E-05	0.440722	0.129287	9	-999.9	2.4
173	67.997	5.450261E-05	4.960009E-05	0.454101	0.130526	9	-999.9	2.4
174	68.297	5.498707E-05	4.872837E-05	0.464775	0.132266	9	-999.9	2.4
175	68.597	5.547368E-05	4.763301E-05	0.473396	0.134414	9	-999.9	1.4
176	68.896	2.266100E-05	4.630823E-05	0.479617	0.137018	9	-999.9	2.4
177	69.196	5.645333E-05	4.474765E-05	0.483050	0.140140	9	-999.9	1.0
178	69.496	1.458786E-05	4.301134E-05	0.484010	0.143750	9	-999.9	2.0
179	69.796	4.035061E-05	4.114918E-05	0.482779	0.147821	9	-999.9	2.4
180	70.096	5.793888E-05	3.919634E-05	0.479527	0.152330	9	-999.9	1.4
181	70.395	2.366358E-05	3.710224E-05	0.473387	0.157465	9	-999.9	2.2
182	70.695	5.017154E-05	3.491799E-05	0.464708	0.163255	9	-999.9	2.4
183	70.995	5.944374E-05	3.269643E-05	0.453955	0.169707	9	-999.9	1.7
184	71.295	3.319396E-05	3.041514E-05	0.440609	0.177076	9	-999.9	0.6
185	71.595	6.493508E-06	2.818157E-05	0.426036	0.185254	9	-999.9	1.4
186	71.894	2.468786E-05	2.609753E-05	0.411921	0.194038	9	-999.9	1.4
187	72.194	2.489532E-05	2.433037E-05	0.401309	0.202709	9	-999.9	0.6
188	72.494	6.658590E-06	2.296689E-05	0.395913	0.210526	9	-999.9	0.6
189	72.794	6.714079E-06	2.200170E-05	0.396435	0.216972	9	-999.9	1.0
190	73.094	1.614631E-05	2.140587E-05	0.403196	0.221638	9	-999.9	1.7
191	73.393	3.518801E-05	2.105784E-05	0.414684	0.224871	9	-999.9	0.6
192	73.693	6.881924E-06	2.095324E-05	0.431448	0.226560	9	-999.9	1.7
193	73.993	3.576842E-05	2.110880E-05	0.454532	0.226569	9	-999.9	1.4
194	74.293	2.637185E-05	2.132824E-05	0.480324	0.226146	9	-999.9	1.7
195	74.593	3.635358E-05	2.142598E-05	0.504719	0.226452	9	-999.9	1.4

45

6.2 Detector Shutter Function

The approach taken of using a mechanical shutter to act as a variable neutral density filter has taken a significant effort to implement properly. The problems are believed to be resolved and are not expected to affect the results in the future. The initial difficulty was due to additional light scattering that caused the primary image to be different than would be expected from the geometry of the arrangement. The problem was that the secondary mirror was slightly larger in diameter than was needed to transfer the light from the primary to the focus of the telescope, which allowed off axis light to be gathered in an annular ring around the primary image (see Figure 5). In addition, the baffle tube was shorter than needed and was not completely effective in removing grazing incidence scattering. Figure 5 indicates the arrangement of the telescope, shutter and the image at the shutter plane. The problems with the slightly larger secondary and the grazing incidence scattering would not normally affect a night-time viewing telescope, in fact astronomical telescopes should intentionally be sized in this way. However, because day sky white light calibrations of the shutter opening are needed to develop a functional representation of the shutter opening, any additional light scattering is critical. When these problems were noted, they were corrected by introducing a small mask around the secondary mirror that effectively reduces the secondary diameter by about 3 mm. This mask eliminates an annular path for off-axis double reflection through the optical system. A mechanical stop was used to eliminate grazing incidence scattering. When these changes were made, the image of the primary mirror at the plane of the shutter wheel changed to the conditions for the proper image shown in Figure 5. The bright ring around the image was eliminated. The representation of the image shows the primary mirror shadowed by both the secondary mirror and the spider that supports the secondary. When these changes were made, the white light calibration curves are reasonably represented by the mathematical function describing the geometry.

Figure 11 shows the shape of the shutter function obtained from a sky-background calibration. Since the larger dynamic range for the detector is obtained by accepting a fraction of the image of the primary mirror (the effect is of a variable neutral density filter), the signal removed by the shutter function must be accurately measured in order to reconstruct the low altitude portion of the profile. The "white light calibration" curve is obtained by opening the telescope to the day-sky background with a neutral density filter inserted in the detector path. The opening function of the shutter is then determined to a high statistical accuracy. As shown in Figure 11, the shutter is seen to start opening near channel 455, which corresponds to an altitude of about 12 km. The shutter is fully open by channel 565, which corresponds to an altitude of about 45 km. Examination of the region around channel 500 reveals the change in slope of the curve as the shadow of the secondary

mirror is passed. The shutter timing and careful handling of the relationship to the data become critical at the lower altitudes.

6.2.1 SHUTTER DRIFT ON 32 cm TELESCOPE

Because the time relationship between the laser firing and the opening of the shutter wheel is critical to within fractions of a microsecond, the shutter arrangement was designed carefully. However, the data were found to exhibit rather large (a few microseconds) variations in the timing for the shutter wheel over a period of several hours. Three factors have been found to have contributed to some degree to this problem. First, the power system grid for central Alaska experiences significant voltage and frequency drifts during the winter nights. Second, the capacitor originally supplied with the shutter motor was not the correct value and caused the motor to overheat. The capacitor was replaced in March. Third, The motor shaft bearings were worn and rough. The shaft bearings were also replaced in mid-March. After the motor repairs, the late March and April data do not show the large variations in the shutter drift. The first problem, the stability of the local power grid, was also less significant during the late March and April data periods. In future experiments, the problem with the power variations can be eliminated by using a crystal controlled power regulator for the shutter motor.

The drift of the shutter position was corrected and we have reasonable confidence in the final results. The procedure included a careful examination of the white light shutter functions that were obtained. The conclusion of that study was that the geometrical model for the shutter function provides a reasonable fit to the data obtained. Figure 5 shows that the slot opening crosses the field of view of the primary mirror image. A small variation due to the secondary mirror obscuration is apparent in the shape of the shutter function. Figure 12 shows the geometrical function compared to the data from the white light calibration curve of 3 March 1986. The extreme steepness of the shutter opening curve, shown in Figure 11, leads to a very large sensitivity of the low altitude data to errors in the timing of the shutter opening of even a small fraction of the 2 msec channel width. Thus in the "EDIT" program used to prepare the data for analysis, the ratio between the data channel at 16 km and that at 45 km provides a sensitive measure of any shift in the shutter opening position. The ratio of the count rate at 16 km to that at 45 km measured for each of the data runs on 14 February 1986 is shown in Figure 13. From this ratio, the magnitude of the shutter drift can be accurately determined. In Figure 13, a large shift can be seen at run 47. The effect of the drift of the shutter wheel from +2 channels to -1 channel is demonstrated in Figure 14. As expected, the major change is observed at the lower altitudes. The magnitude of the shift determined from the signal ratio at 16 and 45 km is recorded and incorporated into the "RUN" file used by the final data
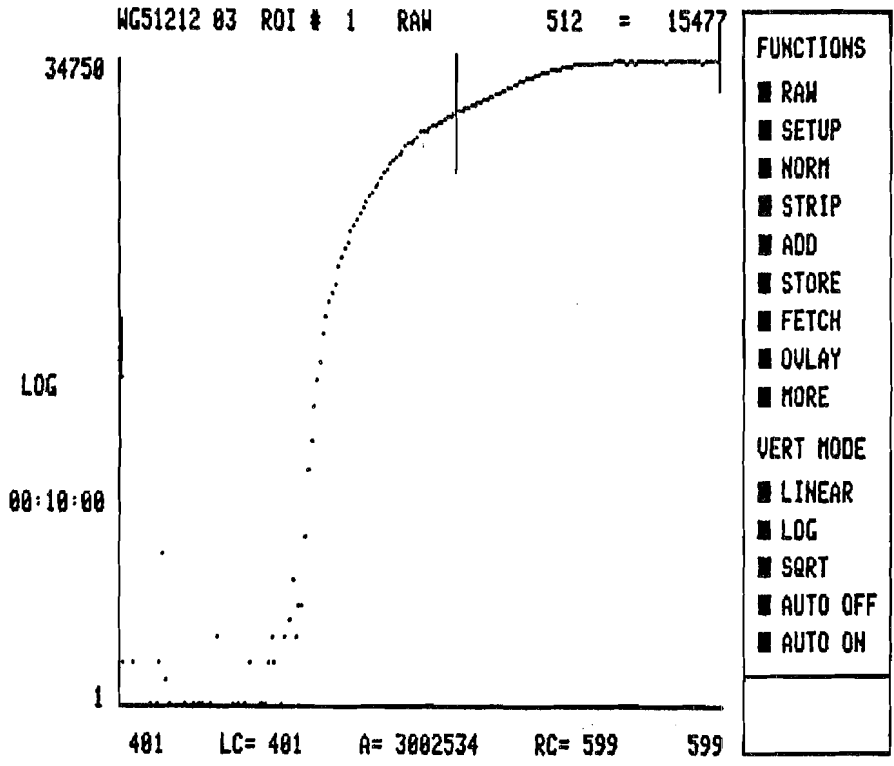
Figure 11. Plot of the Data Obtained During a White Light Calibration of the Shutter. The opening begins near 12 km (channel #455) and is fully open by 45 km (channel #565).
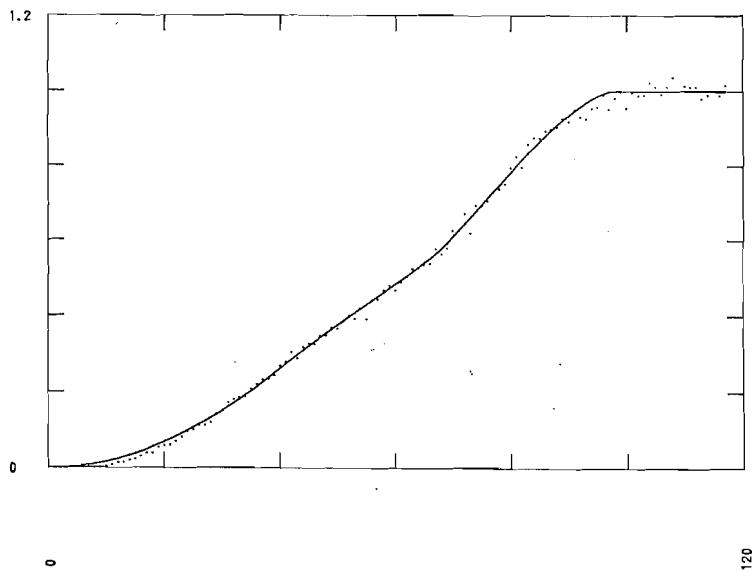
Figure 12. Comparison of the Smooth Model Calculation, Based on the Geometrical Shape, and the Data Measured During White Light Calibration on 3 March 1986. Here the vertical scale is linear as opposed to the log scale of Figure 11. The slope change near midway in the curve is caused by the secondary mirror obscuration.
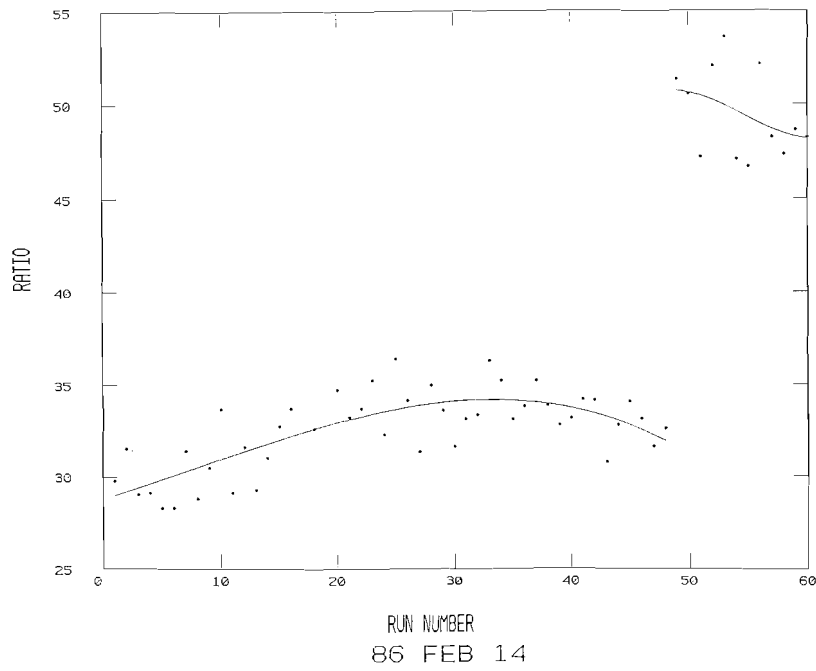
Figure 13. Ratio of the Count Rate at 16 к л to That at 46 km During the Night of 14 February 1986.
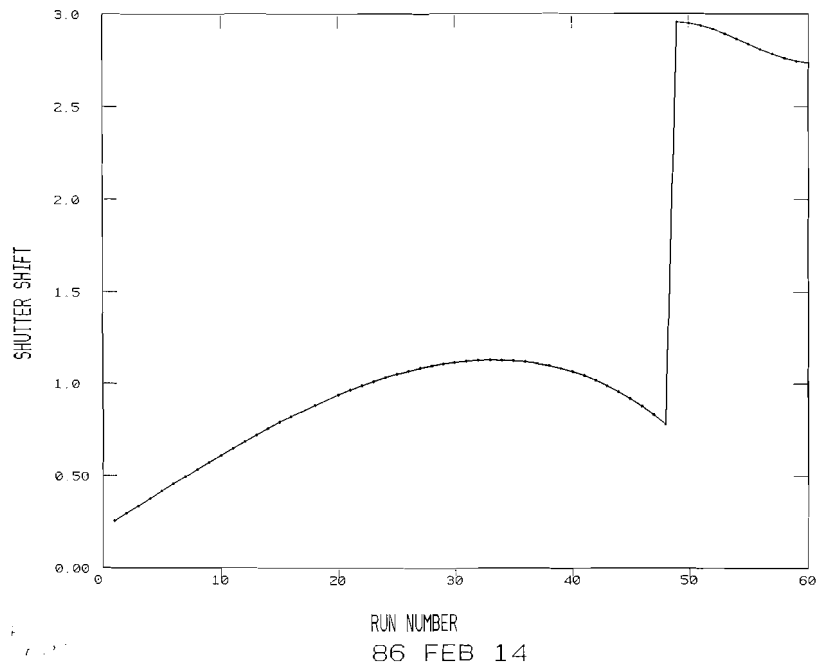
Figure 14. Change in the Density Profile as a Function of Offset of +2 to -1 Channel Widths.

49

processing program. In this way the shutter corrections due to changes in the timing position have been automatically corrected in the analysis program.

Figure 12 shows a comparison of the geometrical shutter calibration curve compared to the data from the white-light calibration for a typical measurement. The shutter begins to open at an altitude corresponding to about 12-13 km and is fully open by 45 km. By removing a significant portion of the low altitude signal, the shutter prevents the photomultiplier tubes from being overloaded by the high count rates. The altitude profile is fully reconverted by dividing the measured count rate by the normalized shutter function. A small hole in the shutter wheel that acts as an initial timing pulse is sensed by a LED detector. The laser Pockels cell switch is fired 316 channels after the LED trigger is detected. The timing is set up to have the laser flash lamps fire a sufficient time before the Q-switch (Pockels cell) pulse. All of the critical timing is referenced to the time when the LED trigger is initiated by the shutter wheel. The time period between the 16 km altitude shutter opening point and the trigger pulse is approximately 766 μsec (316 + 67 channels of 2 μsec each). Since the rate of change of the signal allowed by the shutter wheel is extremely high at the beginning of the shutter wheel opening, it is possible to make a very sensitive measurement of any drift in the relative position of the shutter opening relative to the laser firing. To develop a correction for the variation in the shutter opening time, the ratio of the signal in the data channel near 16 km was compared to the signal in data channels between 43 and 55 km. The test can show variations in the shutter opening drift to the level of 0.1 msec. Since we are only applying the correction and using results for altitudes above about 20 km, the correction procedure appears to be quite sufficient.

6.2.2 SHUTTER DRIFT ON THE 62 cm TELESCOPE

An additional problem was found in the high altitude shutter function. Because the high altitude shutter is phase locked to the low altitude shutter, a loss of sync between the motors caused by noise or a voltage transient can require several tens of seconds to fully dampen and lock the signals. The circuit that was being used during the February and March windows to provide the sync lock of the shutter on the 62 cm telescope detector was not satisfactorily responsive. The circuit was changed and improved in April to maintain better sync. Also, the line noise and transient problems that caused sync loss were much less prevalent during April. Even though large effects are observed during the seeking phase of a large wander in the high altitude shutter position, it appears that reasonable corrections can be made to the results. The high altitude shutter was intended to cut off the high intensity of the low altitude laser pulse so that measurements above 45 km would not suffer from overload and saturation effects on the photomultiplier tube. The effect of the sync lock loss was found to cause significant corrections extending as much as ±150 μsec (±45 km) or essentially encompassing the full measurement range. Figure 15(a) shows a representation of the high altitude

shutter curve for normal operation and examples of the family of curves that can occur when synchronization is lost. Figure 15(b) demonstrates an explanation of the shutter drift. In curve (1), the rate of change in the transmission is represented by the change in area as the shutter moves past the image of the primary. The slope change, which is most pronounced just before the midway open position (a), is due to the obscuration of the secondary mirror. The transmission as a function of time is shown in curve (2), which is just the integral effect of curve (1). Curve (3) indicates the signal variation that results from the transmission curve combined with the exponential decrease of the atmosphere. Curve (4) represents the normal distribution of the drift of the sync position as the drive circuit seeks to relock the system. Curve (5) shows the expected signal as the sync drift affects the measurement (see Figure 15(a)). It appears that a correction algorithm can be applied to most of the affected data to account for this problem. This algorithm is presently being developed. Some of the profiles will probably not be usable when the sync drifts beyond some limit. The reason is that when the drift is sufficient to open the shutter at very low altitude, say below 10 km, the intense signal will produce a nonlinear effect in the photomultiplier, poor background recovery and after-pulsing in the signal. These cases will probably need to be discounted.

Analysis of the results shows that variation of the shutter opening position of more than ±100 μsec occurred several times during the February and March windows. In the future, a crystal-controlled frequency and voltage generator will be used to power the shutter motor and thus eliminate the time drift errors encountered in this data set. The April data, during a relatively warm period when power line variations were minimal, did not show any significant shutter position drift.

6.2.3 DESCRIPTION OF THE DATA EDIT AND SMOOTHING APPROACH

The data consist of accumulated photon counts. Usually, in such a system there are atmospheric regions that produce such a weak return that smoothing is required to reduce statistical fluctuations in the data. Several different smoothing procedures were investigated to determine the best procedure to be used for the data reduction program. Some set of criteria is needed to compare the different procedures with each other and on an absolute basis. The procedure used for this analysis must be simple, accurate, and well defined. In Appendix A, the various approaches are described.
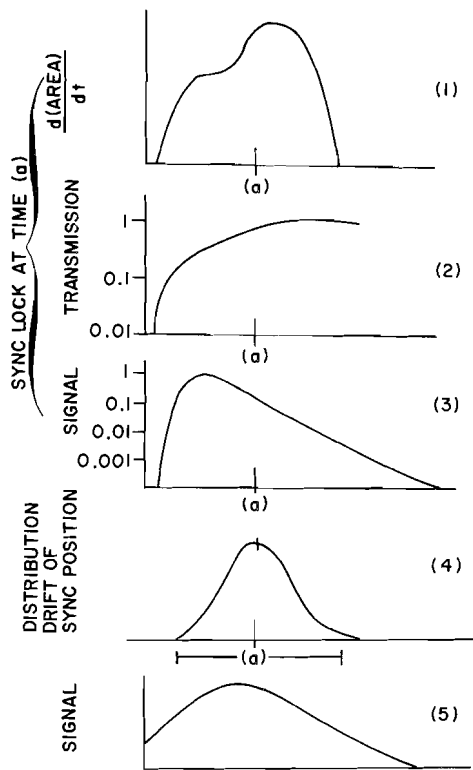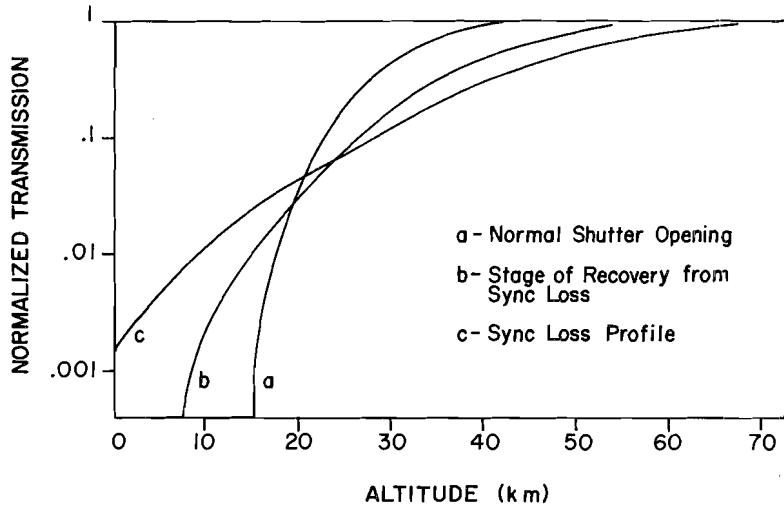
Figure 15. Transmission Changes in the H Detector When the Shutter Loses Sync.

The first try at a smoothing procedure was a simple sliding average. This procedure was considered marginally acceptable, as it met the above criteria in a general way. However, the smoothed data were still fairly noisy. The noise was mostly high frequency noise generated at the edges of the rectangular smoothing window.

The next procedure used was also a sliding average except that a Hanning window was used for smoothing instead of the rectangular window. This smoothing procedure has a good high frequency cutoff and does not add any ringing to the data. While investigating this procedure through literature searches, a similar filter using the Blackman window was found. This filter is basically an extension of the Hanning filter extended to higher frequencies and results in a stronger attenuation of the high frequency components of the data. A study of the filters usually applied to various data sets was made (see Appendix A).

From the study in Appendix A, the Hanning filter (commonly referred to as the raised cosine filter) was chosen as the best filter for the analysis of the lidar data. The sliding average filter was rejected on the basis of insufficient high frequency rejection. The Blackman filter performed well, but not really noticeably better than the Hanning filter. The added terms in the window definition make the increase in complexity not worth the effort. The FFT-based filters all have some disadvantage such as ringing or complexity of application. The exponential cutoff FFT filter could be made not to ring but the filter was more complex and more difficult to apply.

The results were obtained using 2 μsec range bins, which correspond to 300 meter altitude steps in the data. The smoothing interval of the filter must be changed as a function of altitude. The magnitude of the counts in the range bin was selected as the criteria for changing the smoothing interval. The selection of the thresholds for making the changes was somewhat subjective. The length of the smoothing interval and the threshold have been considered together to allow a reasonable tradeoff between the statistical accuracy of the data and the altitude resolution. The criteria for the altitude resolution was based on the recognition that the minimum vertical wavelength for a propagating wave is about 1 km near 60 km and about 3 km near 90 km. However, this data set has shown that the larger contributions to the structure variations are not due to the propagating waves (in summer, the monochromatic propagating waves may be the most important factor). The information in Table 11 states the thresholds used in the data analysis.

Table 11. Threshold counts for changing the smoothing interval used in the Hanning filter. The effective filter length is given.

# counts	smooth index n	actual # channels 2n + 1	effective # channels n + 1	filter length (km)
> 10000	0	1	1	1.3
3000-10000	1	3	2	1.6
1000-3000	2	5	3	1.9
500-1000	3	7	4	1.2
200-500	5	11	6	1.8
100-200	7	15	8	2.4
< 100	9	19	10	3.0

The large transients in power and the static electricity in the cold dry environment led to rather large, but infrequent, noise spikes in the data. These have been examined in a few cases to develop a routine method of processing the results. At times the magnitude of the transient was large and the recovery time was long, many consecutive range bins. In other cases, only a single range bin was affected. When the transient involved only a single range bin, the data in that bin were modified to a mean value of the data in the adjacent bins, with the criteria that the single bin had exceeded the running mean by more than 4σ. Few points were changed by this procedure and when it was applied, the bin exceeded the 4σ criteria by a large factor.

The value of the sky background, from the 10 shutter files of sky background between each laser firing, and the mean values of the channels between the altitudes 90-100 and 100-110 km were plotted for each run during each night. By examining these plots it is possible to identify most of the files of concern for the large noise transients. Figures 16 and 17 show an example of the change in the sky background that resulted from a noise transient. The background was measured ten times for each laser firing on the G files and five times for the H files to provide an accurate measure of the sky background. The other measurements between 90-100 km and 100-110 km are used to test whether the data was likely to have been affected by a noise pulse. The results shown in Figures 16 and 17 were obtained on 27 April. The short night conditions are obvious as the sky background signal decreases at sunset and begins to increase again 3 hours later. A running mean curve is shown through the data points and an upper curve shows the relative value of the $+4\sigma$ statistical uncertainty. The data files which exceed this + 4s value have been rejected from routine data processing.

The errors which result from the statistical uncertainty in the signal counts for example profiles on 14 February 1986 are shown in Figure 18. This is typical of the data on which the errors described in Table 12 are based. The jagged steps in the error plots are due to the discrete steps in the changes of filter interval along the profile (Table 11 describes the thresholds for the changes in smoothing interval).
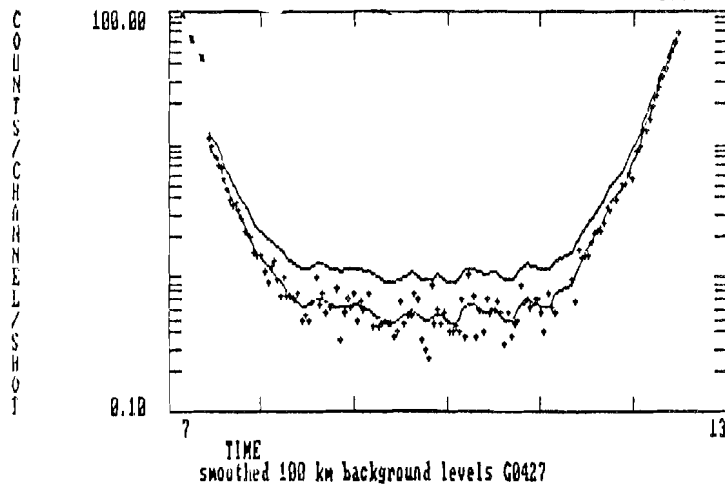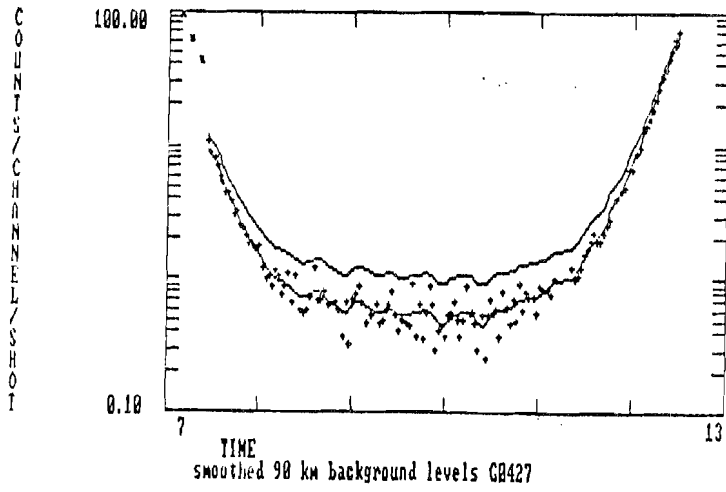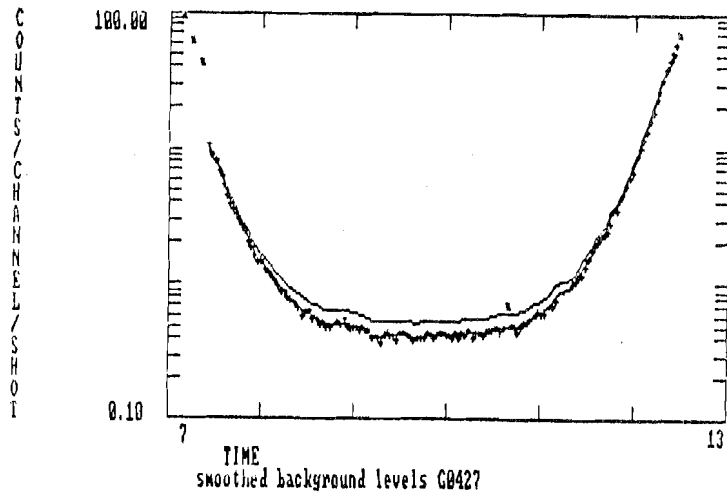
Figure 16. Example of the Background Curves for G Files from Night of 27 April 1986.

56
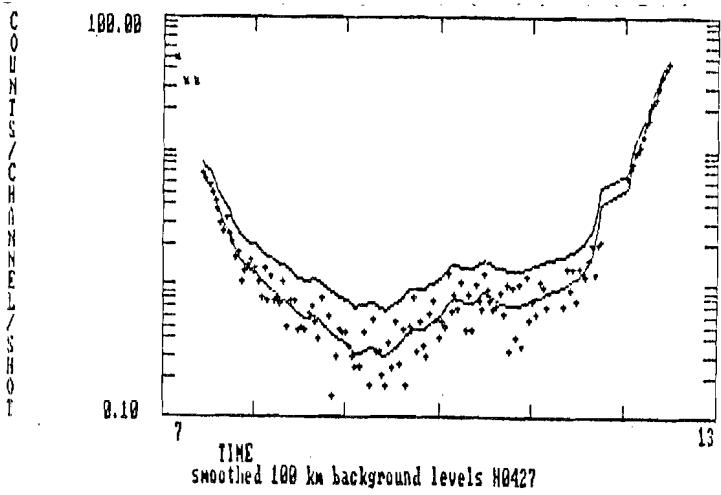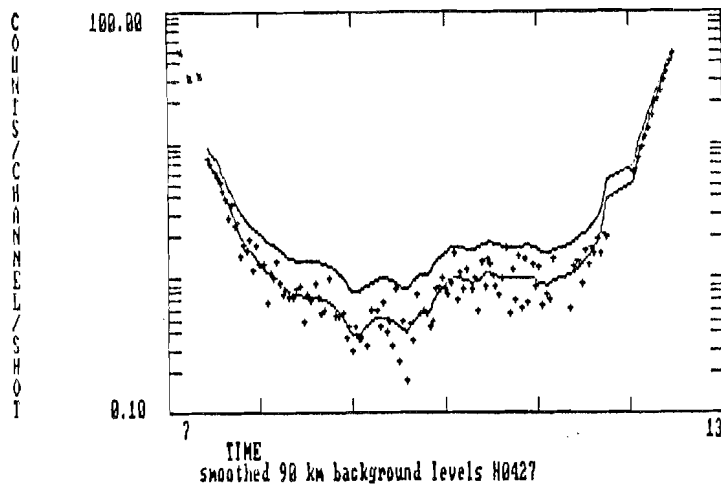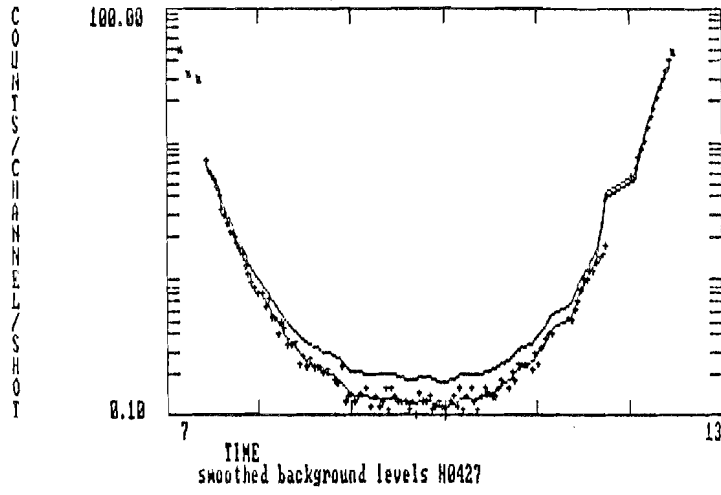
Figure 17. Example of the Background Curves for H Files from Night of 27 April 1986.

57
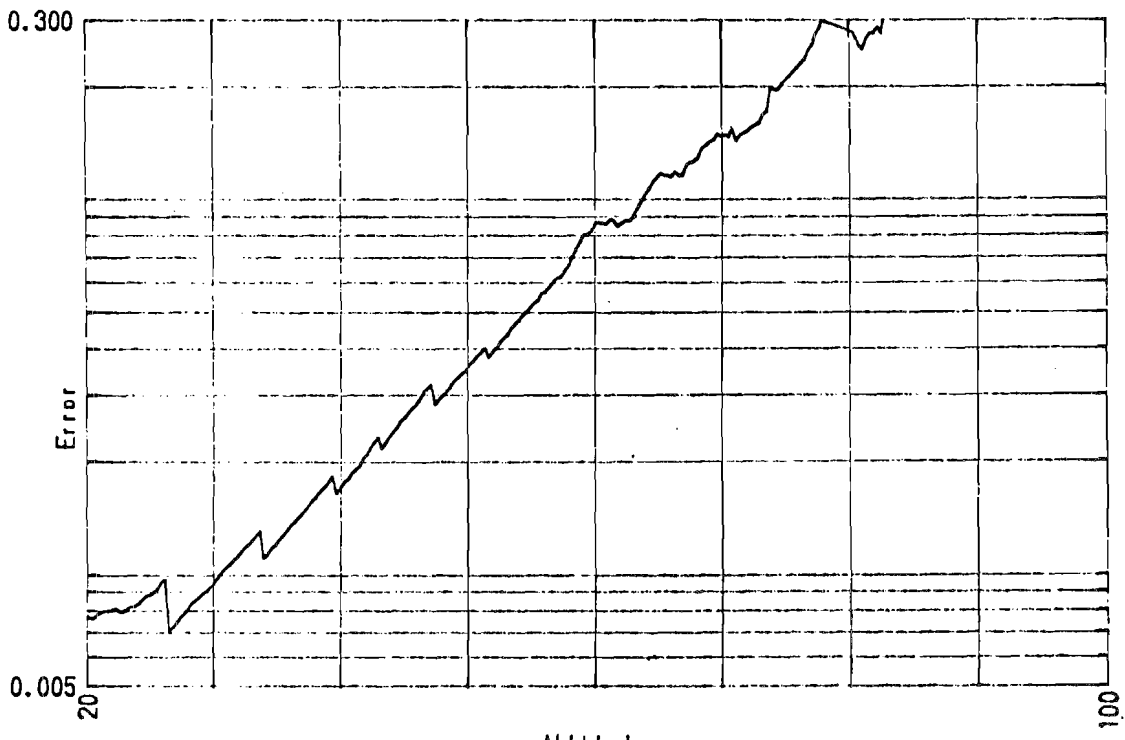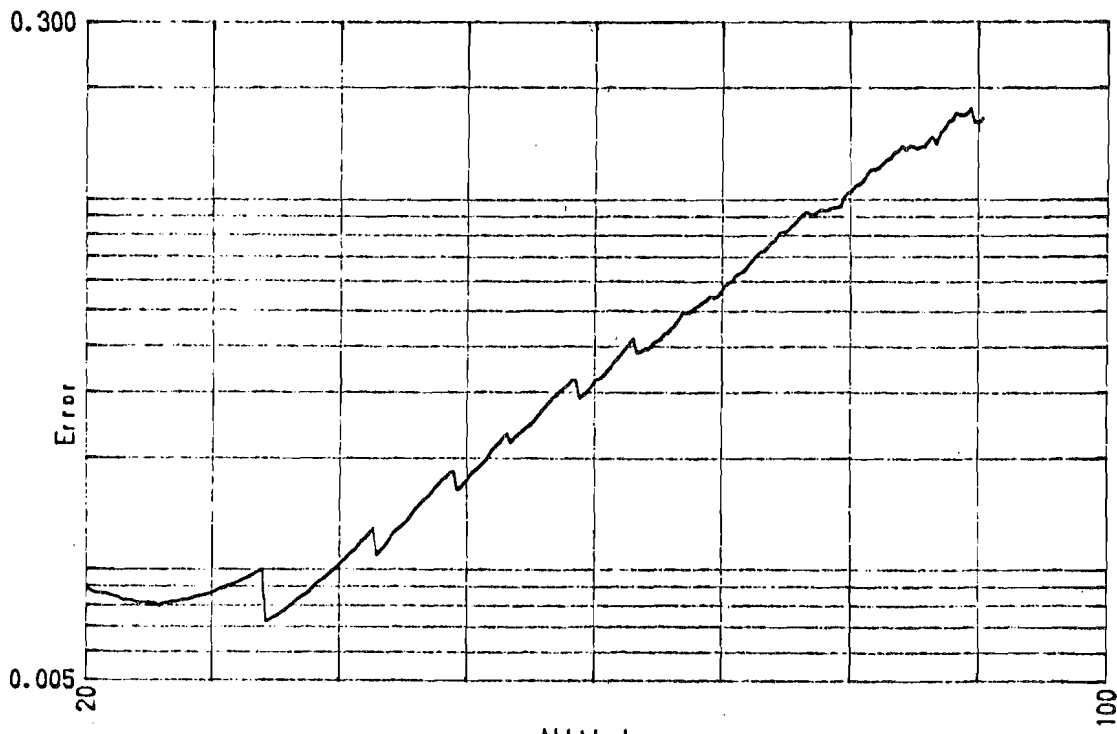
Figure 18. Examples of the Error Curves for Typical Runs of the G and H Files from Data of 14 February 1986.

7. SUMMARY OF RESULTS

The data obtained during operating periods during February and March 1986 consisted of a sequence of 3,000 shot (5 min) data runs. The 5 min data periods were chosen to be short relative to the minimum expected period of propagated waves, that is the resonance period of about 7 to 10 min. Because of the results of quick look analysis of the February and March results, the data period for accumulation was reduced to 1,000 shots, or 100 sec, for the April measurements. It is possible to co-add the data runs over longer periods to improve the signal to noise. The short data runs are not useful for altitudes above 60 km because of the low statistical accuracy. The short runs do, however, show the importance of interpretation of the background irregularities of the atmosphere. The granularity in the density structure, amounting to a few percent with scale sizes of a few kilometers, contribute to the shorter period variations observed in the data. The lidar path is a thin pencil probe through which the irregularity of the background neutral atmosphere moves in the horizontal wind field.

7.1 Ultraviolet Measurement Results

On each evening that lidar data was obtained, a series of 3-5 profiles were obtained using the ultraviolet wave length at 355 nm. The ultraviolet signal to noise is significantly poorer than the signal for the green wave length. We suspect that one of the optical coatings in the transmit or receive section of the lidar is not reflecting or transmitting the expected fraction of the ultraviolet light. Because of the poor signal to noise ratio, and the fact that only two measurements can be made simultaneously with the data system, the ultraviolet return is not routinely monitored.

Figure 19 shows the profiles measured by the green and ultraviolet detectors on the 32 cm telescope during periods of simultaneous operation. Figure 20 shows the smoothed ratio of the green (G) to the ultraviolet (U) profiles of the cases corresponding to those in Figure 19. The important point to note is that for altitudes above 30 km the profiles are in complete agreement (until the noise contributions of the UV profile becomes significant near 60 km). At altitudes below 30 km, the signal from the green detector is significantly higher than that for the ultraviolet detector. The ultraviolet detector is relatively more sensitive to the molecular scattering and relatively less sensitive to the particulate scattering. This is due to the molecular scattering cross section which has a very steep dependence on wave length, $1/\lambda^4$.

Figure 20 shows the ratio of the G to the U signal as a function of altitude. The large increase in relative signal in the green detector at the lower altitudes is due to the scattering by volcanic dust in the altitude region between 15 and 25 km. An examination of the data will show a significant variability from day to day, and even during a night, in the intensity of the signal from the layers. During the time period of these tests in Alaska, the St. Augustine volcano off the coast of Alaska erupted several times and ejected dust into layers observed most prominently between 19 and 22 km.

By use of the two colors, green and ultraviolet, it is possible to resolve the question of what altitude regimes can be properly analyzed as regions of pure Rayleigh scatter from which density and temperature can be directly determined. The signal from the ultraviolet detector was not sufficient to resolve the question of the Mie scattering in the 75-80 km altitude region in the April results. In a subsequent test, the ultraviolet signal could be integrated for a sufficiently long period to resolve this question.

7.2. Examples of the Results

As examples of the lidar data obtained during the campaign in Alaska, the results in Figure 21 show the extremes of the profiles measured. The profile from February represents the winter case of mesospheric densities as low as half of the mean values represented by the USSA76. By April, the density is approaching the summer case of densities 50 percent greater than the mean. Note that the region between 18 and 25 km exhibits intense changing layers. This signal is due to the aerosols and volcanic dust scattering the laser beam. The scattering cross section for dust is larger than molecular scattering. Significant changes in the character of this region could easily be correlated to the volcanic activity during the period.

Figure 22 shows examples of profiles measured in on 4 March 1986 and on 14 February 1986. The profiles are density ratio to the USSA76 model. The size of the $\pm 1\sigma$ error bar is shown on the data with a spacing that indicates the length of the smoothing interval. The 4 March case exhibits rather strong wave activity, which was observed frequently in March. The February data includes profiles of both the G and high altitude (H) detectors. The H profile shutter opening is supposed to be complete by 45 km and the two profiles should overlap from that point. The shutter sync loss reduces the signal at lower altitudes and some signal is lost, particularly near 40 to 50 km. In Figure 22(b), the H signal appears to be reduced by about 3 percent near 45 km and the difference decreases with height. If the H signal were 3 percent higher at 45 km, 2 percent higher at 50 km, and decreased to no bias near 65 km, then the results of the two example profiles would overlap very well. Section 6.2 discusses the shutter drift errors.

These examples show the large change that occurs in the high latitude density due to seasonal effects, that is, dynamical processes and radiation balance. The typical mid-winter values of density in the mesopause are about half of the equinox values (which are near the mean model) and the summer values are 40 percent greater than the equinox values. One of the striking effects in the data is the large scattering layer that has developed during the time that measurements have been made here. The examples show the strong effects of the volcanic dust at altitudes between 15 and 25 km.

7.3. Lidar Performance Compared to Expected Results

Comparison of the calculations of Table 1 with the results of Table 12 shows that the overall performance and accuracy of the lidar was approximately as expected. The decrease in the sensitivity of the 62 cm detector between February and April is due to a decrease in the collected counts. The change in sensitivity is due to a change in the alignment of the 62 cm telescope axis which caused the effective collecting area of the telescope to be reduced significantly. The ratio of the signal in the H files to the corresponding G files should be approximately the factor of five which was observed in February. The errors associated with the G and H files for a data run are shown in Figure 18. The small jumps which occur in the graphs are the result of the discrete changes in the smoothing interval.

One other factor caused a reduction in the sensitivity of the H detector during several periods. The transmission of signal photons through the detector was reduced by a deposit from the outgassing of the material used to thermally insulate the housing of the thermally stabilized narrow band pass filter. The top window to the thermoelectrically cooled photomultiplier housing was coated by the deposit on several occasions. Cleaning of this element became a routine part of the operating procedure. A material with lower outgassing properties will be substituted in the detector for future measurements. The major effects from the outgassing were found to occur during the initial warm-up of the filter housing (temperature cycle overshoot) and the problems were greatly reduced by leaving the temperature stabilizing circuit powered.

During the test period in Alaska, the performance of the instrument was carefully monitored during the data runs. Several parameters were continuously observed and recorded to evaluate the performance, as carefully as possible, during real time operations. Numerous factors were found to affect the performance of the equipment during the program. Some of those factors included:

(1) Power line transients and variations in the voltage and frequency of the power affected the performance of the system. This problem influenced the detector shutters as described in Section 4.2.
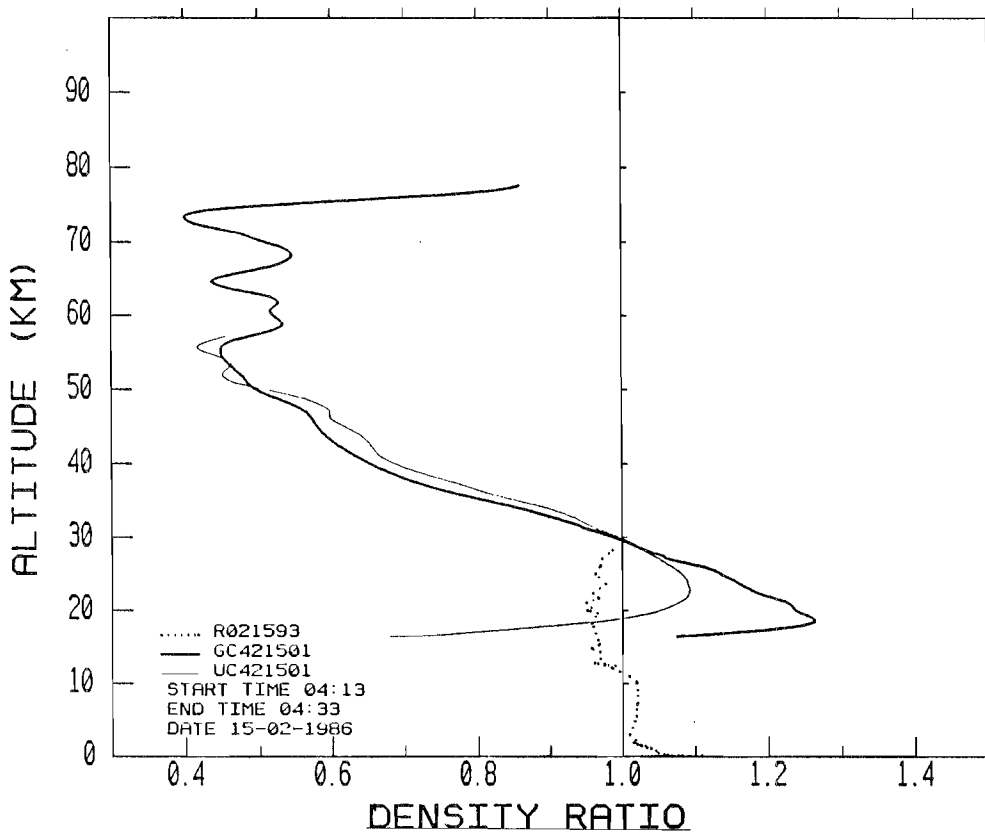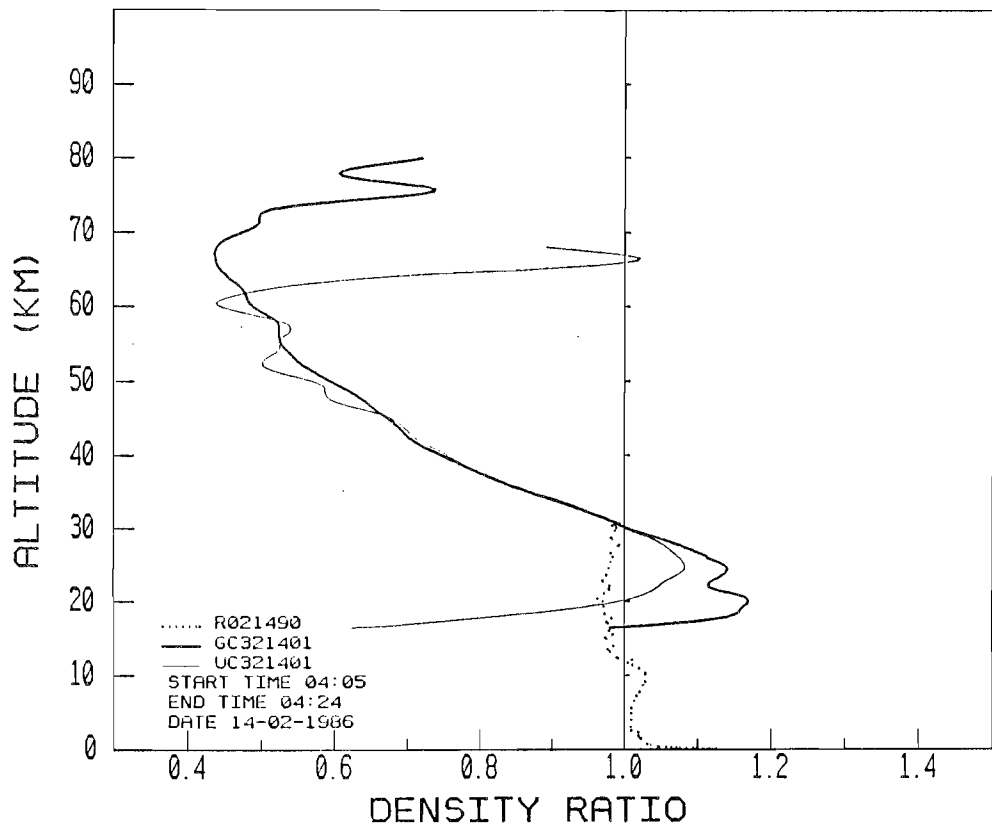
Figure 19. Comparison of the Visible and Ultraviolet Lidar Profiles (a) 14 February 1986 (b) 15 February 1986.
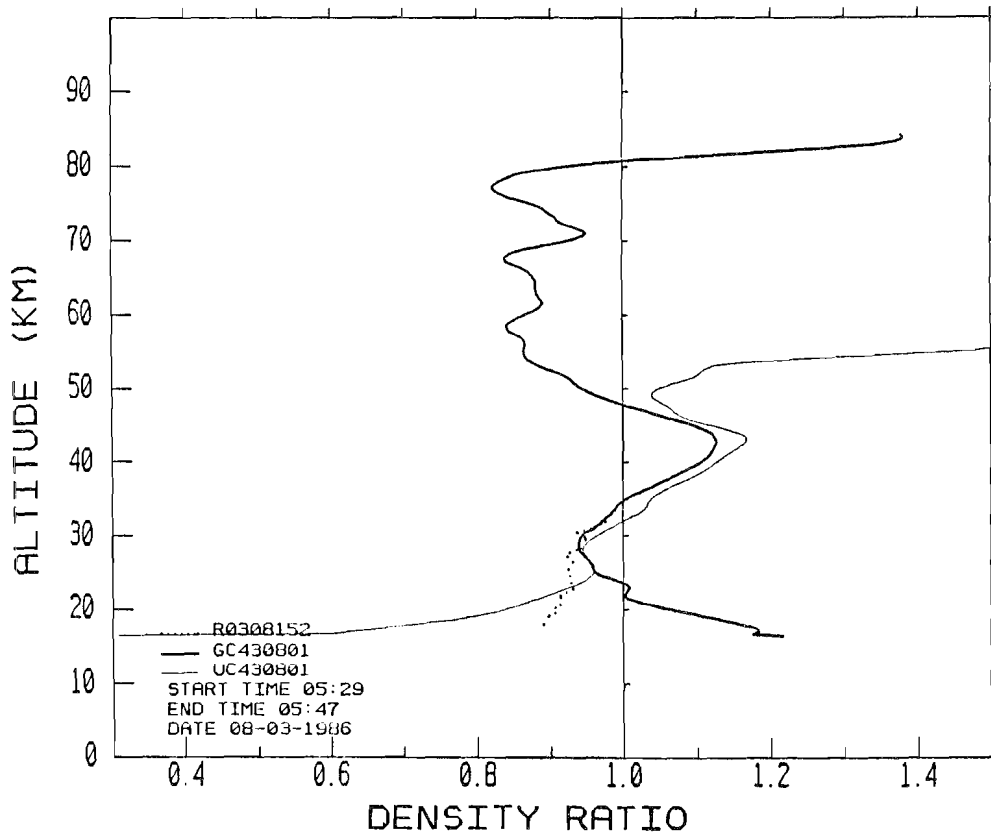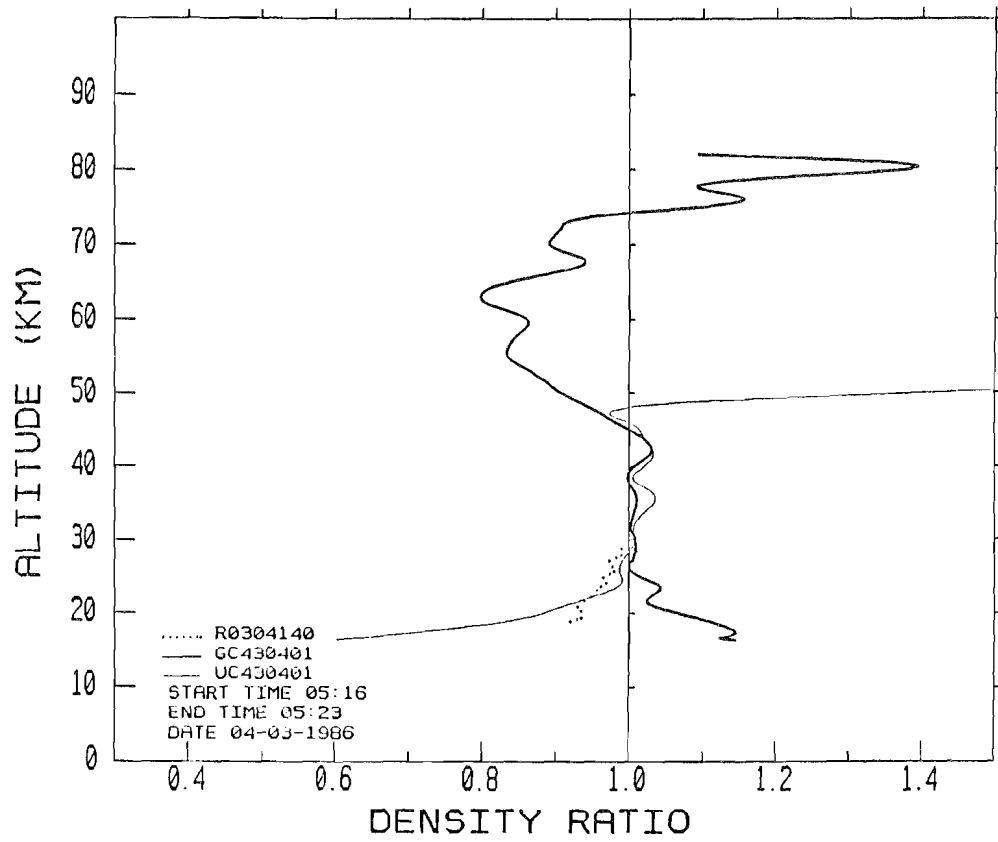
Figure 19. Comparison of Visible and Ultraviolet Lidar Profiles. (c) 4 March 1986 (d) 8 March 1986.
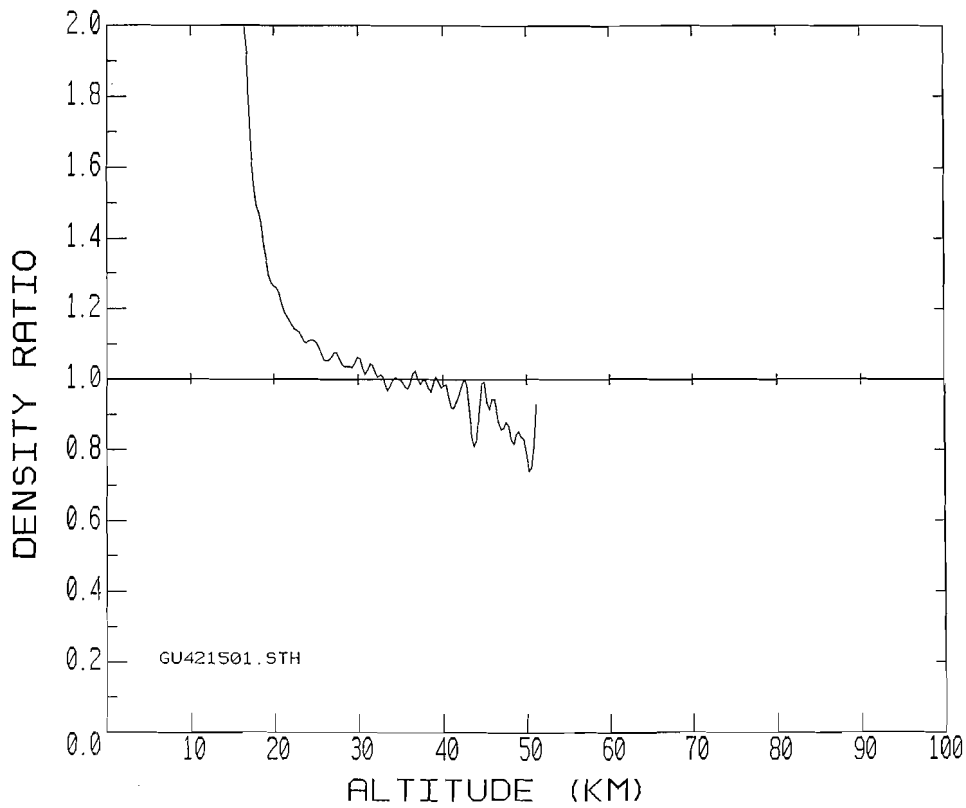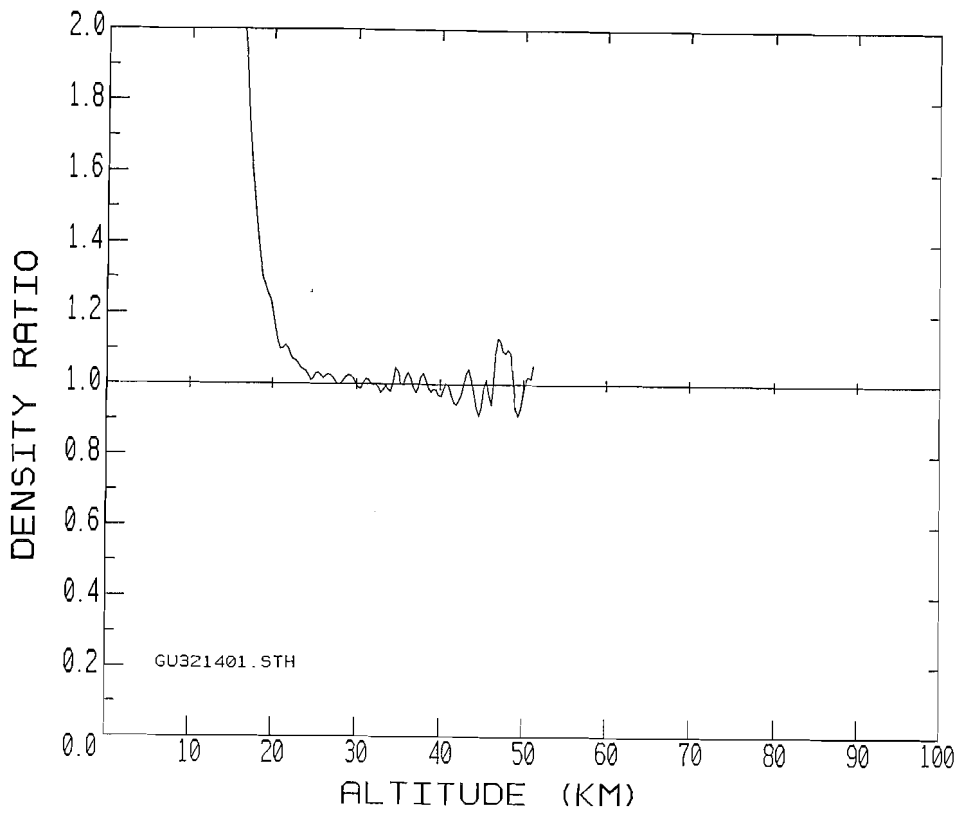
Figure 20. Ratio of the Visible to Ultraviolet Profiles (a) 14 February 1986 (b) 15 February 1986.
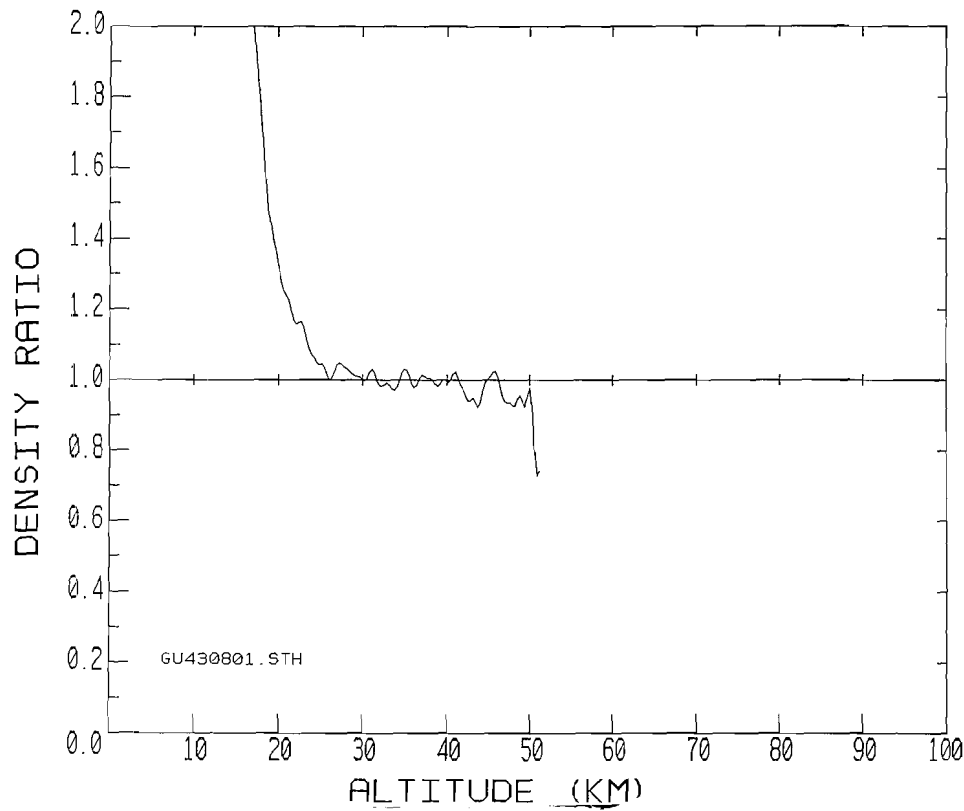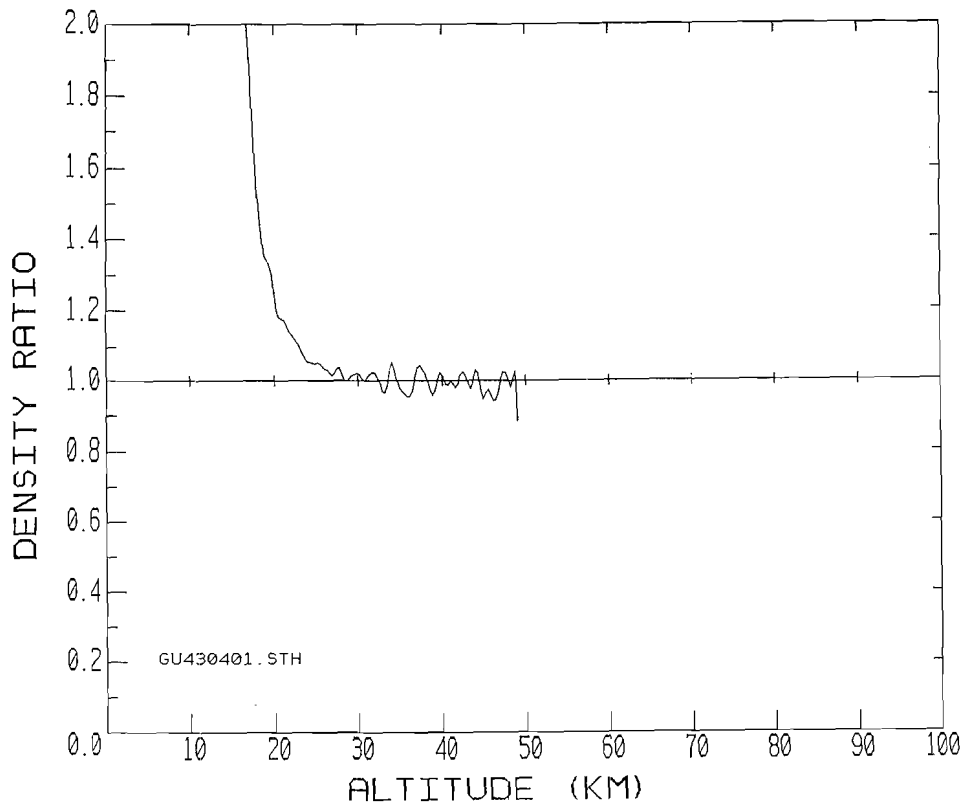
Figure 20. Ratio of the Visible to Ultraviolet Profiles (c) 4 March 1986 (d) 8 March 1986.
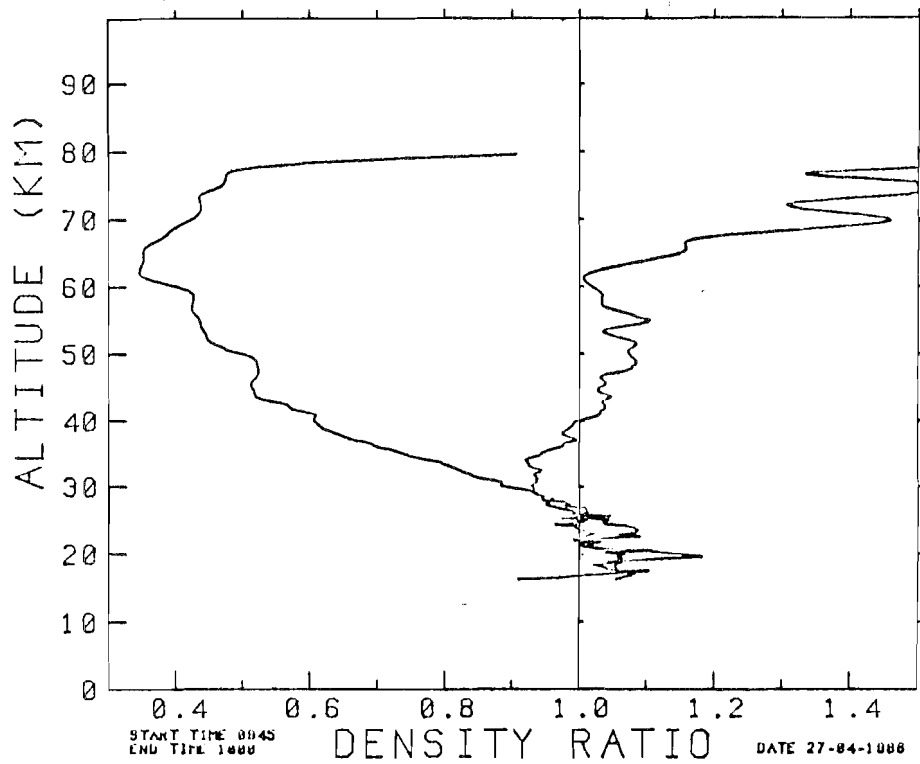
Figure 21. Comparison of the Extremes of the Density Profiles Measured, Winter Conditions on 14 February (Run 31) and Summer-like Conditions on 27 April 1986 (Run 43).

66
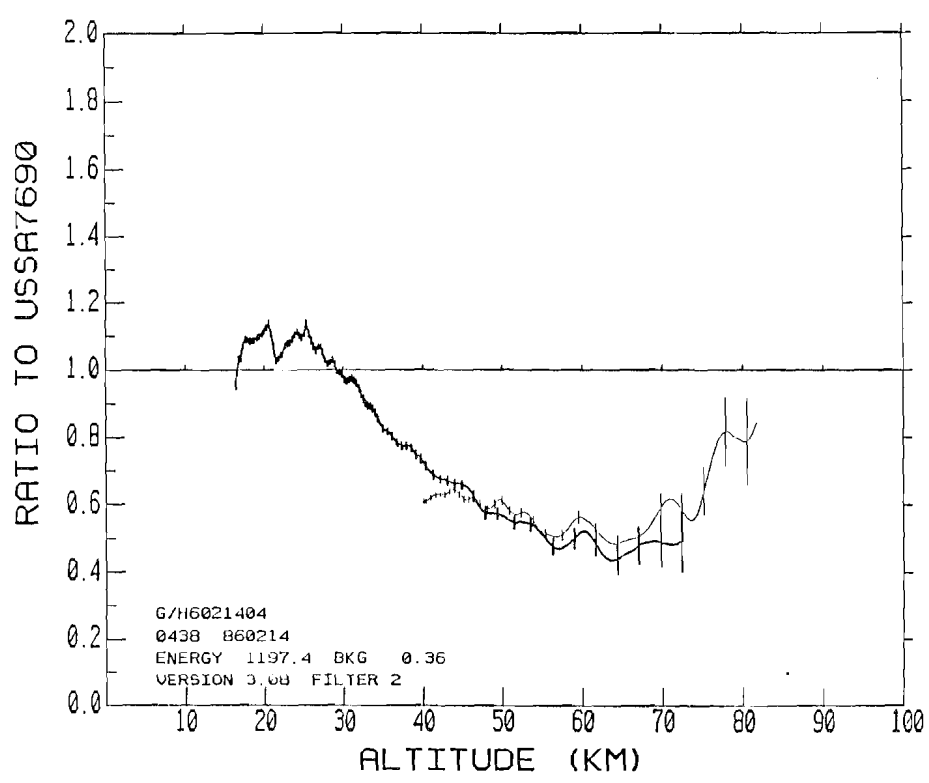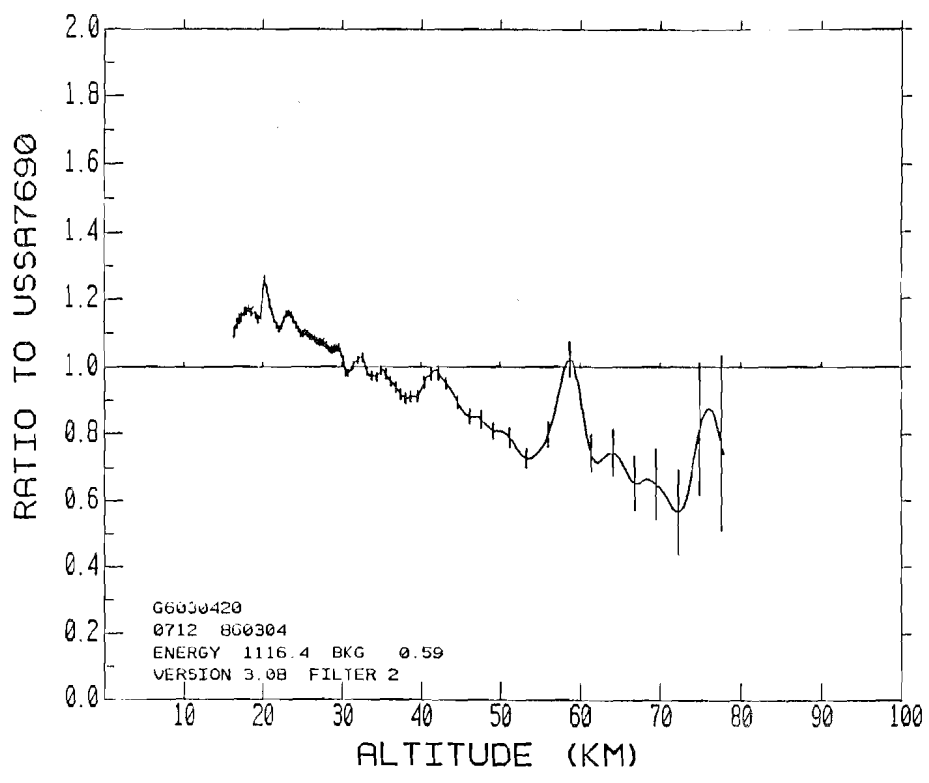
Figure 22. Examples of Density Profiles Measured by the Lidar on 4 March and 14 February 1986.

Table 12. The Accuracy of the Lidar Based Upon Actual Performance (Count Rate of Typical Data Runs). These numbers represent only the statistical error; the tie-on error for the rawinsonde of 2 to 3 percent must also be included. These values are based on the actual results and thus include the time for data transfer and storage, which make the errors larger than they would be if data was actually accumulated for a 1-hr period.

February Data — 32 cm Telescope

Altitude (km)	1000 (km)	1000 %	3000 (km)	3000 %	9000 (km)	9000 %	hour (km)	hour %
20	0.3	1.2	0.3	0.8	0.3	0.5	0.3	0.3
30	0.9	1.8	0.6	0.9	0.3	0.9	0.3	0.6
40	1.5	2.4	1.2	1.6	1.2	1.0	0.6	1.0
50	2.7	4.5	2.4	3.0	1.8	2.5	1.2	1.9
60	3.0	10.3	3.0	7.3	2.4	4.4	2.4	3.4
70	-	-	3.0	14.6	3.0	8.9	3.0	6.3
80	-	-	-	-	-	-	3.0	19.5

February Data — 62 cm Telescope

Altitude (km)	1000 (km)	1000 %	3000 (km)	3000 %	9000 (km)	9000 %	hour (km)	hour %
40	1.2	1.4	0.6	1.1	0.6	0.9	0.6	0.8
50	1.8	2.0	1.2	1.7	1.2	1.5	0.9	1.4
60	2.4	4.0	2.4	2.8	2.4	2.5	1.8	2.4
70	-	-	3.0	5.1	3.0	4.5	3.0	4.0
80	-	-	3.0	9.6	3.0	8.7	3.0	8.3

April Data — 32 cm Telescope

Altitude (km)	1000 (km)	1000 %	3000 (km)	3000 %	9000 (km)	9000 %	hour (km)	hour %
20	0.6	1.5	0.3	1.0	0.3	0.6	0.3	0.4
30	0.9	1.8	0.6	1.2	0.3	1.0	0.3	0.7
40	1.8	2.4	1.2	1.8	0.6	1.5	0.6	1.0
50	3.0	4.5	1.8	2.9	1.2	2.3	0.6	1.9
60	3.0	10.4	3.0	7.5	2.4	4.8	1.8	3.7
70	-	-	3.0	15	3.0	9.7	2.4	8.1
80	-	-	-	-	-	-	2.4	20.1

April Data — 62 cm Telescope

Altitude (km)	1000 (km)	1000 %	3000 (km)	3000 %	9000 (km)	9000 %	hour (km)	hour %
40	1.2	1.9	0.9	1.4	0.6	1.2	0.6	0.8
50	2.4	3.1	1.8	2.5	1.8	2.0	0.9	1.7
60	3.0	6.0	2.4	3.8	1.8	3.1	0.9	2.4
70	3.0	13	3.0	7	3.0	5.7	2.4	4.0
80	-	-	-	-	3.0	14	3.0	9.4

On a few occasions this equipment was turned off as the voltage on the 110 volt line dropped as low as 85 volts.

(2) Static discharge caused the computer system to be reset. On numerous occasions, the reset caused by static discharge from operating personnel caused the computer to be reset, so that it was necessary to re-boot and re-initialize the data taking system.

(3) Large temperature gradients through the laser beam porthole in the optical table caused a shimmering or dancing of the beam when outside temperatures were in the range below -30°. The shimmering of the beam was only a problem on a few of the evenings and a solution was found in inserting a cardboard tube extension into the optical bench porthole, which seemed to provide a laminar flow condition that stabilized the beam direction in the region of strong thermal convection between the inside room temperature and the outside ambient temperature.

(4) Blowing snow on the ridge of the mountain caused snow storms in the lower hundred feet of the atmosphere at times. It was found that a large fan blowing across the beam steering mirror could keep the snow from coating the surface, thereby, degrading the performance of the instrument significantly. The overall transmission of the atmosphere was not reduced significantly by the light blowing snow.

(5) The signal collected by the lidar was at times degraded by the alignment of the laser beam to a region near the center of the field of view of the receiving telescope. The field of view of the receiving telescope is described later in this section. Since the primary detector system is essentially monostatically aligned (laser beam leaves from a point on the optical axis of the telescope) between the laser beam and the telescope axis, any change in sensitivity resulting from a non-centered laser beam should only result in reduced sensitivity for the profile and not result in height dependent effects until the sensitivity is significantly degraded. Concern for this problem prompted many careful realignments of the beam, as many as two or three times during a night when any sensitivity change was noticed. During the later data periods in March and April, the sensitivity drifts were not apparent. This factor leads to a conclusion that at least part of the problems observed during February and early March were due to mechanical changes caused by thermal contraction during the periods of extreme temperatures (the alignment between the laser axis, the laser being at room temperature, and the telescope optical axis, the telescope and beam steering optics being at ambient temperature, is sensitive to changes in the 100 μrad range).

(6)   Overall equipment performance was considered to be good or excellent considering the intensity of the use of the equipment during the period. The major problem encountered was the failure of the laser power supply which resulted from a defect in a high current/high voltage connector which gradually deteriorated until its failure destroyed numerous components in the laser power system. One section of the power system was returned to the manufacturer for repair and the other damaged components were repaired in the field by the operating personnel. Two failures were noted in the safety radar during operation. One resulted in replacement of tubes in this older tube-type radar system. The second resulted in replacement of a large capacitor in the 400 Hz power system which provides the operating power for the radar. Other minor failures of equipment included a noisy pulse-height amplifier in the detector system, a ±15 volt power supply, and several component replacements.

The alignment of the laser beam with the optical axis of the telescope is critical for operation of the lidar. It is important to have a small field of view for the telescope to minimize the amount of background starlight, which would limit the overall sensitivity. Based upon our laboratory experience and review of information on beam wander, we choose to make the telescope field of view about 5 times the size expected for the laser beam divergence. The beam divergence of the laser with the beam expander has been found to be in good agreement with the design goal. The beam expander was tested using a 2 mile horizontal path at the NASA Wallops Island Center in December 1985. The overall beam divergence was found to be in the range 0.13 to 0.16 mrad. The telescope field of view can be adjusted by a micrometer drive, which can set the iris at any diameter from slightly less than 1 mm to about 1 cm. The setting chosen for the normal operation is 0.5 cm, which corresponds to a field of view of ~1 mrad (the telescope, with a diameter of 32 cm and an effective performance figure of approximately f/15, has a focal length of 4.8 meters which would result in a field stop diameter of 4.8 mm for a 1 mrad field of view. Figure 23 shows the signal intensity measured, at the altitude of 40 km, as the laser beam is stepped through the center of the telescope field for the two orthogonal axes. The edges of the field of view of the telescope and the edges of the laser beam combine to give the intensity curves shown. These curves are in good agreement with the expected results. The mechanical lever arm used in the beam steering mount causes a 12.5 μrad change in the angle of the mount plate for each micron of stepper motor adjustment. Since this adjusts a mirror surface, the angular change is magnified by a factor of 2. Thus, each micron of adjustment causes an angular change in the beam direction of 25 μrad. The scale for the angular change is shown in Figure 23.
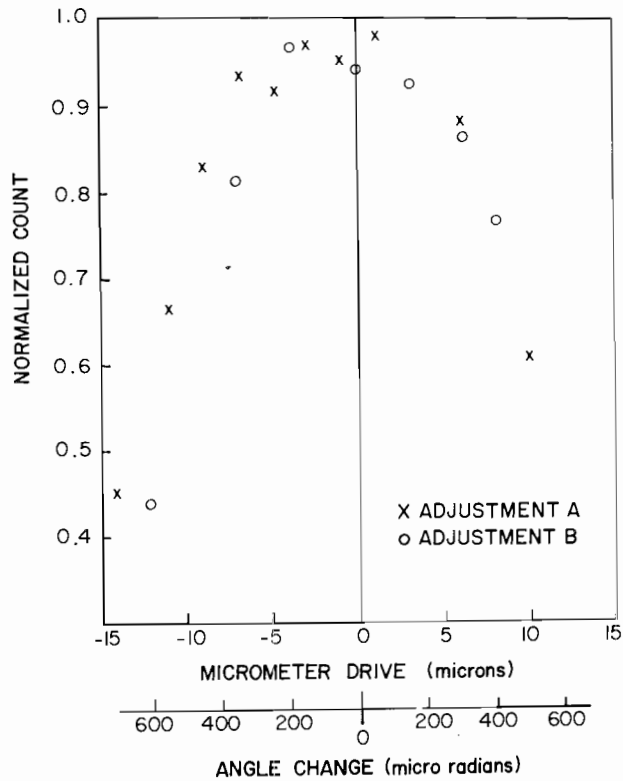
Figure 23. The Signal Intensity at 40 km Altitude is Shown as the Beam Steering Drive is Moved on Two Orthogonal Axes Through the Center of the Telescope Field of View.

7.4 Comparison of Lidar and Rocket Results

This campaign represents the first serious attempt to compare the measurements from standard meteorological rockets with lidar measurements of the atmospheric structure. Two small earlier comparisons were made with the lidar at Wallops Island, VA in September and December 1985. Those results showed that the lidar derived profile and the meteorological rocket profile were in general agreement. During the campaign in Alaska, a total of 10 datasondes and 10 passive spheres were launched in conjunction with the lidar measurements. This data set has provided the first opportunity to compare the techniques and evaluate the performance of the lidar, as well as the opportunity to question previous assumptions regarding the standard techniques.

There is a mixture of both excellent agreement and several cases of significant disagreement between the results obtained. Figure 24 shows some examples of the profiles obtained by the lidar and by the meteorological rockets during the program. Figure 24 (a) and (b) show cases where the strongest disagreement between the lidar and rocket occur. These two sets of measurements were both made on 14 February. There is consistency between the two different types of meteorological payloads launched on that night. L1D designates the datasonde results and L2S designates the passive sphere results. While the two meteorological rockets differ from each other in significant ways, concerning the structure features measured in the profiles, the mean values for the density are in good agreement between them. In contrast, the lidar profiles indicate a density about 12-15 percent below the meteorological rocket densities through the altitude region from 30-70 km. The differences seen in these two comparisons were again observed in the results obtained for L3S on 15 February. Many aspects of the data have been investigated to explain the observed differences; however, no resolution has been found. The ultraviolet data has been compared with the visible lidar profiles to be sure that no significant particulate scattering (Mie scatterers) exists above 25 km. It appears that the tie-on between the lidar data and the Rawinsonde data near 30 km is valid. The lidar data curves show the size of the $\pm 1\sigma$ error bars on the profiles. One of the ideas which was investigated to attempt to explain the differences was whether the altitude could be in error. A difference of a few microseconds in the pulse timing could make a significant error in the density assignment to a particular altitude, because the density decreases at 15 percent per kilometer. The lidar data and radar data (checked for beacon pulse delay mode of operation) were carefully checked and this possibility has been eliminated. The differences observed in these cases are still under investigation. By contrast, the results through most of the rest of the program show general agreement in the mean and in many detailed features observed by the lidar and by the meteorological rockets. Figure 24 (c) and (d), for example, show the results from L7D and L8S measurements of a datasonde and passive sphere compared to the lidar results. In these cases, many of the features observed are in good agreement.

Some degree of confidence in the ability of the lidar to independently define the atmospheric properties was gained from three comparisons between the lidar and datasonde flights. Significant differences existed in those cases and in checking upon the results, it was found that the datasonde calibration curves used for those flights was in error. In the three cases, errors in the calibration data have been corrected by the manufacturer. In two of the cases, the calibration data curves had been inadvertently switched. In general, the data obtained on 27 and 28 April 1986, which was a period of concentrated meteorological rocket measurements, was in good agreement for the altitude range from 20 to 70 km. At higher altitudes, a bias between the results has led to the suggestion that part of the signal return on those dates may have been due to polar mesospheric clouds. The fact that the signal agrees well in both detector systems and the measurements were made after the corrections to the shutter drift problems

72

had been corrected (for the most part), leads to the conclusion that the signal should not be discounted. It is known that the polar mesospheric clouds form over the summer polar cap due to the change in transport and temperature conditions that occur during the summer.

Figures 25 and 26 show a summary of the density and temperature measurements obtained from the meteorological rockets launched during the campaign in Alaska. Figure 25 (a) shows the full set of measurements and Figure 25 (b) shows the 11 profiles that were obtained on 27 and 28 April. An examination of the results has indicated that the standard filter intervals used in the passive sphere analysis may be too short. It appears that the noise level in the radar data would require a longer filter to be applied. An improved analysis of the passive sphere data is presently under study. The datasonde profiles have been corrected using improved calibration data recently supplied by the manufacturer. Figure 25 (a) readily demonstrates the seasonal variation of the atmosphere. The three February measurements lie well below the densities of the other profiles, while the March measurements are grouped between the February and April profiles. The April data shows the onset of summer-like conditions with the mesospheric density increasing to 10 percent above the U.S. Standard in the 70-80 km range. By mid-summer the density would be expected to be 30-40 percent larger than the U.S. Standard. Figures 26 (a) and (b) show the corresponding temperature profiles for the same met rocket launches. It is obvious while several warming pulses occurred in the stratosphere in February, none of the meteorological rockets were actually launched during a major stratospheric warming period. However, lidar data was gathered during a major stratospheric warming which peaked on 19 February (see Section 6.2).
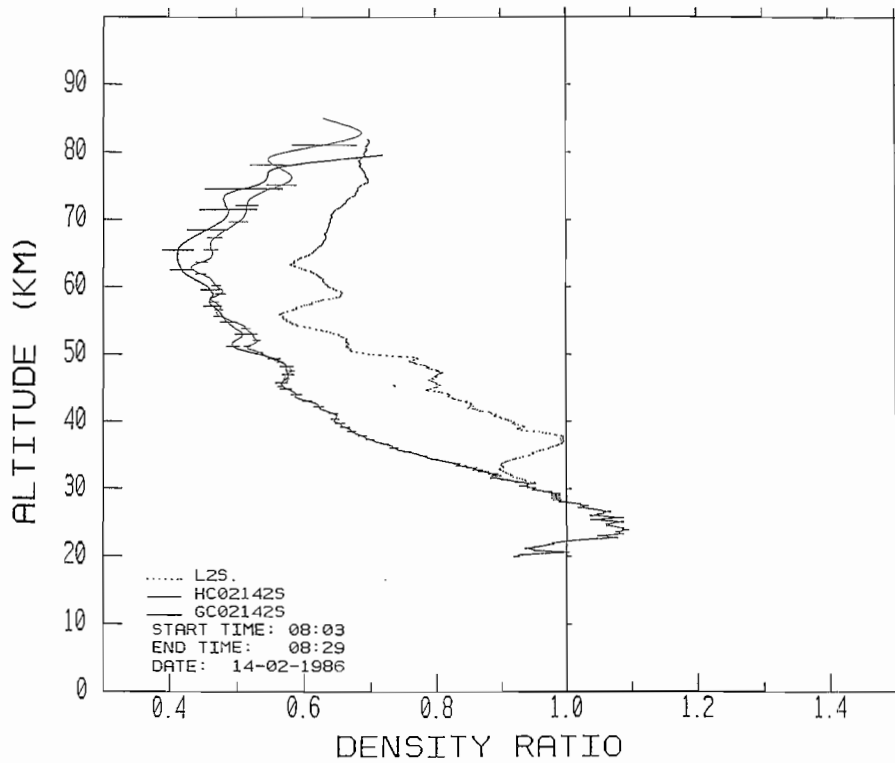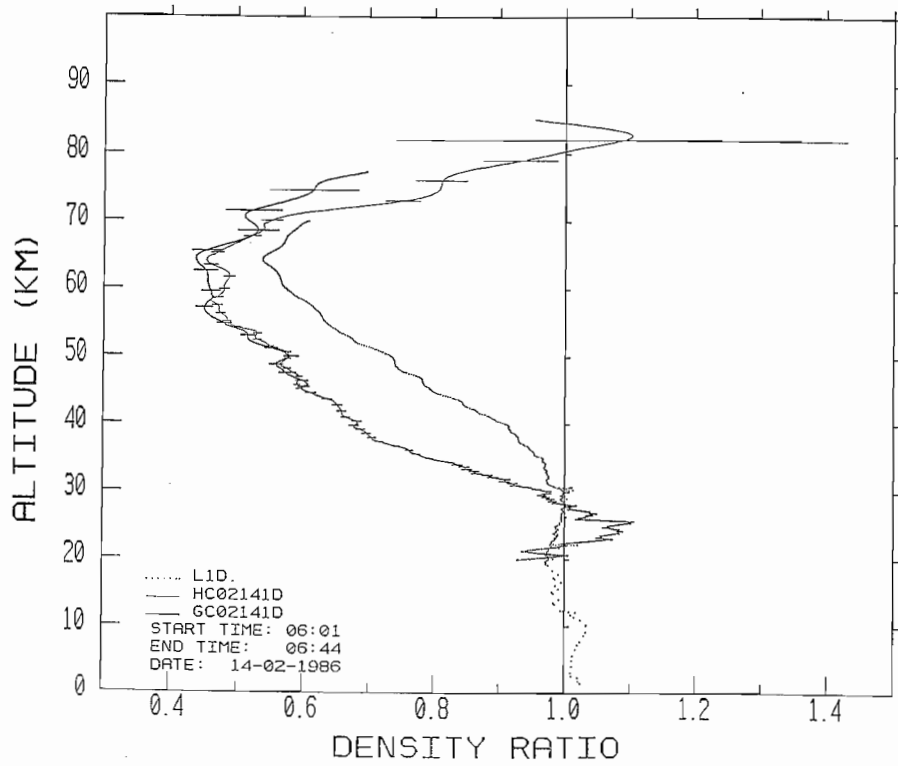
Figure 24. Comparison of Lidar and Rocket Density Profiles (a) Datasonde on 14 February 1986 (b) Passive Sphere on 14 February.

74
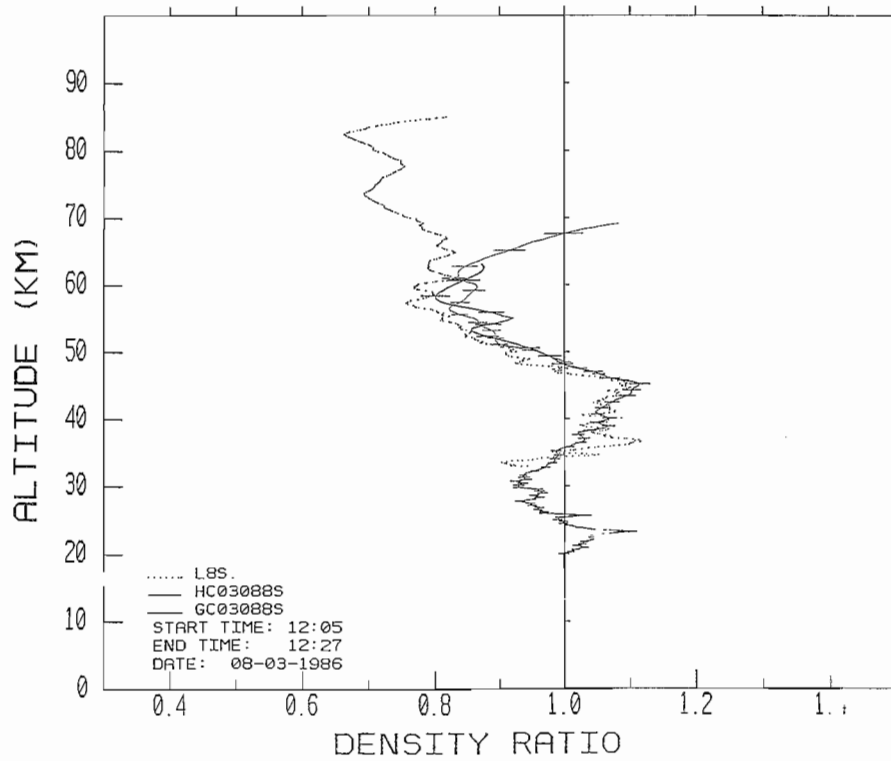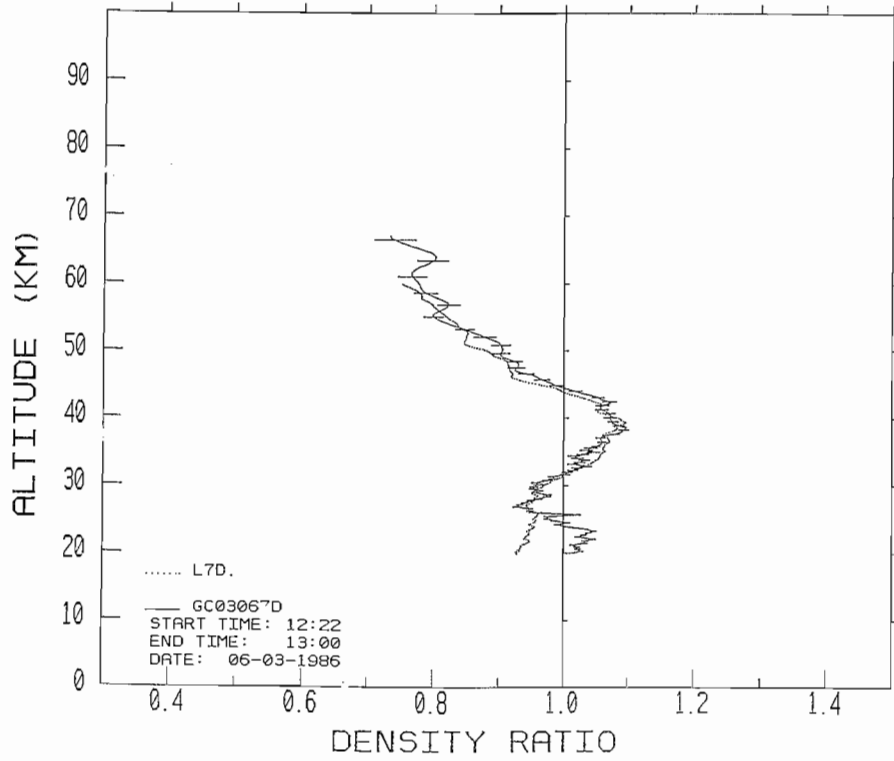
Figure 24. Comparison of Lidar and Rocket Density Profiles   (c) Datasonde on 6 March 1986   (d) Passive Sphere on 8 March 1986.
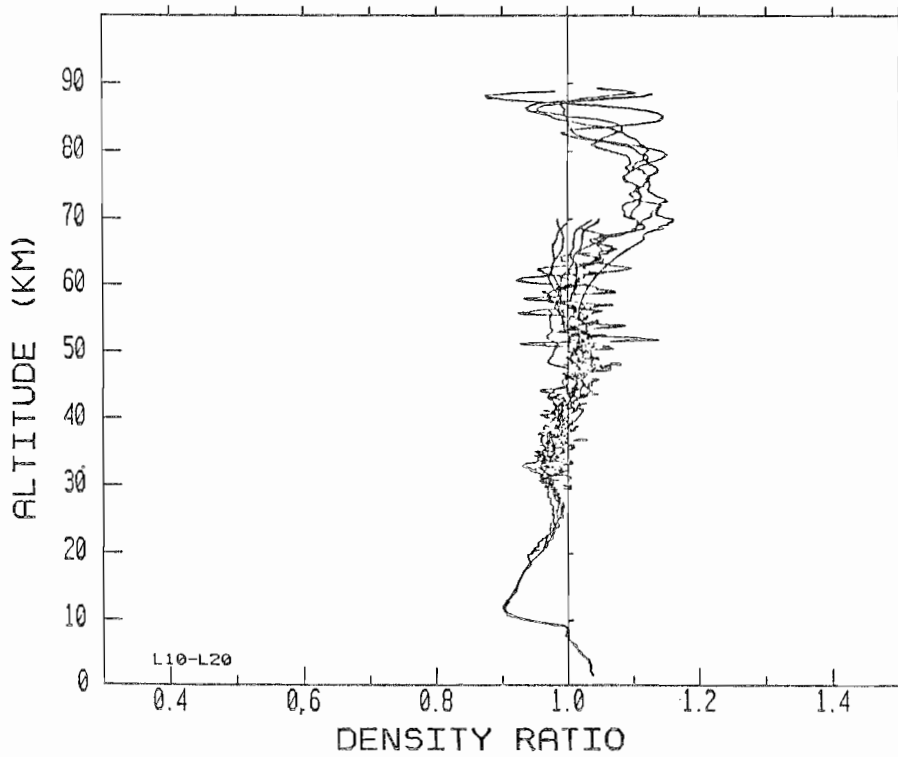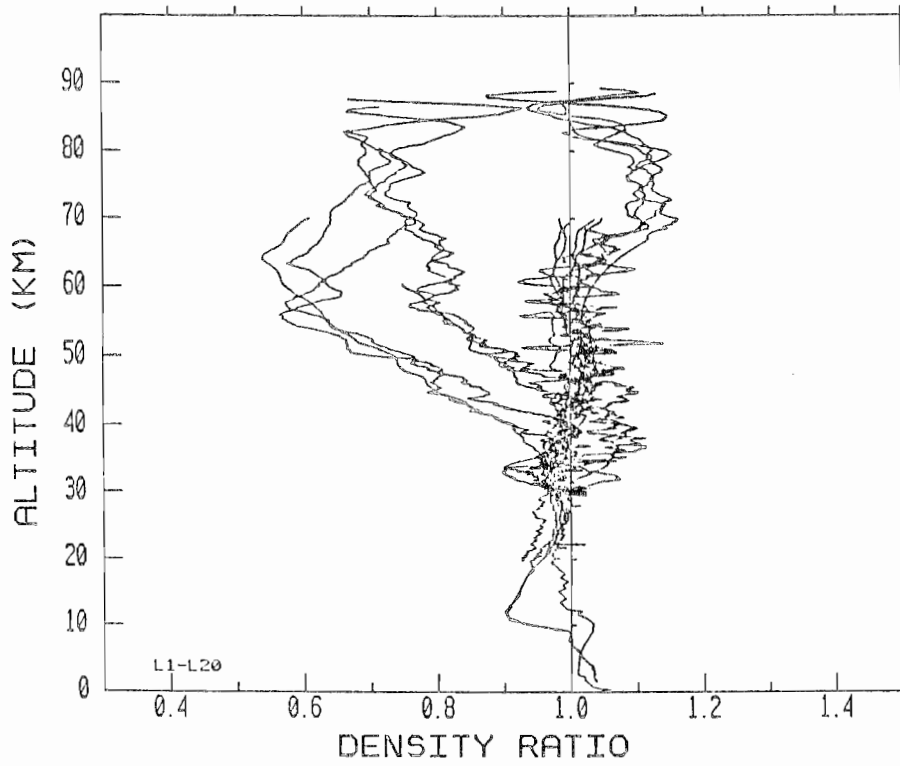
Figure 25. Summary Plots of all of the Meteorological Rocket Data Obtained During the Campaign. (a) Summary of all rocket density measurements (b) Summary of the 11 rocket profiles obtained on 27 and 28 April 1986.

76
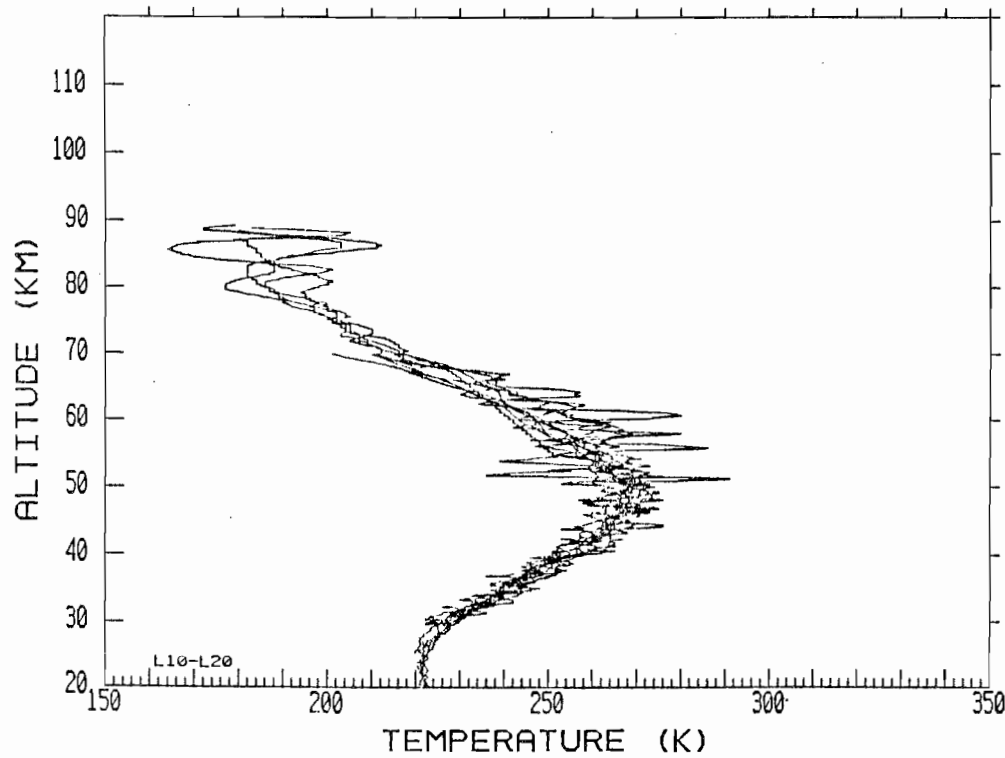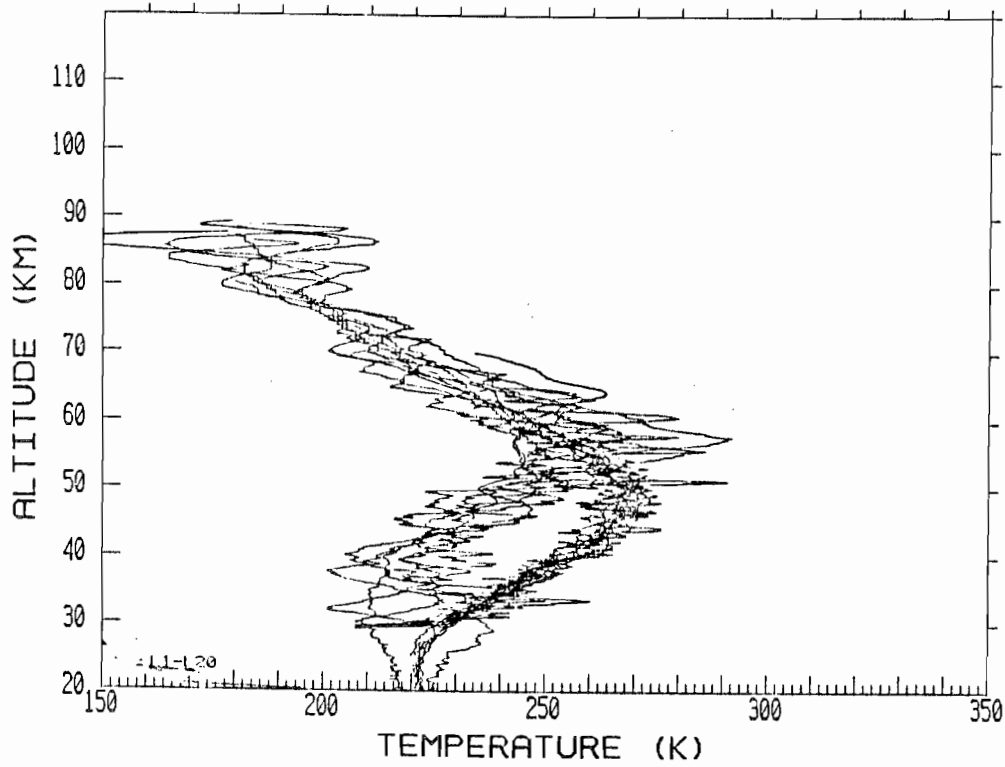
Figure 26. Summary Plots of all of the Meteorological Rocket Data on Temperature During the Campaign. (a) Summary of all rocket temperature data (b) Summary of the 11 profiles obtained on 27 and 28 April 1986.

8. INTERPRETATION OF RESULTS

8.1 Short Time Variations in Structure

The lidar results provided a unique opportunity for examining the sequential changes which occur in the middle atmospheric structure. Figure 27 shows an example of the measurement sequence during three hours of the night of 14 February. During this time, the lidar profiles were collected by integrating the return signal for 3,000 laser shots (5 minutes). Small gaps appear from time to time during which procedures such as alignment, calibration, and data transfer were being performed. The interpretation of any results for the altitude region below 25 km is affected by the initial opening of the detector shutter and by the volcanic dust layers which cause a significant contribution to the return signal. For altitudes above 25 km, the density profiles provide a basis for studying density variations from gravity waves, planetary waves, tidal effects, and seasonal variations. The winter atmosphere seldom exhibits periods in which monochromatic wave structure could be observed in such profiles. There are many sources for gravity waves in the winter, but the measured profiles usually exhibit rather random and usually rather weak density fluctuations. This is primarily due to the fact that the observed profile results from the constructive and destructive interference of many superimposed waves. In addition, much of the energy of the waves transported into the 40-60 km region is extracted by the turbulence layers that exist through most of that region during the winter period. It would be expected, at the upper altitudes, that generation of turbulence layers would occur in regions of wave breaking (where the static stability limit of the atmosphere is exceeded, $(\partial \ln \rho)/\partial z > g/C^2$). Examination of the profiles shown in Figure 27 shows that significant variations in the atmosphere occur during periods of 5-10 min. The study of the quick-look results in the field convinced us to make changes in the equipment and operation which would allow collection of data at shorter time periods. The April 27 and 28 data was accumulated for 1,000 laser shots (100 sec) and stored at intervals of about 2 min.

Figure 28 shows the profiles obtained during a 1 hr period on 4 March. Comparison of these results with those of February shows that the wave activity has increased substantially. Also, the low altitude returns associated with the volcanic dust layers have changed significantly. During the campaign, several eruptions of the St. Augustine volcano added to the dust and increased the signal return in the 18-25 km region.

In late April changes were incorporated to allow data collection at a 2-3 minute repetition rate. Figure 29 shows examples of profiles obtained during a measurement sequence on 27 April. It is found that the small-scale variations, which are still significant, appear to be almost random in character. The realization which has come from the data set of the campaign is that the atmosphere contains many irregular features. Density irregularities with horizontal scale sizes of hundreds of meters to tens of kilometers appear as irregular profile

78

features on short time scales because of their transport by the horizontal wind field. For example, an irregularity with a density 2-3 percent higher than the mean and with a horizontal scale size of a kilometer, would be moved past the lidar measurement path by a 10 meter per second horizontal wind within the 100 second measurement period. In fact, it appears that the region of the middle atmosphere could be described as a region of irregularity (or granularity) in the density distribution along any horizontal path. The magnitude of this variation is probably in the range of 2-5 percent under most conditions and would result from the evolutionary process of the dissipation of wave energy within a macroscopic ensemble. Relative to an observation at one point, such as the lidar measurement at a particular altitude or a rocket flight through a particular level, the atmosphere moves past the region. At different altitudes the wind direction changes in magnitude and direction so that the examination of any path through the atmosphere will contain a white-noise-like variation in the structure properties. This point of view is important in understanding and interpreting the results obtained by the lidar and by in-situ rocket flights. The variation along the path is typically in the few percent range. An analogy to the effect described here can be seen by looking at the sky along a path through the atmosphere on a day when clouds are blowing through the field of view. During the time of transit through the field of view, the clouds are essentially frozen in the time scale of their evolutionary process and a large variation in transmission along a line of sight is observed as the cloud passes. A similar effect is a major contributor to the scintillation of stars by the atmosphere. The frequency components observed in the intensity variation are contributed to by the irregularities moving through the path from different directions and with different amplitudes, scale sizes and velocities at each altitude. Based upon these realizations, a view of the atmosphere should be adopted which allows a few percent of white noise-like background, which does not have to be explained when two independent measurements are compared, unless they are measuring exactly the same volume at the same time.

Another way of visualizing the variations which occur during the night is shown in Figure 30. The data from the profiles can be extracted at constant altitude levels to better observe the variations in density with time. Figure 30 shows the sequence of measurements from 0700 to 1300 GMT for 27 April. Some regularity in the features is observed, however, most of the variation is difficult to visualize relative to the scales and periods of waves present in the atmosphere.

To study the longer time period variations of the atmosphere, we removed the short period variations by combining all of the profiles obtained during a 1 hr time period. The combination of the data improves the signal to noise character and extends the useful altitude range. The results from the G profile are believed to be final. An attempt to compare the profiles has led to the data presentation shown in Figure 31. The data from each of the eighteen nights on which more than four hours of data was collected are summarized in Figure 31 (a) through (r). This presentation allows the longer period gravity waves, planetary waves, and other features to be seen more clearly. The profiles of 14 February, Figure 31 (a), exhibit rather smooth character through the

altitude region between 30 and 50 km. On 15 February, Figure 31 (b), the beginning of a stratospheric warming can be seen in the altitude region near 45 km. By 16 February, Figure 31 (c), the density in the 45 km range has increased by more than 30 percent over the profiles of 14 February. The changes that occur during the night of 16 February are striking. February 17, Figure 31 (d), continues with the minor warming pulse that is characteristic of the profiles late on 16 February. On 18 February, Figure 31 (e), the atmosphere begins to return to more normal conditions. However on 19 February, Figure 31 (f), a full stratospheric warming has developed, which apparently continued through the 20th, 21st and 22nd [see Figure 31 (g)] of February. On 24 February, Figure 31 (h), the atmosphere is obviously still in the disturbed condition remaining from the stratospheric warming but shows the tendency to return to expected conditions. The results on 27 February, Figure 31 (i), are interesting because relatively large structure features, up to &8 percent are observed in the region near 50 km. The measurements in the period 2 March to 5 March, Figures 31 (j) through (m) contain a large amount of wave activity. Beginning on 6 March and continuing through 8 March, Figures 31 (n) through (p) exhibit a large relative increase in density in the altitude region of 35-45 km, which would be characteristic of a minor stratospheric warming. The results of 27 and 28 April, Figures 31 (q) and (r), exhibit profiles typical of expected conditions for early summer. The higher altitude regions, above 70 km, are unusual in that the density appears to increase by a large factor above the U.S. Standard Atmosphere. While density profiles in mid-summer increase to values of 40 percent above the model, it is unlikely that the density profile could exhibit the response shown. Comparison of these results with the meteorological rocket measurements, the sphere flights on 27 April, leads to the conclusion that the upper altitude signal is not due to a Rayleigh scatter density measurement. A proposed explanation for the measurements is that a Mie scattering region associated with polar mesospheric clouds is affecting the profiles measured during late April.

8.2. Day to Day Variations in the Density Structure

The mean profiles for each measurement night are presented in Appendix C. The results of the nightly mean profiles are summarized in Figure 32. The effect of the variations associated with the stratospheric warming pulses is clearly demonstrated in this presentation. The time sequence of these profiles is similar to that which has been analyzed from the MAP-WINE data, where the components of the planetary wave field have been extracted. It becomes apparent that it may be possible to predict stratospheric warmings based on analysis of the wave components which combine to produce the conditions of minor or major stratospheric warmings and mesospheric coolings. Another significant point that can be extracted from the results is that the wave amplitudes are larger in the mesosphere during the period of a stratospheric warming. In this case, the region around 50 km becomes more stable, allowing waves to grow as they propagate through this region rather than giving up their energy to turbulence there. This change toward summer-like stability conditions results in larger amplitude waves in the mesosphere. The few summer measurements which are available exhibit large amplitude waves that are more nearly monochromatic than in the winter profiles.

8.3. The Future for the Lidar Sounder

These measurements have provided the first opportunity for evaluating the performance of a lidar under field conditions where simultaneous measurements of standard meteorological techniques could be obtained. Most of the comparisons are encouraging, but there are some significant differences in a few cases where additional study is required. A long term goal is to evaluate the lidar capabilities and develop the technique sufficiently that it can be produced and used as a dependable tool in supporting the national range operations by providing required data on atmospheric and meteorological conditions. It is expected that the lidar will replace a majority of the meteorological rocket observations wi' iin a five to seven year time frame. In the meanwhile, a large community of scientists and meteorologists will need to be convinced of the capabilities the lidar can offer. These initial tests have laid the groundwork for the evaluation. During the next three years, a concentrated effort should carefully consider the accuracies and capabilities of the lidar and carefully evaluate the current measurement techniques. Several measurement campaigns will be needed to provide the data base for these evaluations. The present study has shown the major value in having sequential measurements during a night and during many nights to evaluate the atmospheric variability, its dynamical conditions, and for interpreting many of the current scientific topics regarding the physics of the atmosphere.
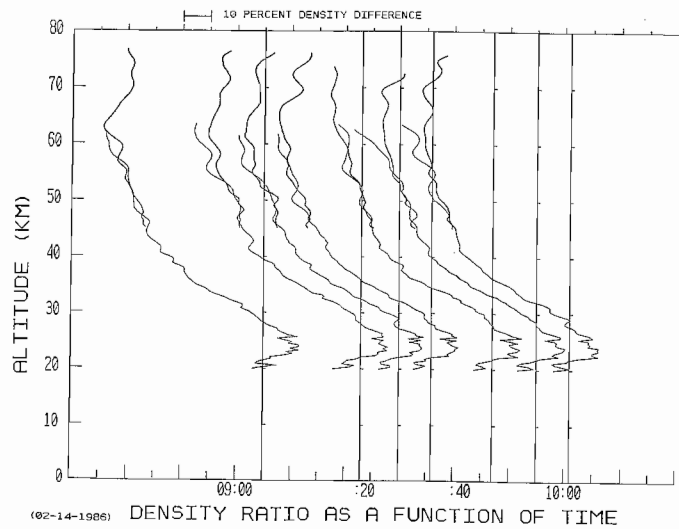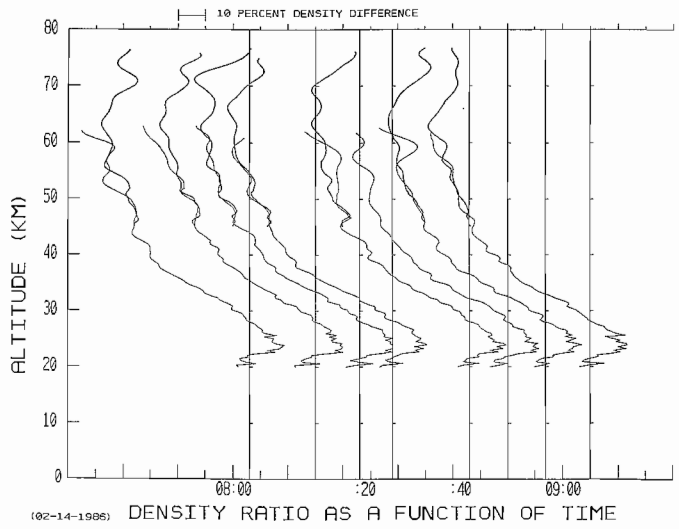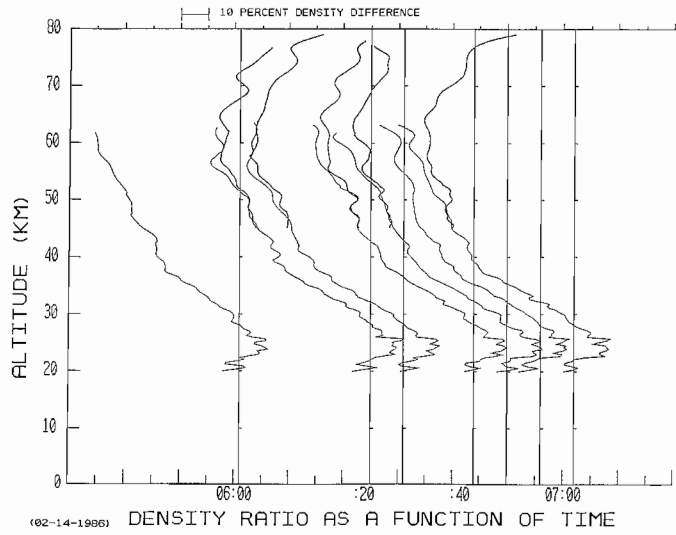
Figure 27. Sequence of Lidar Profiles of Density Measured on 14 February 1986.
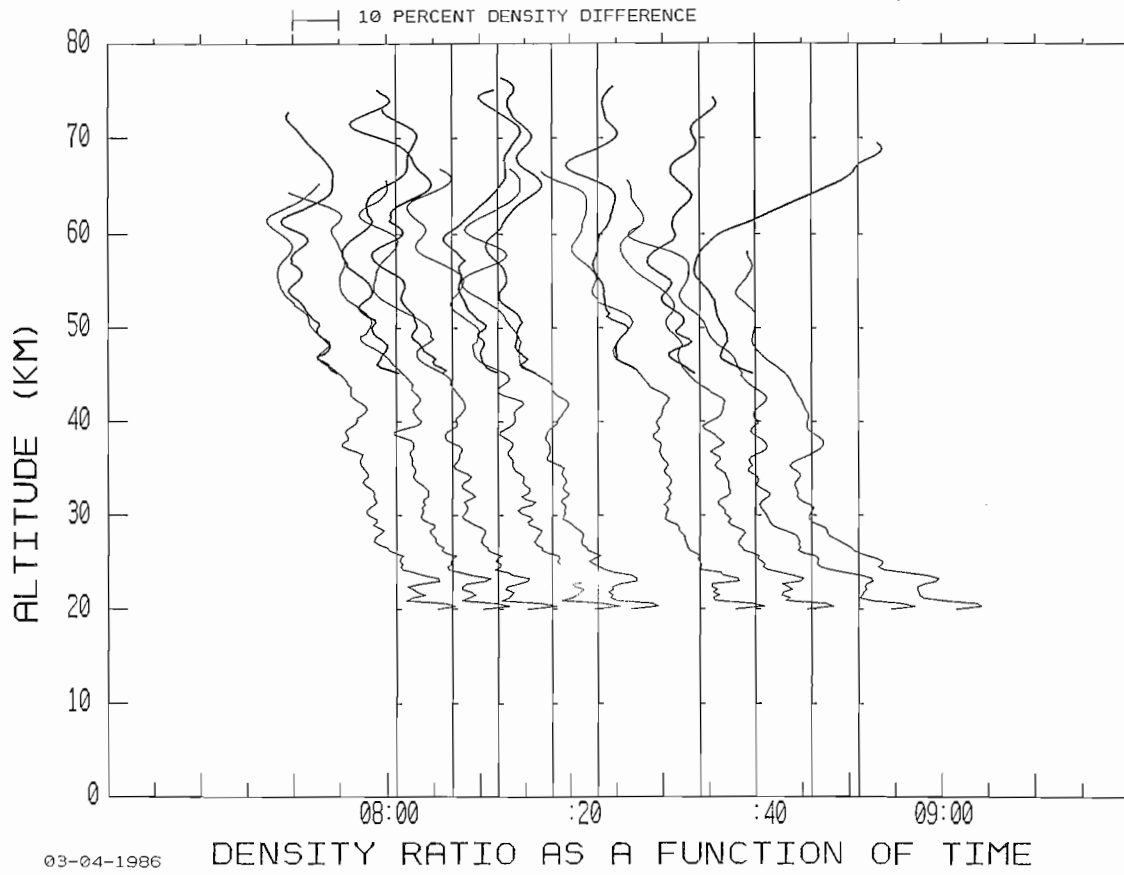
Figure 28. Example of the Time Variation of the Density Profiles Measured on 4 March 1986.
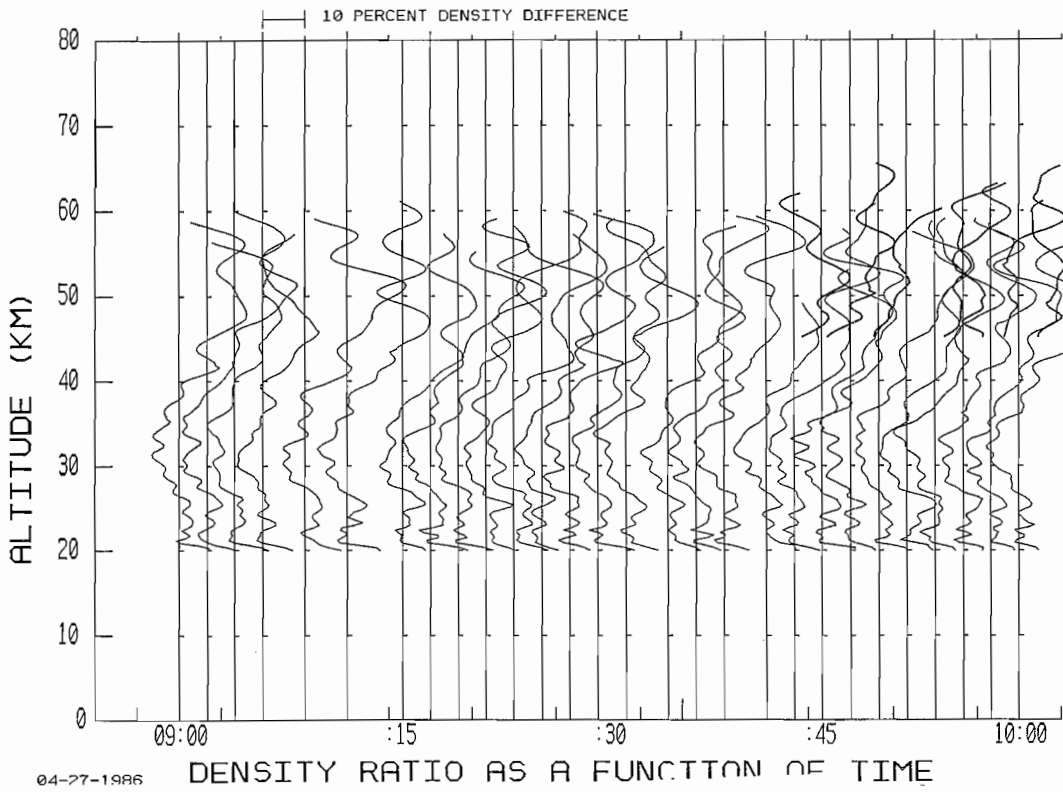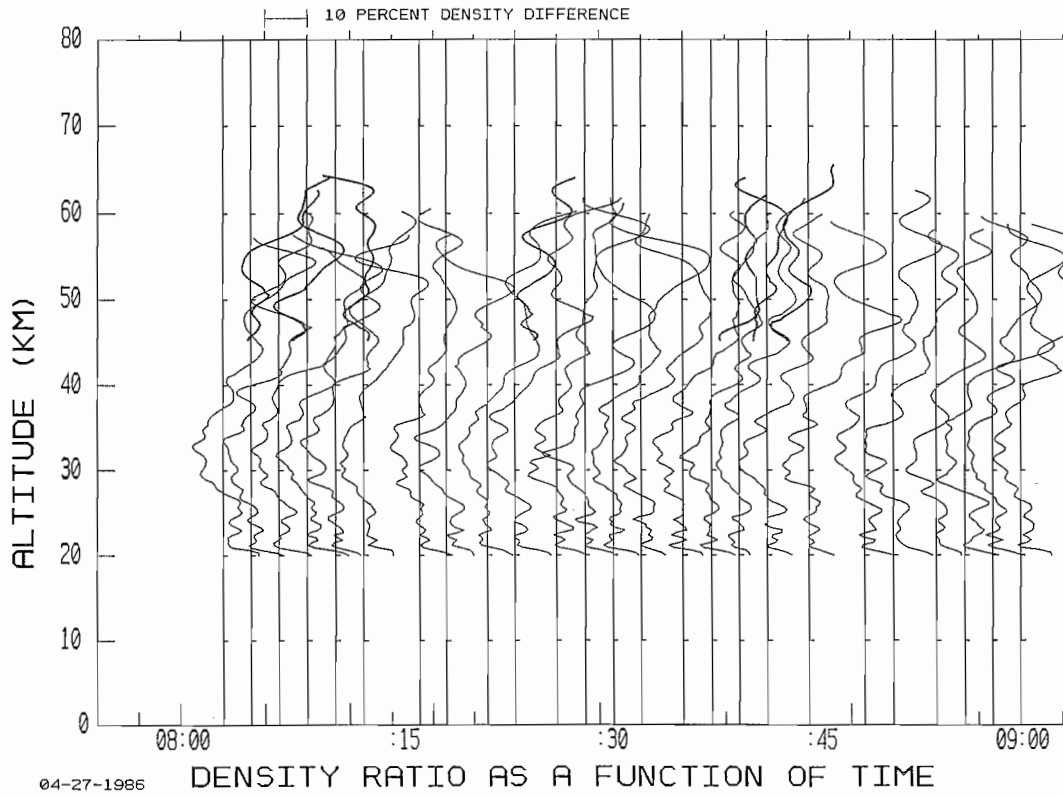
Figure 29. The Time Variation of the Density Measured on 27 April 1986 with 100 Sec Integration Time.

84
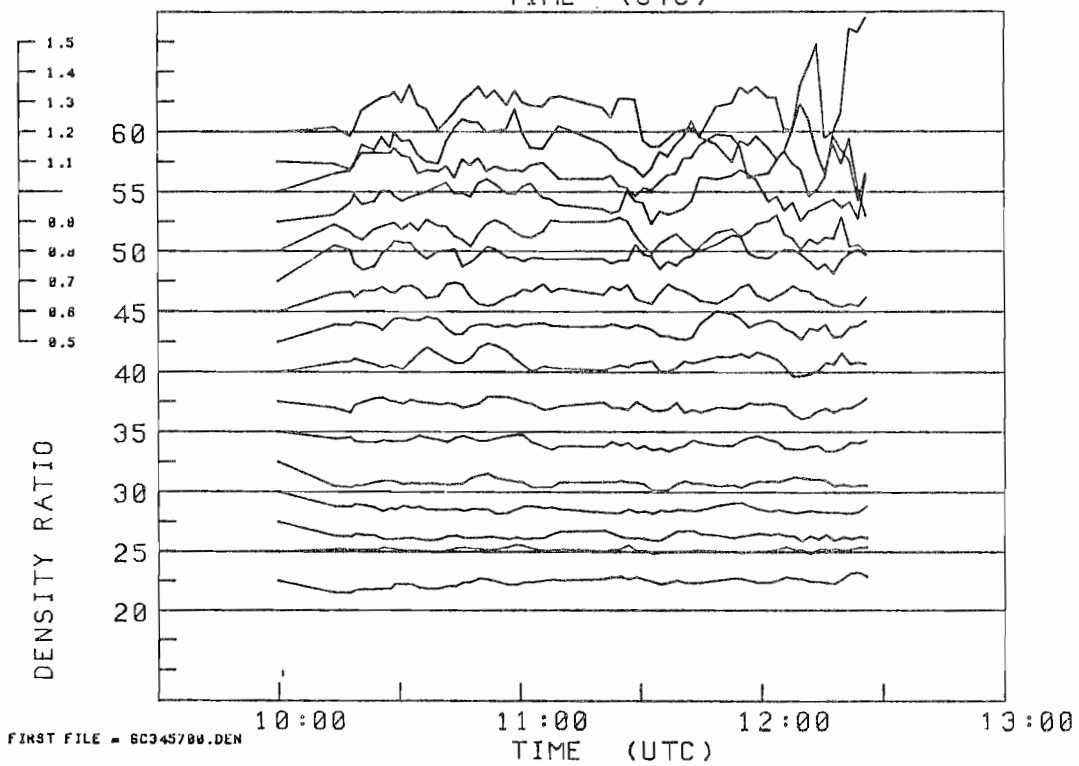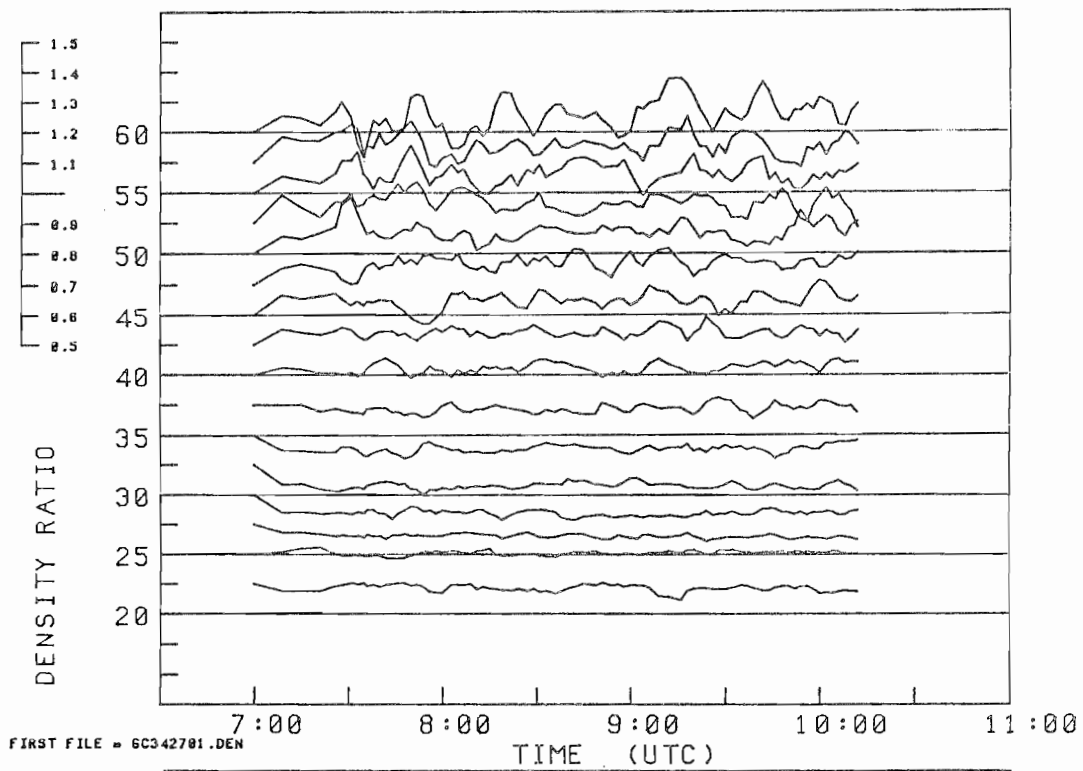
Figure 30. Time Variation of the Density at Constant Altitude Provides Another Way to Observe the Atmospheric Structure for Measurements of 27 April 1986.

85
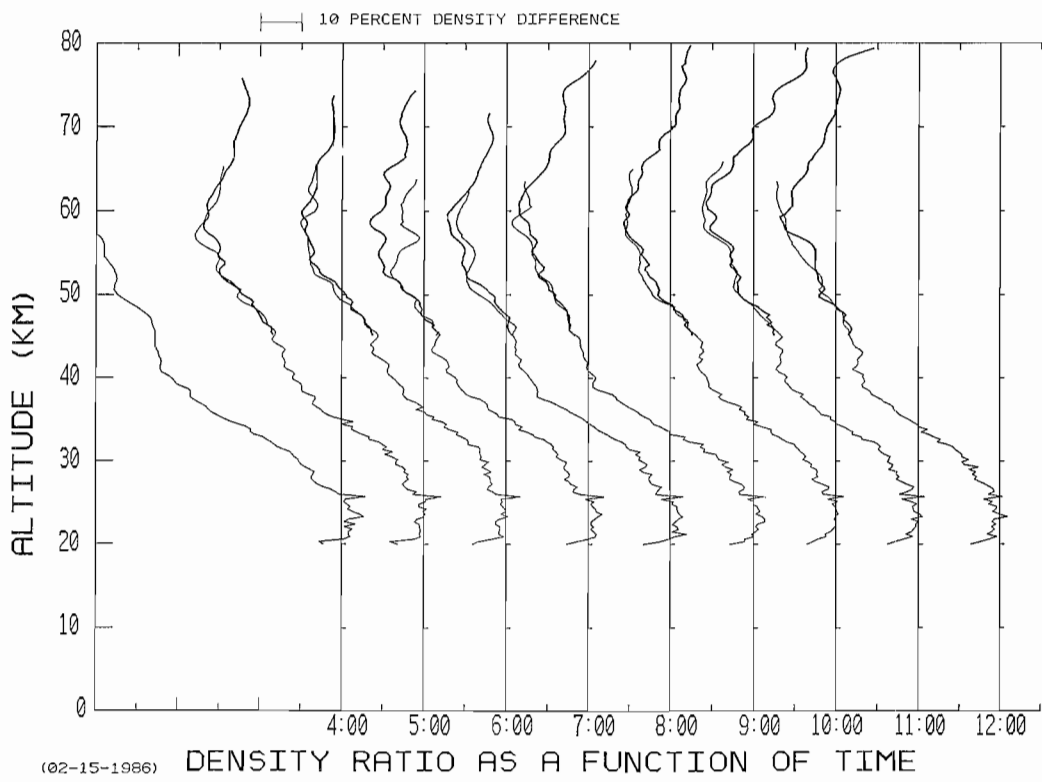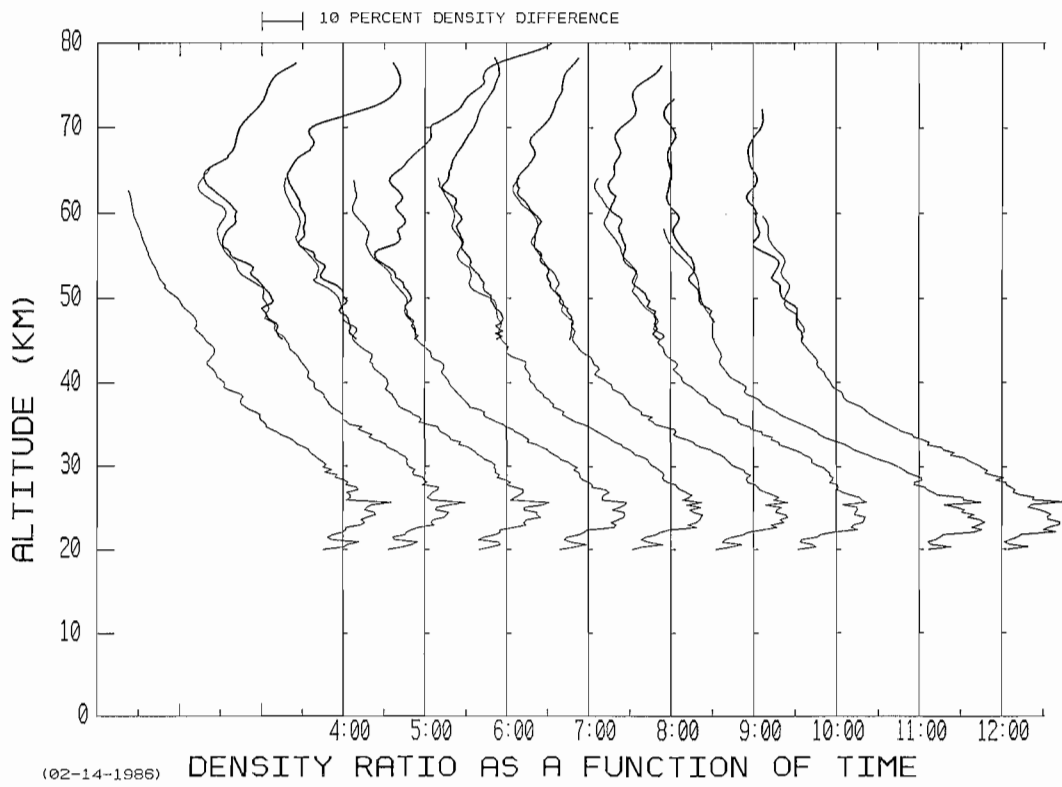
Figure 31. Hourly Mean Profiles of Atmospheric Density (a) 14 February 1986 (b) 15 February 1986
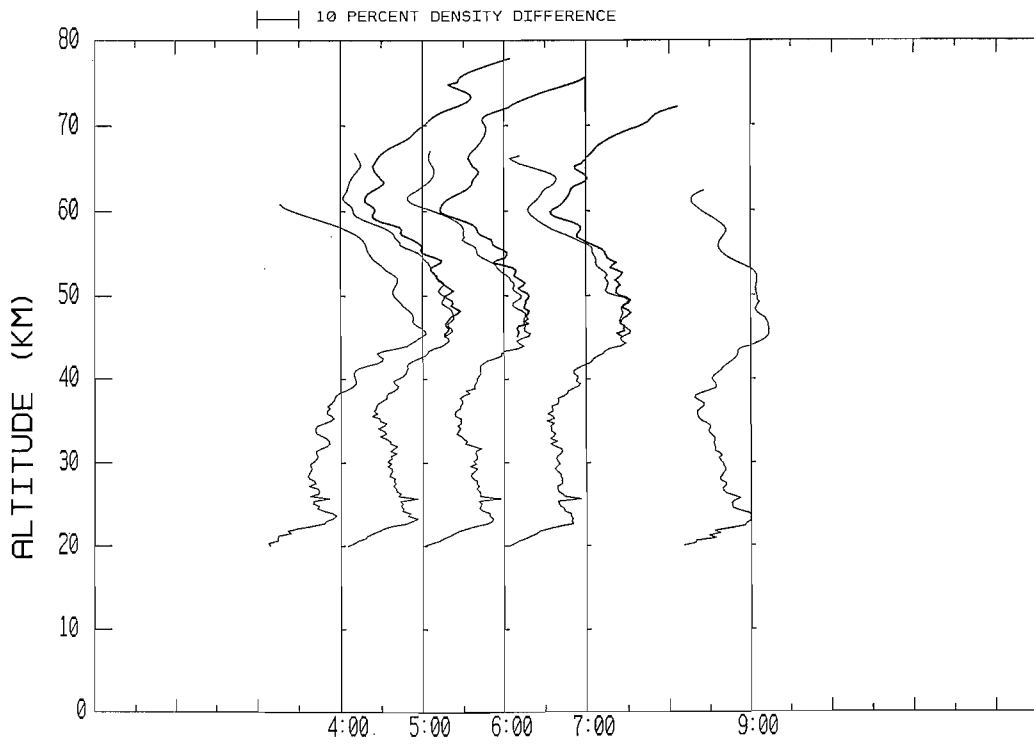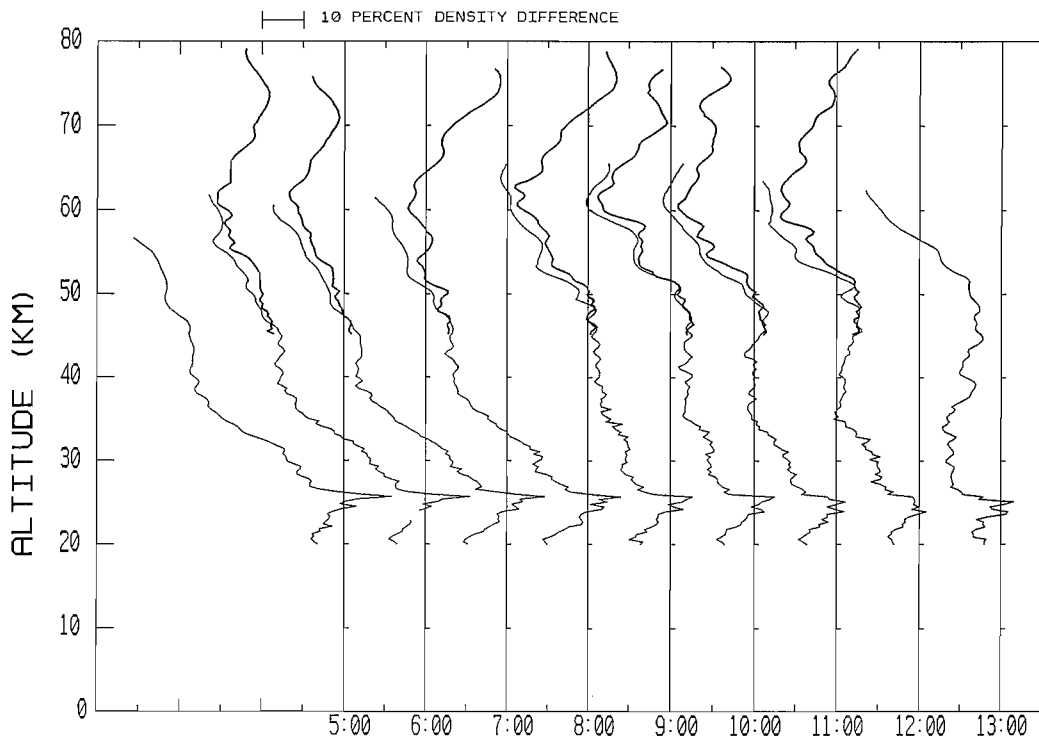
Figure 31. Hourly Mean Profiles of Atmospheric Density (c) 16 February 1986 (d) 17 February 1986
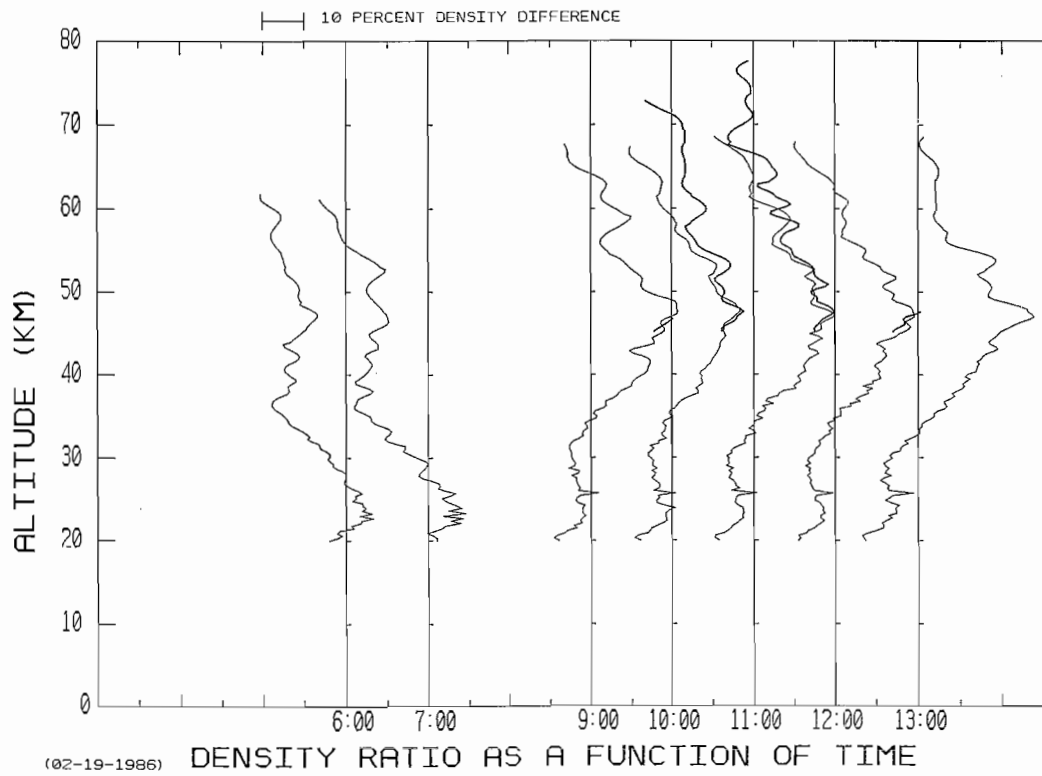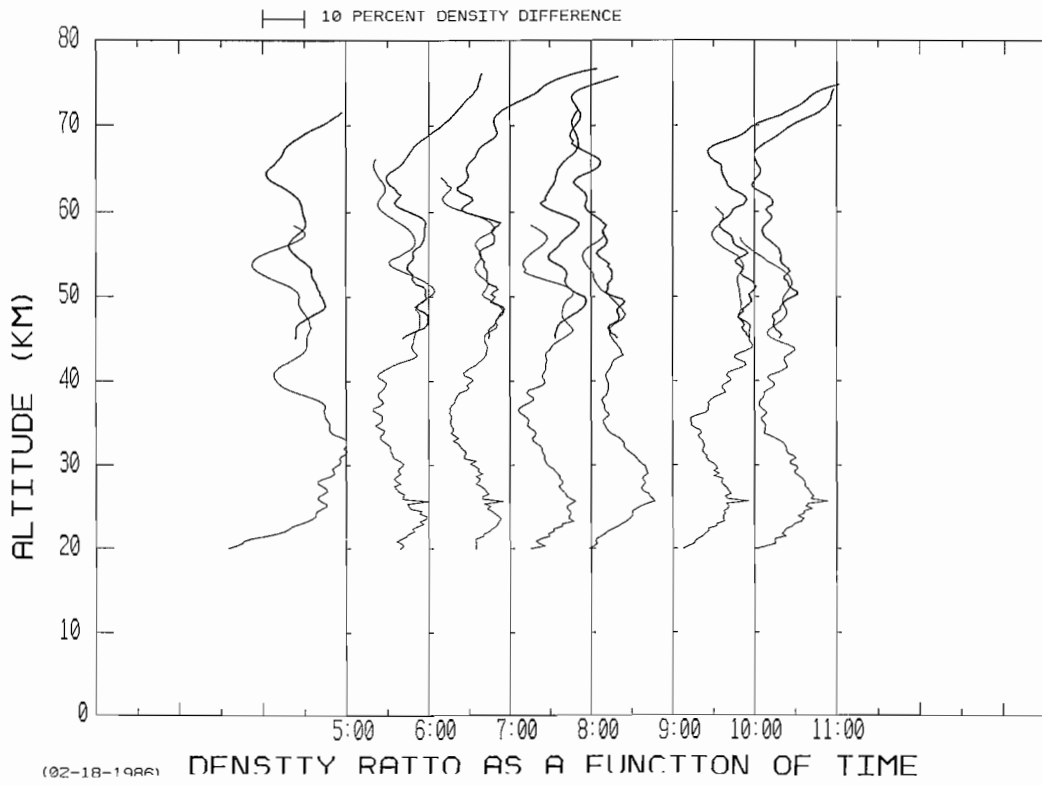
Figure 31. Hourly Mean Profiles of Atmospheric Density (e) 18 February 1986 (f) 19 February 1986

88
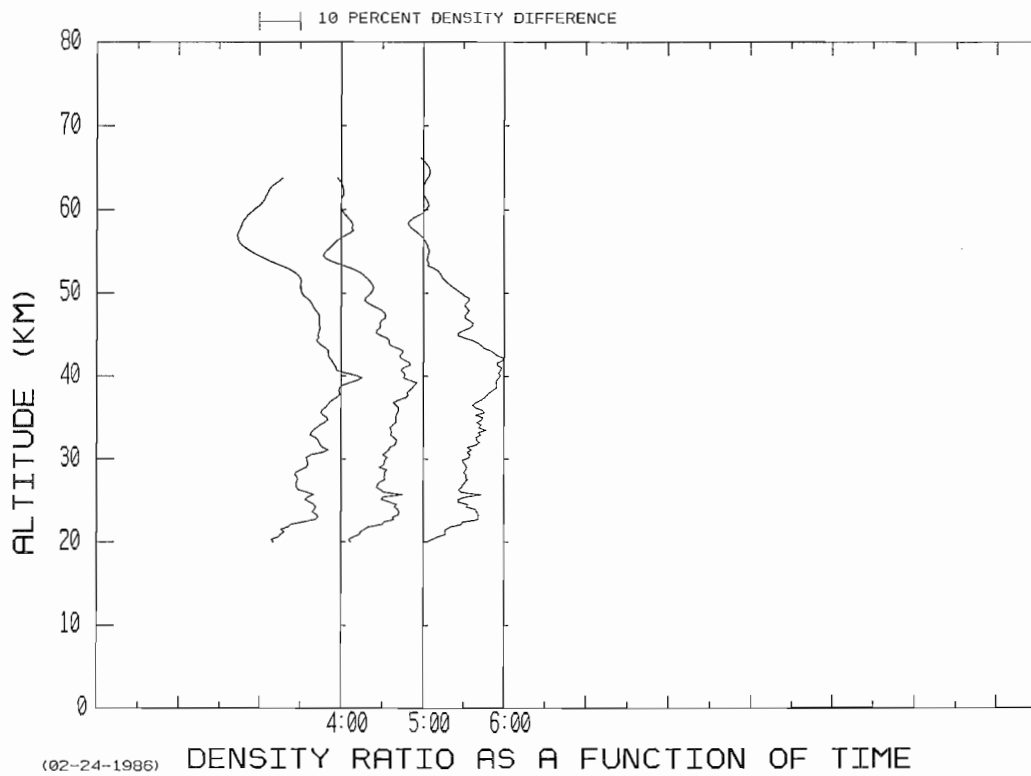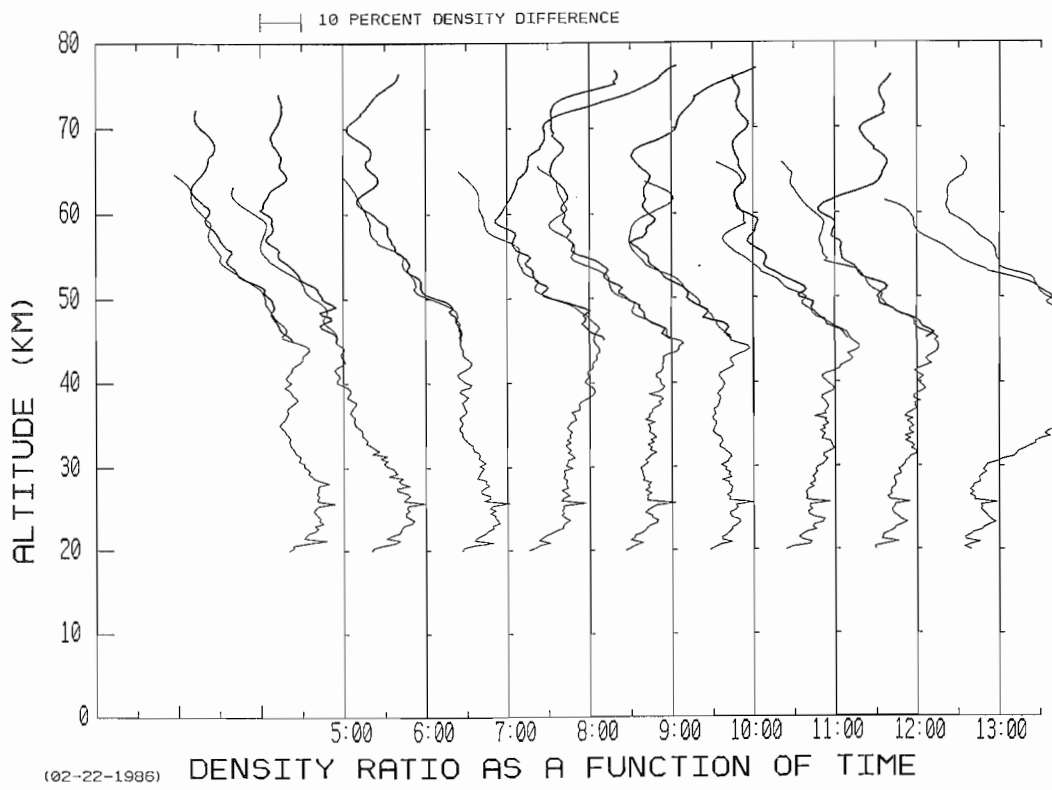
Figure 31. Hourly Mean Profiles of Atmospheric Density (g) 22 February 1986 (h) 24 February 1986
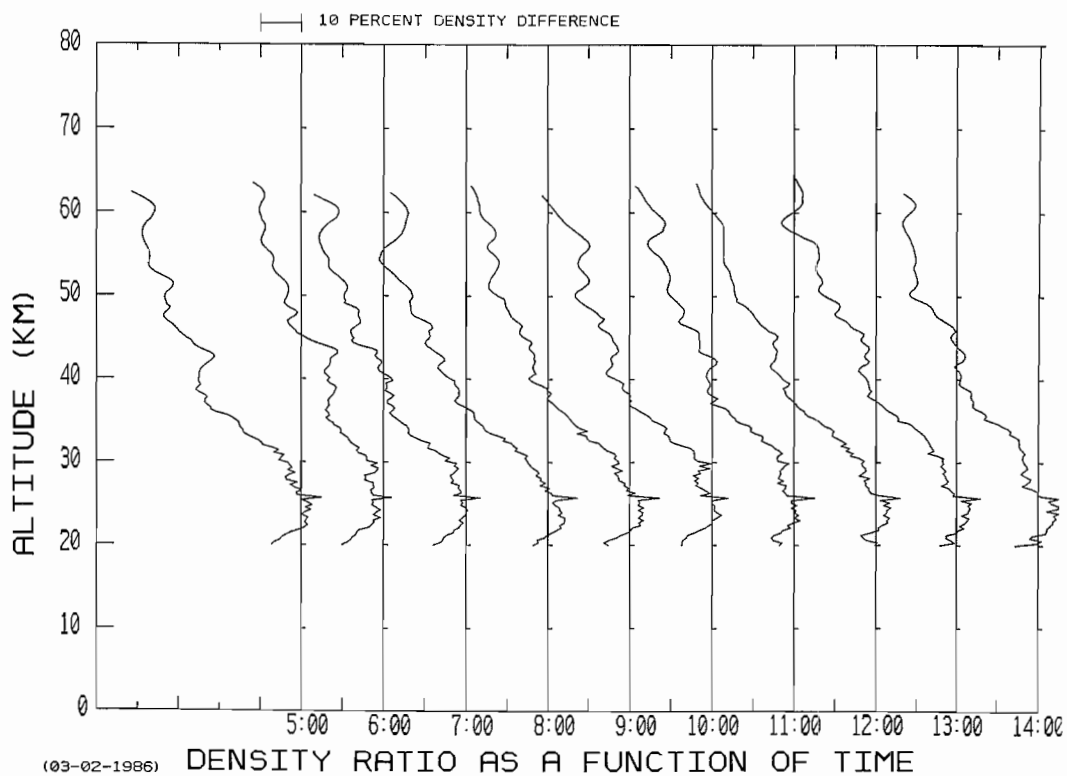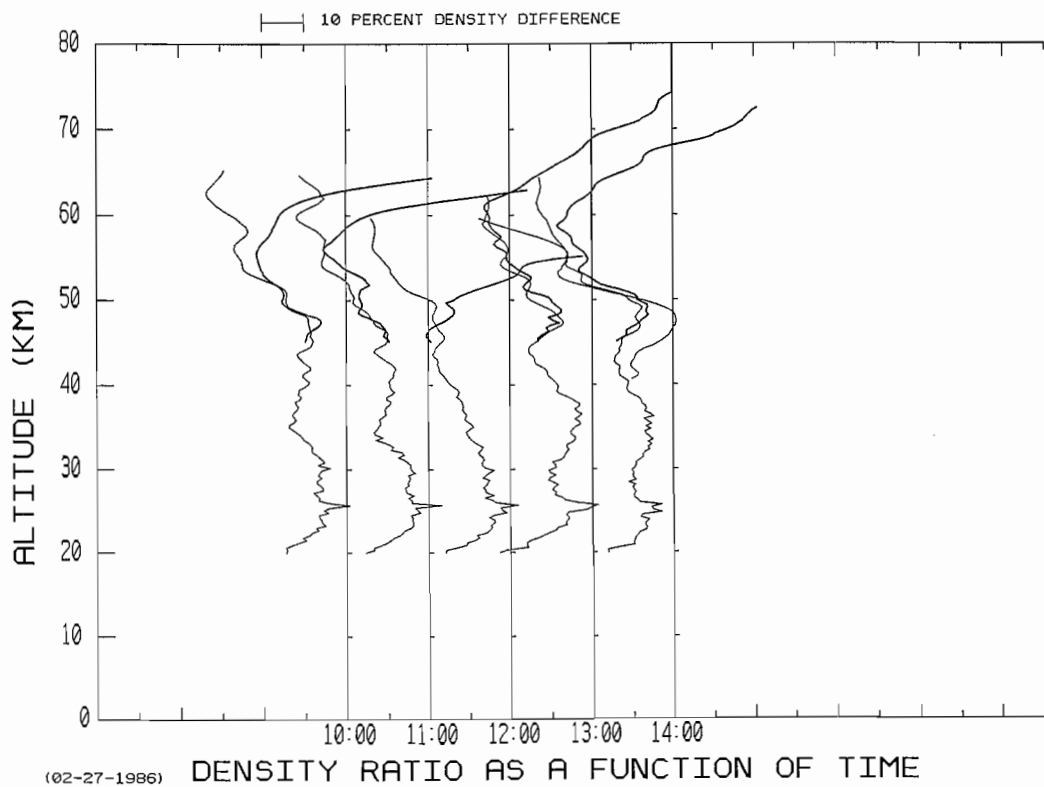
Figure 31. Hourly Mean Profiles of Atmospheric Density (i) 27 February 1986 (j) 2 March 1986
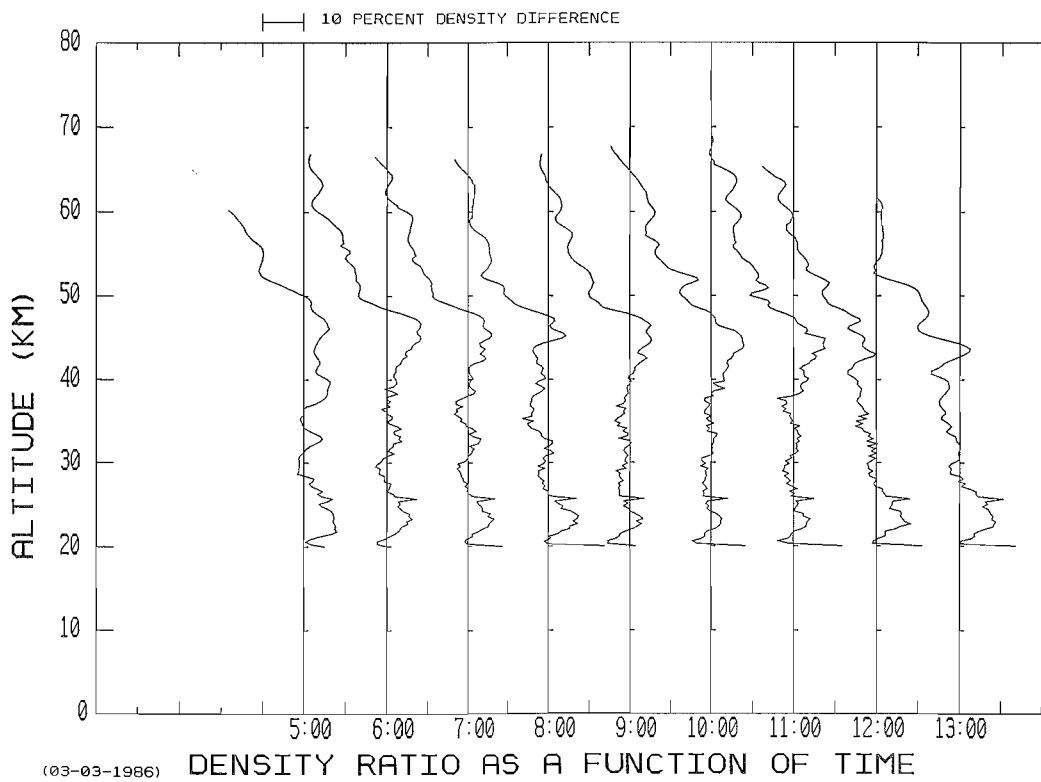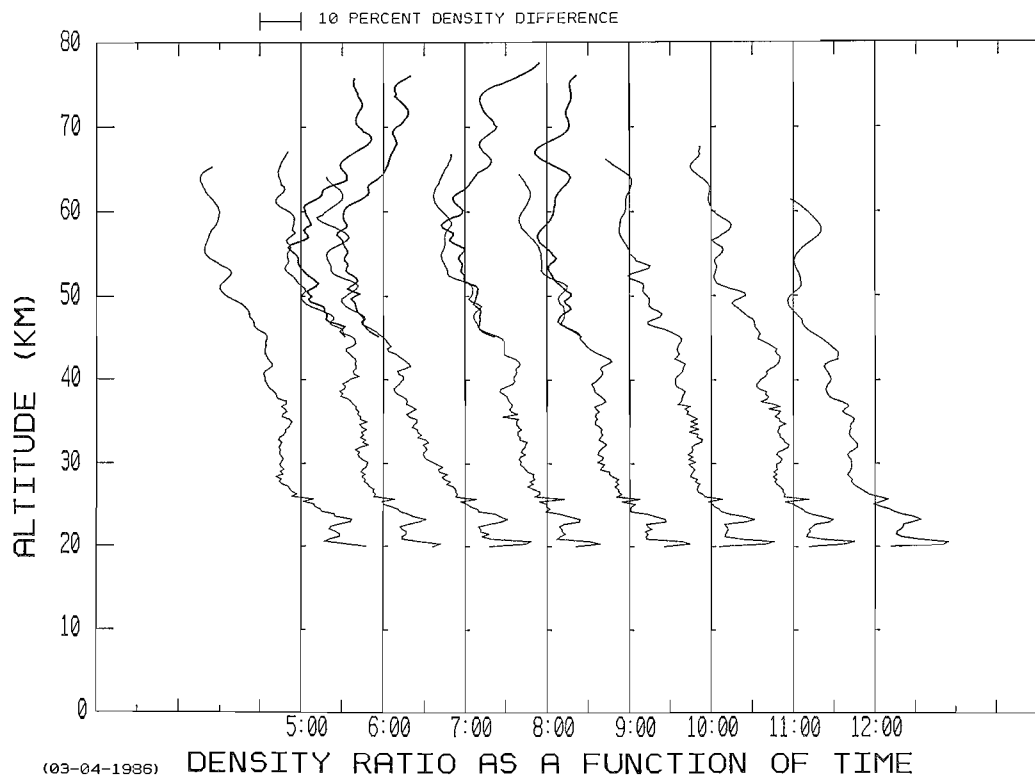
Figure 31. Hourly Mean Profiles of Atmospheric Density (k) 3 March 1986 (l) 4 March 1986

91
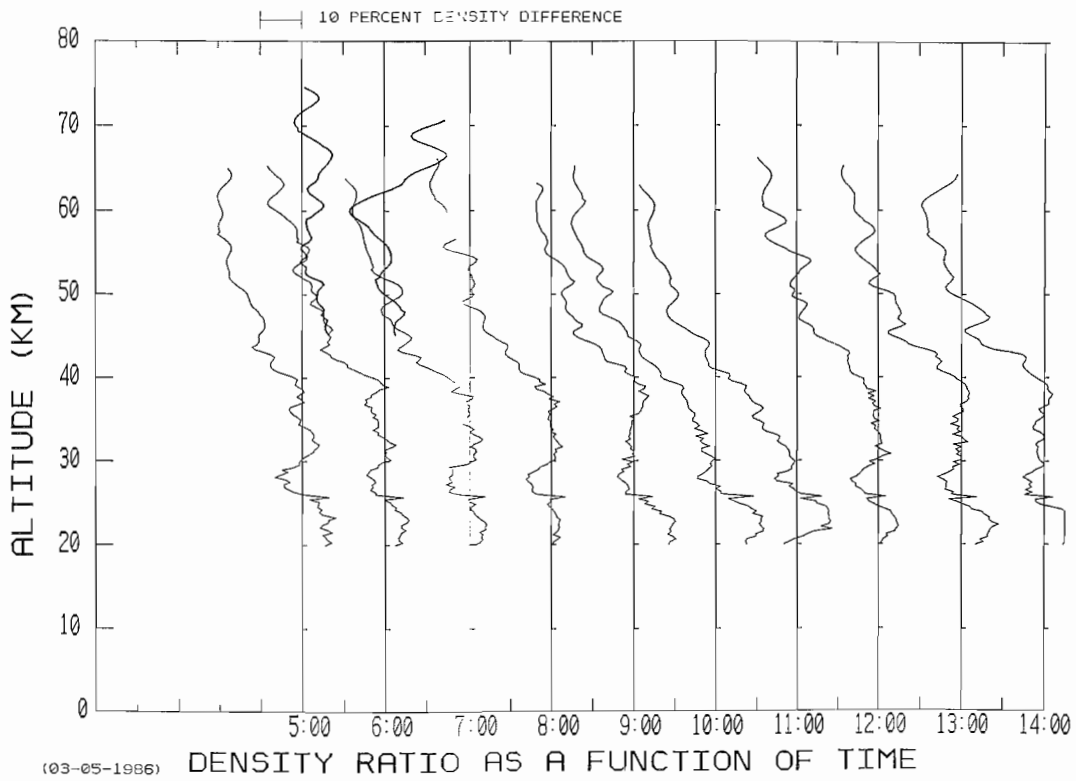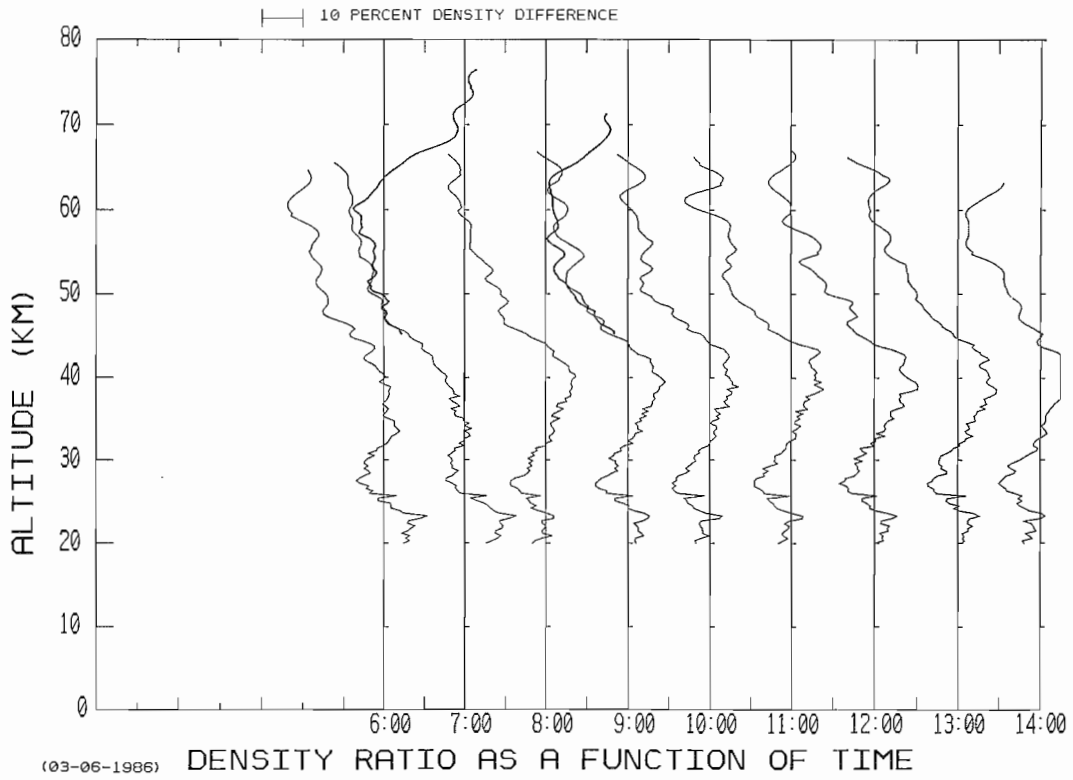
Figure 31. Hourly Mean Profiles of Atmospheric Density (m) 5 March 1986 (n) 6 March 1986
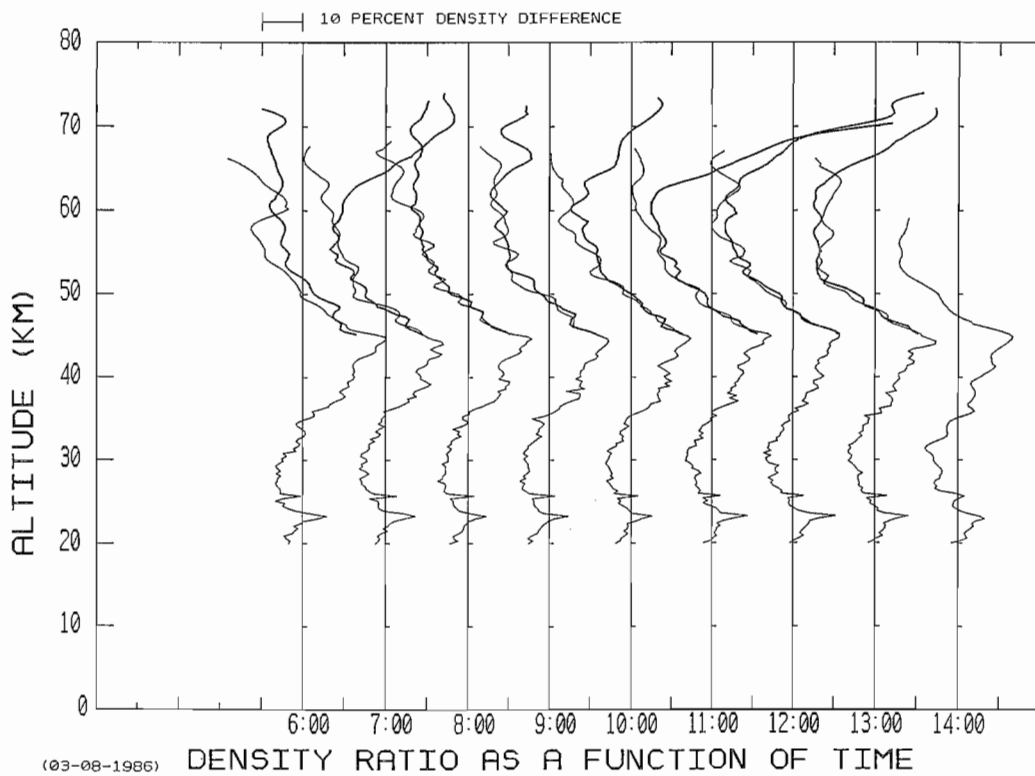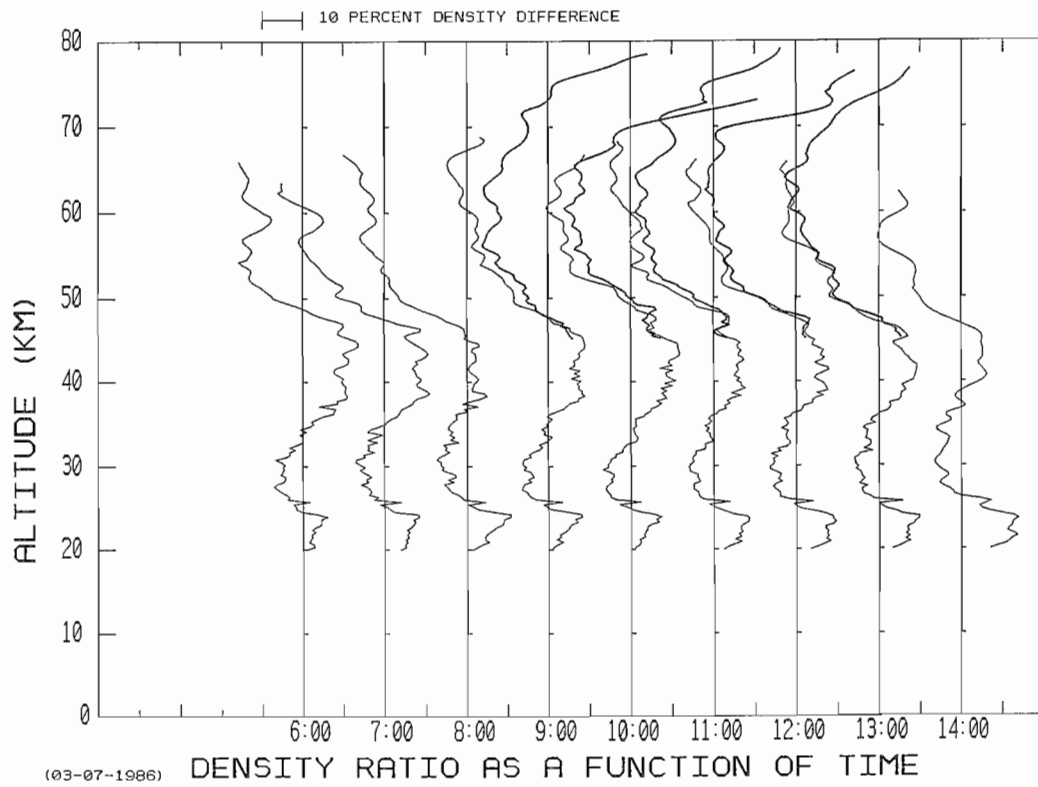
Figure 31. Hourly Mean Profiles of Atmospheric Density (o) 7 March 1986 (p) 8 March 1986

93
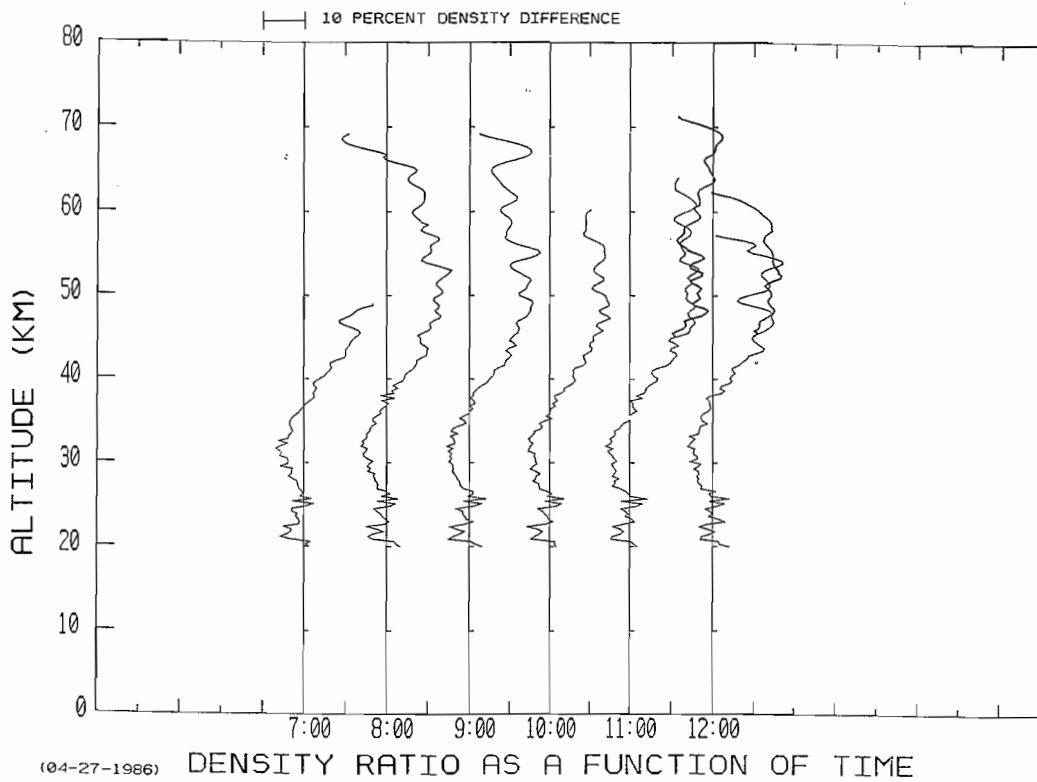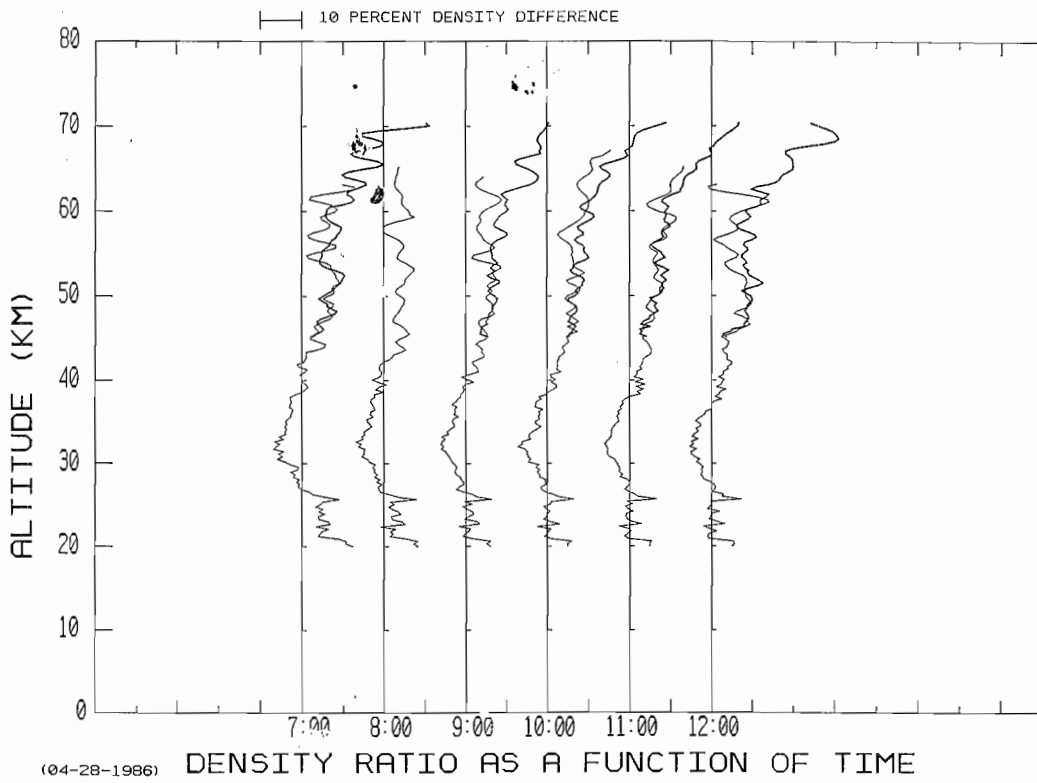
Figure 31. Hourly Mean Profiles of Atmospheric Density (q) 27 April 1986 (r) 28 April 1986

94
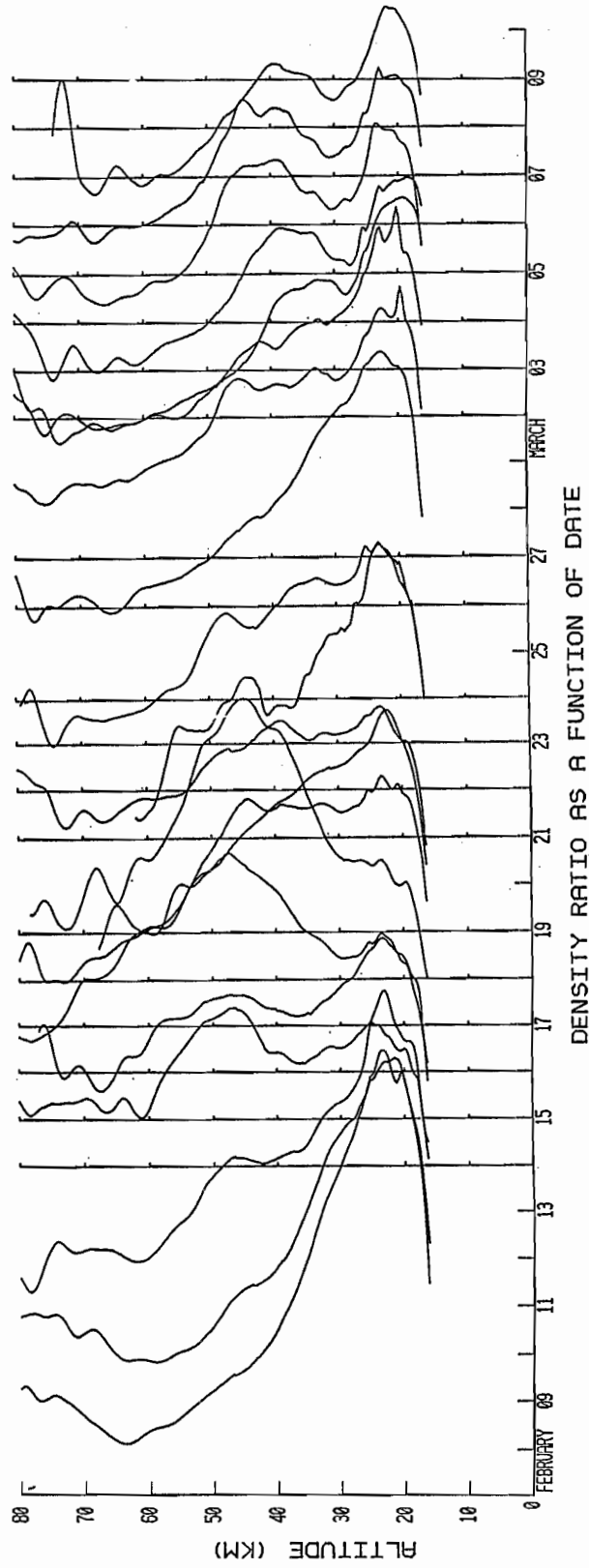
Figure 32. Nightly mean profiles for the sequence of measurements from 14 February – 9 March 1986.

APPENDIX A: COMPARISON OF DATA FILTERS

The LIDAR data are collected by photon counting and as is usual in such a system there are atmospheric regions that produce such a weak return that smoothing is needed to reduce statistical fluctuations in the data. Several different smoothing procedures were investigated to determine the best procedure to be used for the data reduction program. Some set of criteria is needed to compare the different procedures with each other and on an absolute basis. The criteria used for this evaluation are:

(1) Simplicity: the smoothing procedure must be easy to implement and must not require an exorbitant amount of computer time for the analysis of typical data.

(2) Accuracy: the smoothing procedure must not add anything to the data. In particular, the smoothed data must not "ring" in response to transient impulses in the raw data. This would add what might look like strong wave components in the data. In particular, the wave structure of the atmosphere will be of interest and the smoothing procedure must not add misleading unphysical responses.

(3) Analyticity: the smoothing procedure must be based on well-defined functions so that the process can be described easily and so that further investigations into the wave structure of the atmosphere will be possible.

A.1 Filters

The first try at a smoothing procedure was a simple sliding average. This procedure was considered marginally acceptable, as it met the above criteria in a general way. However, the smoothed data were still fairly noisy. The noise was mostly high frequency noise generated at the edges of the rectangular smoothing window.

The next procedure used was also a sliding average except that a Hanning window was used for smoothing instead of the rectangular window. This smoothing procedure has a good high frequency cutoff and does not add any ringing to the data. While investigating this procedure through literature searches, a similar filter using the Blackman window was found. This filter is basically an extension of the Hanning filter extended to higher frequencies and results in a stronger attenuation of the high frequency components of the data.

97

Discussions with several individuals led to the suggestion that since the power spectrum is of interest eventually, the smoothing procedure might be based on a fourier transform. This would enable the analysis program to provide information on the atmospheric wave structure at the same time that it was smoothing the data. Accordingly, a FFT program was obtained to evaluate the performance relative to the other smoothing procedures. The FFT program was used to evaluate the results of the other smoothing procedures as well as the FFT-based procedures. The FFT-based procedures were based on simple windowing of the terms of the fourier transform to reduce the high frequency components of the transform. The windows considered were a) rectangular (sharp cutoff), b) linear cutoff, c) cosine cutoff and d) exponential cutoff.

A.2. Impulse Test

A single point unit impulse function was first used as the input to the filters being evaluated because the power spectrum for the impulse is flat. The function consists of 256 points, all zero except the 128th, which is 1.0. The power spectrum of this function is 1.0 for all frequencies. All the filters are designed to preserve the integral of the input function. The filter widths were adjusted to produce approximately the same width of the output response. To simplify the application of the filters at the end points, the input function was assumed to be circular, i.e. it was wrapped around at the ends. This did not affect the impulse function but did affect the random numbers used in subsequent tests (see below).

A2.1 Sliding Average (Rectangular Window)

The sliding average is a commonly used procedure which is very simple but not very effective. Figure A1(a) shows that this procedure does indeed reduce the excursion of an impulse from the mean but leaves a rectangular excursion with sharp edges. This leaves high frequencies in the data. The power spectrum of the averaged data is shown in Figure A1(b). The only real advantage of this procedure is its simplicity. A 9 point filter width was used, that is, 4 points plus the central point.

A2.2 Hanning Filter (Raised Cosine Window)

The sliding average described above is based on a rectangular window weighting function, that is, all the points are equally weighted for each averaged point. The Hanning filter is a similar procedure except that the averaged points are weighted by a function which falls smoothly to zero at the end points. For the particular case of the Hanning filter the function is:

$$\{1 + \cos[\text{pi} / (n + 1)]\} / 2.$$

An impulse and the Hanning filter response are shown in Figure A2(a). The high frequencies are attenuated much more strongly, as can be seen in the power spectrum of the filter output, shown in Figure A2(b). This procedure is basically just as simple as the sliding average except for the weighting function and produces a much sharper cutoff of the high frequencies. Figure A1(a) shows that no apparent extraneous frequencies (ringing) are introduced by the filter. A 17 point filter width was used. This is similar to the 9 point width of the rectangular window since the central 9 points of the window represent the half width of the window, that is the point at which the window drops to 0.5 of the peak value.

A2.3 Blackman Filter

The Blackman filter is similar to the Hanning filter except that it is designed to cut the high frequencies more strongly. The Blackman filter is also similar in application to a sliding average but as in the Hanning filter no ringing is introduced by the filter. The filter response is shown in Figure A3(a) and the power spectrum in Figure A3(b). The Blackman window is:

$$\{0.84 + \cos[\text{pi} / (n+1)] + 0.16 \cos [2\text{pi} / (n+1)]\} / 2.$$

A2.4 Fourier Transform, Truncated

Figure A4(a) shows the output of the filter formed by taking the fourier transform of the input data (the impulse) and truncating it after 16 terms (setting all higher terms to zero) (see Figure A4(b)) and then taking the inverse transform. This procedure clearly introduces a strong oscillation in the data which could be mistaken for wave structure. This procedure is therefore unsatisfactory for smoothing lidar data.

A2.5 Fourier Transform, Linear Cutoff

Instead of truncating the fourier transform of the input function, this procedure forces it to zero linearly between the 16th and 24th terms as shown in Figure A5(b). The output of this filter is shown in Figure A5(a). It can be seen that this filter is slightly better at suppressing extraneous oscillations although some overshoot is still evident.

A2.6 Fourier Transform, Cosine Cutoff

This filter uses a cosine to cut off the terms of the fourier transform as shown in Figure A6(a). It

was thought that this might help by removing some discontinuities in the derivative of the fourier transform but the filter output seen in Figure A6(b) exhibits a slightly larger oscillation than in the linear cutoff case.

A2.7 Fourier Transform, Exponential Cutoff

This filter uses an exponential cutoff for the fourier transform. Two variations of this filter are shown in Figure A7. To compare it with the other FFT-based filters a window was chosen which is constant up to the 16th fourier term and decreases exponentially thereafter with a 4 point e-folding rate. The filter response is shown in Figure A7(a) and the power spectrum in Figure A7(b). This is similar to the above FFT-based filter responses in that some overshoot is seen at the edges of the central peak and some residual oscillations can be seen out to the edges of the plot. A second trial was performed on this filter using a 16 point e-folding rate on all terms (no constant terms). Figure A7(c) and A7(d) show the response and the power spectrum respectively. The 16 point e-folding rate was chosen to make the width of the response peak similar to the other filter responses.

A.3 Normal Random Number Input

As a second test, a set of normally distributed random numbers was generated and written to a file. The numbers were read as data and smoothed with the various filters. The smoothed data can be seen in Figures A8(a-g). The same data were used as the input to each filter so the effect on the structure can be more easily compared. The numbers had a mean of zero and a variance of 1. The smoothing procedures with the greatest high frequency rejection are seen in Figures A8(b) and A8(g). Figure A8(b) is the Hanning procedure and A8(g) is the exponential cutoff FFT-based filter.

The exponential cutoff FFT-based filter has a more heavily smoothed response than the Hanning filter even though the impulse response is wider for the Hanning filter. Looking at the impulse response of the filters, we see that while the Hanning filter response is limited to a few points around the impulse, the FFT-based filter uses weighted points from the complete set of input points. The response peak from the FFT filter is narrower at the half power points but the response has wings that extend to the edges of the data set. The FFT-based filter therefore uses all the data points in the smoothing of each point while the Hanning filter uses only local points in the smoothing process. The Hanning filter therefore keeps purely local phenomena local rather than smoothing them out over the entire data set. This and the much lower degree of complexity make the Hanning filter our choice for the lidar data analysis.

100

A.4 Poisson Random Number Input

The final test was similar to the above, but used a Poisson distribution of random numbers as the input data to the filters. The results of this test are shown in Figures A9(a-g). The basic conclusions from the above analysis are the same. The mean of the Poisson distribution was 15, which corresponds to a 3000 shot run at an altitude that would give 5 percent statistics (400 counts) from a 9000 shot run averaged over 9 . points (2.7 km).

In addition to evaluating the different smoothing procedures, the analysis enabled us to look at the effect of the smoothing on the variance or standard deviation of the data. Since these were known for the input data, calculation of the standard deviation of the smoothed data was all that was necessary for this evaluation. The 'effective number' of points used in the smoothing process is found by taking the half points of the impulse response of the filters. As expected, the sliding average just reduced the standard deviation by the square root of the 'effective number' of points in the average. The Hanning filter and the Blackman filter reduced the standard deviation by somewhat more, and the exponential cutoff FFT-based filter reduced the standard deviation the most. The other FFT-based filters reduced the standard deviation somewhat less than the sliding average, exhibiting the effects of the ringing inherent in those filters. Using the 'effective number' of points in the filter to calculate the reduction of the standard deviation therefore overestimates the standard deviation of the Hanning smoothed data by about 30 percent.

From this study, we consider the Hanning filter to be the best filter for the analysis of the lidar data. The sliding average filter was rejected on the basis of insufficient high frequency rejection. The Blackman filter performed well, but not really noticeably better than the Hanning filter. The added terms in the window definition make the slight increase in complexity not worth the effort. The FFT-based filters all have some disadvantage such as ringing or complexity of application. The exponential cutoff FFT filter could be made not to ring but the filter was more complex and more difficult to apply.
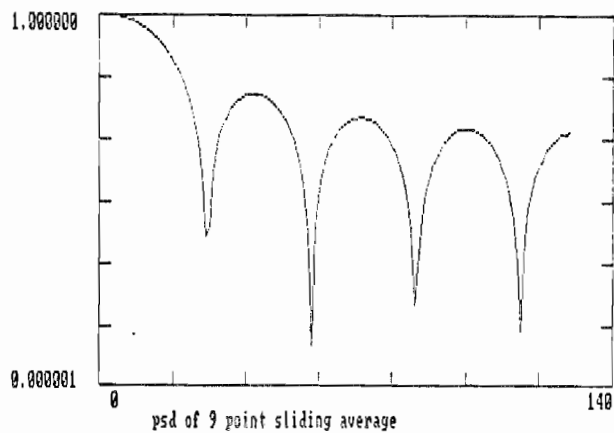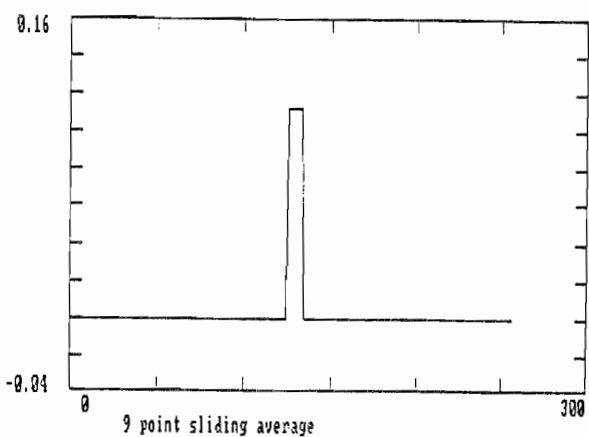
Figure A1. Sliding Average. (a) Rectangular excursion resulting from 9 point sliding average applied to an impulse. (b) Corresponding power spectrum for case (a).
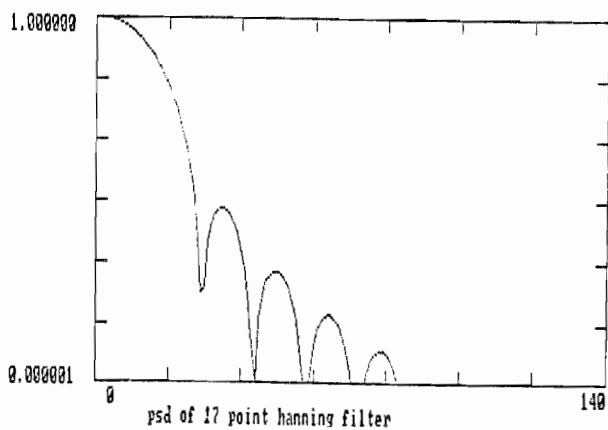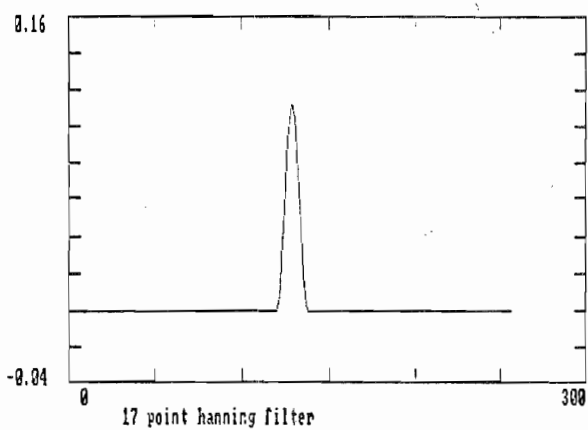
Figure A2. Hanning Filter. (a) Response of Hanning filter to an impulse using a 17 point filter (corresponds to 9 point sliding average). (b) Power spectrum corresponding to case (a).
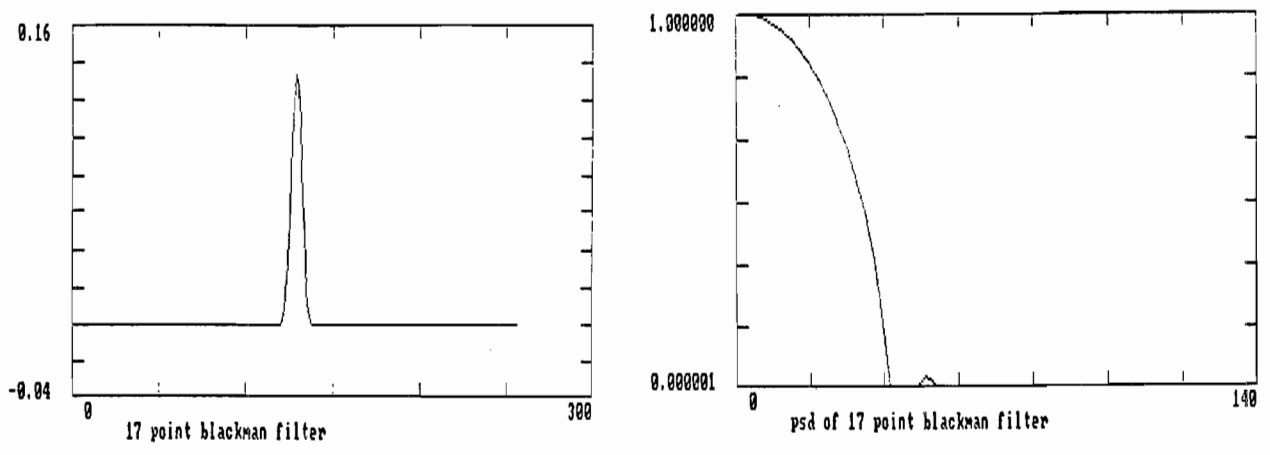
Figure A3. Blackman Filter. (a) Response of 17 point Blackman filter to an impulse. (b) Power spectrum corresponding to case (a).
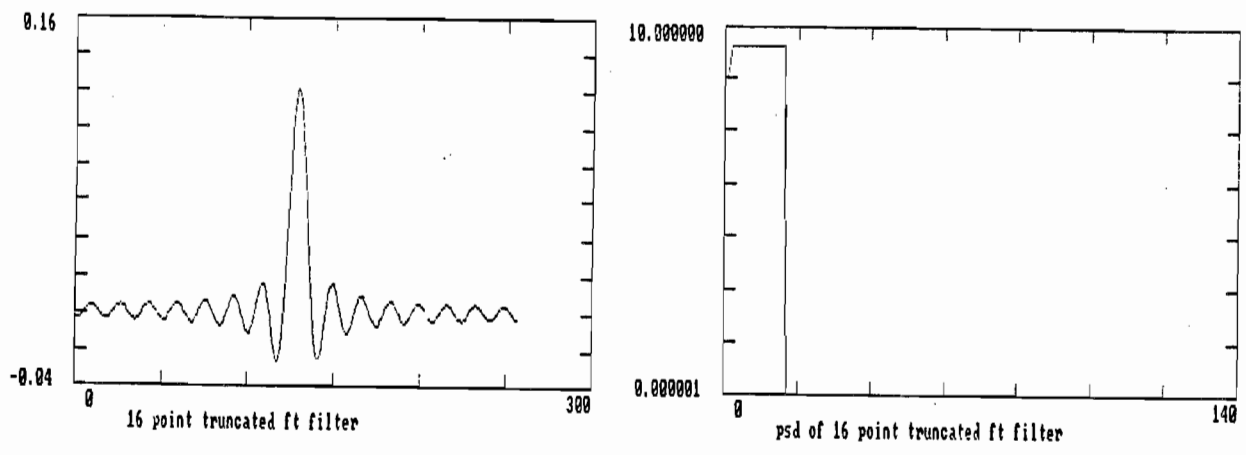
Figure A4. Fourier Transform Filter (Truncated).

103
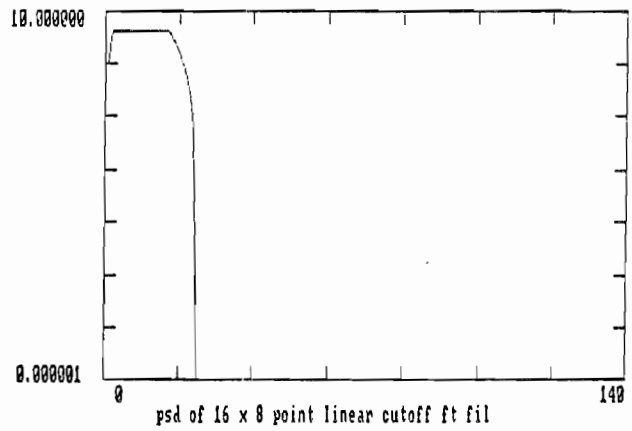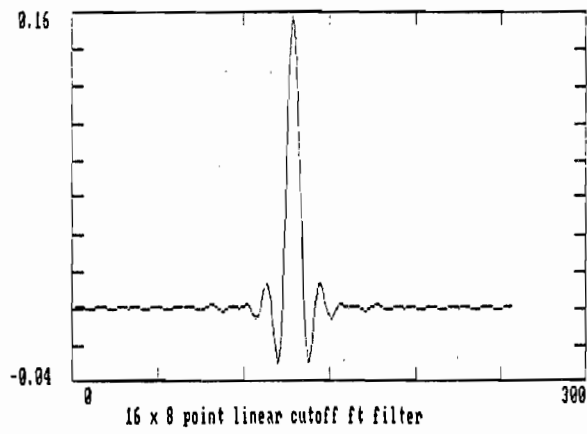
Figure A5. Fourier Transform Filter (Linear Cutoff).
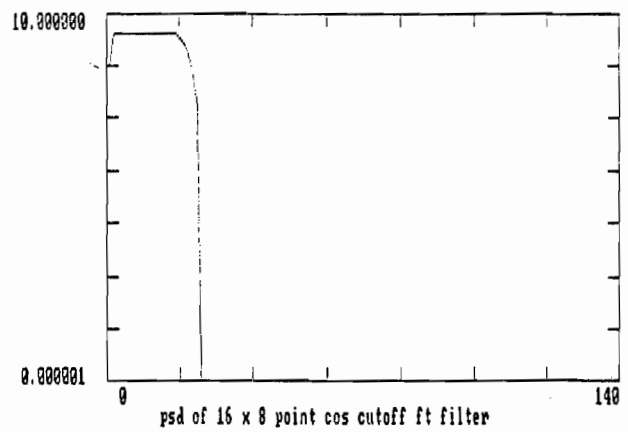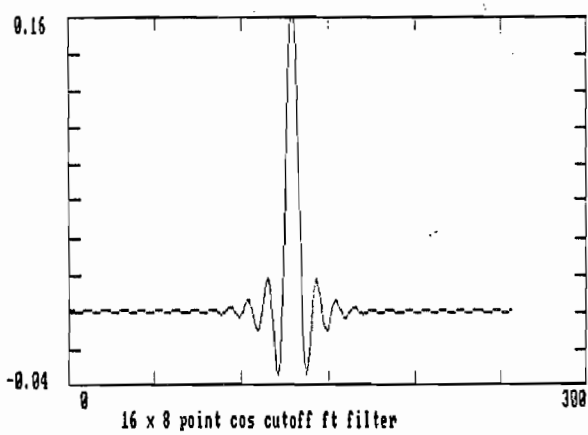
Figure A6. Fourier Transform Filter (Cosine Cutoff).

104

16 x 4 point exp cutoff ft filter

psd of 16 x 4 point exp cutoff ft filter

0 x 16 point exp cutoff ft filter

psd of 0 x 16 point exp cutoff ft filter
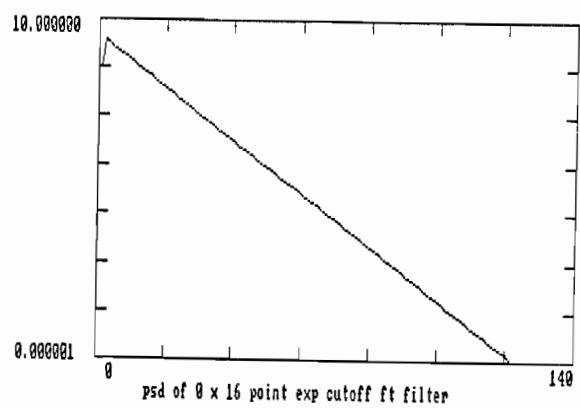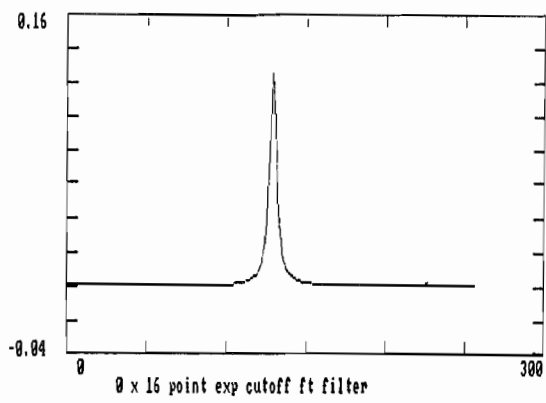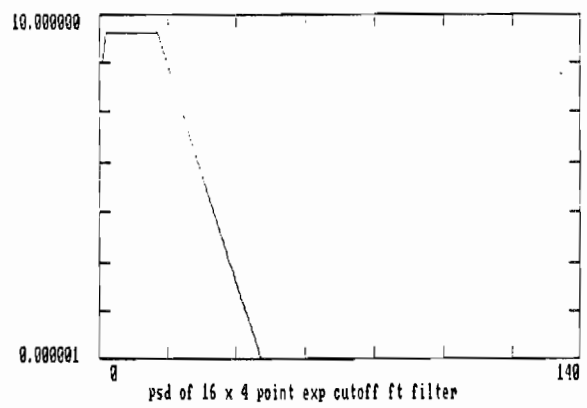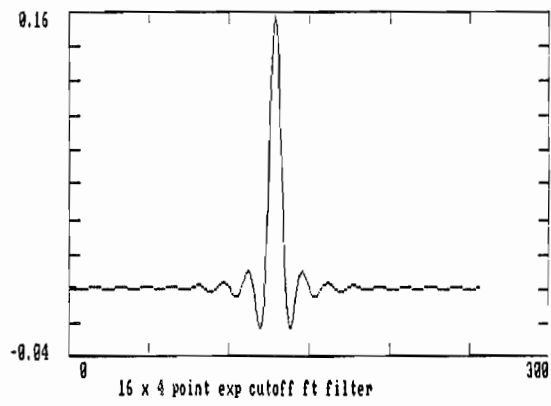
Figure A7. Fourier Transform Filter (Exponential Cutoff).
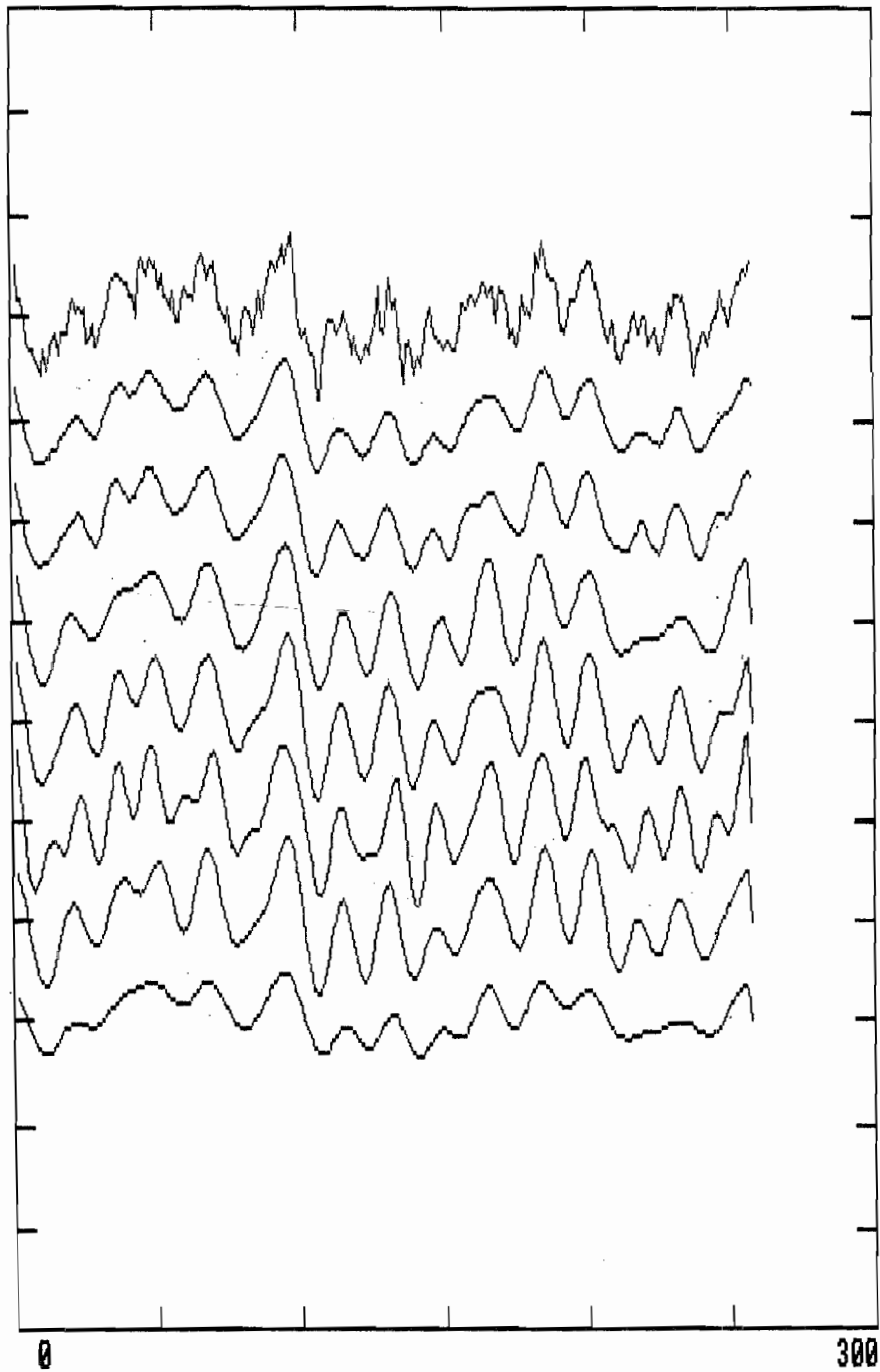
Figure A8. Comparison of the Response of Each of the Filters to the Same Set of Normally Distributed Random Numbers. Curves (a) - (g) represent the 7 cases of filters shown in Figures A1 - A7.

106
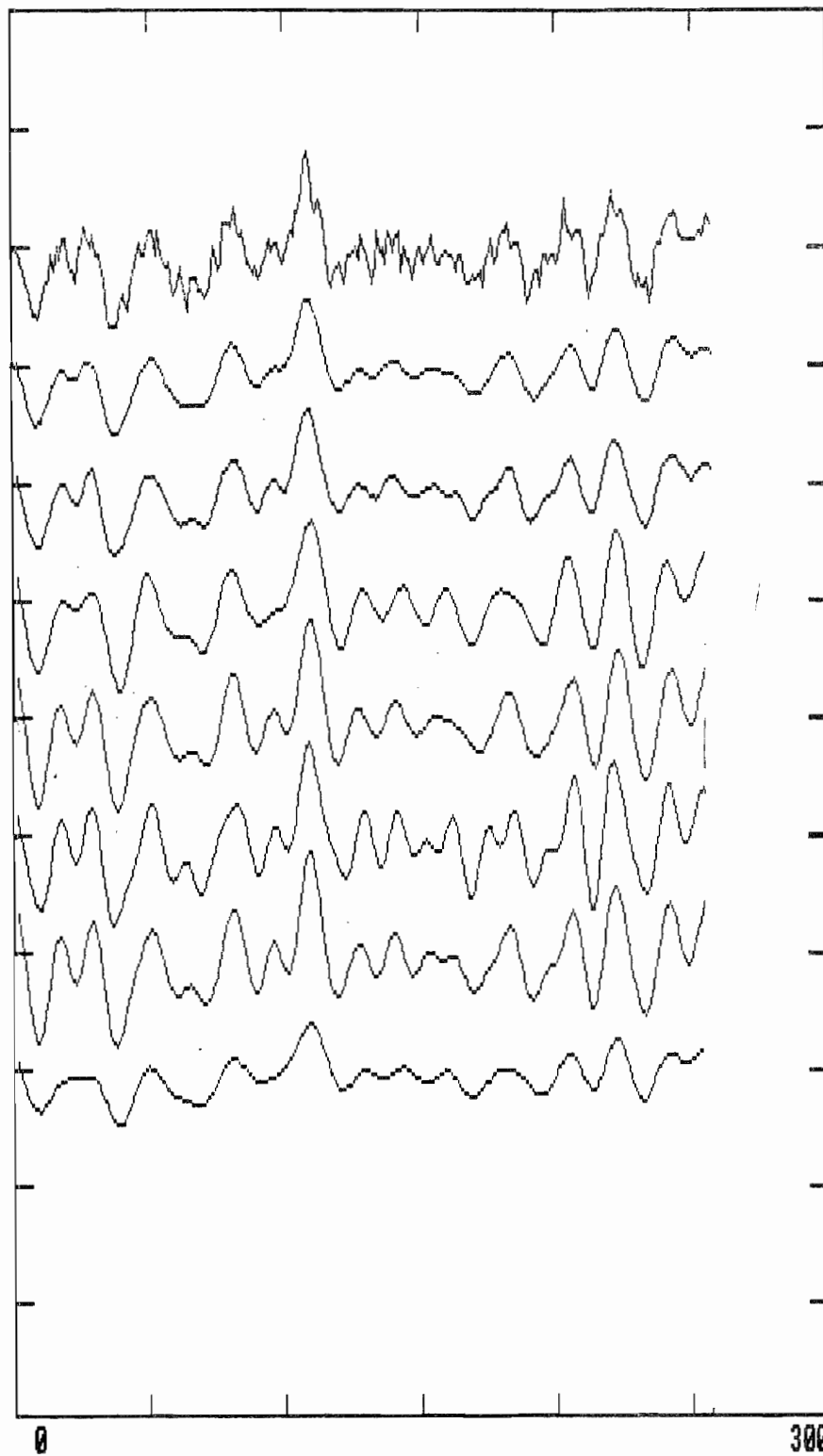
Figure A9. Comparison of the Response of Each of the Filters to the Same Set of Poisson Distributed Random Numbers. Curves (a) - (g) represent the result of applying the 7 filters of Figures A1 - A7.

107

Appendix B

Derivation of FFT Spectral Analysis

This section contains a discussion on the use of Fast Fourier Transform (FFT) analysis to examine the lidar data. The particular advantage of this technique is the ability to investigate the frequency components of waves in the data and the possibility of separating the noise at specific frequencies or at higher frequency than the useful information. The following contribution by Professor C.S. Gardner of the Electro-Optic Systems Laboratory, Department of Electrical and Computer Engineering, University of Illinois at Urbana-Champaign, answers the question of how to properly apply the FFT analysis. In particular, the density-scale height dependence with altitude is included in the formalistic construction of the analysis. This approach has been tested and compared with another approach of detrending the data. By using the ratio of the measured density to the USSA76 model, the large altitude dependence is removed and the standard FFT techniques were applied. There does not appear to be any significant difference between the results from the more formal approach and those from the density ratio to the model.

Professor Gardner's original title for this discussion was "Rayleigh Scatter Lidar Measurements of the Gravity Wave Spectrum."

In an isothermal atmosphere, the steady-state atmospheric density decreases exponentially with altitude,

$$\rho_0(z) = e^{-z/H} \tag{B1}$$

where H is the atmospheric scale height. The density response due to a monochromatic gravity wave is given by[1]

---

[1]Gardner, C.S., and Voelz, D.G. (1986) *Lidar Studies of the Nighttime Sodium Layer Over Urbana, Illinois, 2. Gravity Waves*, EOSL Report No. 86-002, University of Illinois.

$$\rho(z) = e^{-\phi} \, \rho_o(z - \theta_z) \tag{B2}$$

where

$$\phi = \ln\left[1 + \frac{Ae^{\beta z}}{\gamma - 1} \cos(\omega t - k \cdot r)\right] \tag{B3}$$

$$\theta_z = \gamma H \phi \tag{B4}$$

and

$Ae^{\beta z}$ = wave amplitude

β = amplitude growth factor

γ = ratio of specific heats ($\simeq 1.4$)

ω = frequency

k = $k_x \hat{x} + k_z \hat{z}$ = wavenumber vector

λ_x = $\dfrac{2\pi}{k_x}$ = horizontal wavelength

λ_z = $\dfrac{2\pi}{k_z}$ = vertical wavelength

By substituting Eqs. (B3) and (B4) into Eq. (B2), we obtain

$$r(z) \; \frac{\rho(z)}{\rho_o(z)} - 1 = \left[1 + \frac{Ae^{\beta z}}{\gamma - 1} \cos(\omega t - k \cdot r)\right]^{\gamma - 1} - 1$$

$$\simeq Ae^{\beta z} \cos(\omega t - k \cdot r) \; . \tag{B5}$$

It is convenient to use the polarization and dispersion relations for gravity waves to express the wave amplitudes in terms of the amplitudes of the vertical and horizontal winds generated by the wave

110

$$v_z \simeq -\frac{\gamma H \omega}{\gamma - 1} A e^{\beta z} \sin(\omega t - \boldsymbol{k} \cdot \boldsymbol{r})$$

$$\simeq -\left(\frac{\gamma H g}{\gamma - 1}\right)^{1/2} \frac{\lambda_z}{\lambda_x} A e^{\beta z} \sin(\omega t - \boldsymbol{k} \cdot \boldsymbol{r}) \tag{B6}$$

$$v_x \simeq \frac{\gamma H \omega}{\gamma - 1} \frac{\lambda_x}{\lambda_z} A e^{\beta z} \sin(\omega t - \boldsymbol{k} \cdot \boldsymbol{r})$$

$$\simeq \left(\frac{\gamma H g}{\gamma - 1}\right)^{1/2} A e^{\beta z} \sin(\omega t - \boldsymbol{k} \cdot \boldsymbol{r}). \tag{B7}$$

Notice that the horizontal velocity perturbations and the density perturbations differ by a phase shift of $\pi/2$ and a multiplicative constant. Because we are interested in the power spectrum, the phase difference is irrelevant. The power spectra of $r(z)$ and $v_x(z)$ are proportional, and the constant of proportionality is $\left(\frac{\gamma H g}{\gamma - 1}\right)$.

For non-monochromatic waves, it is more convenient to express the velocity in terms of its Fourier transform

$$v_x = \left(\frac{\gamma H g}{\gamma - 1}\right)^{1/2} \int_{-\infty}^{\infty} \int_{-\infty}^{\infty} \int_{-\infty}^{\infty} A(\boldsymbol{k}, \omega)\, e^{i(\omega t - \boldsymbol{k} \cdot \boldsymbol{r})} d\omega \, dk_x \, dk_z \tag{B8}$$

where $A(\boldsymbol{k}, \omega)$ is the random complex amplitude and

$$<A(\boldsymbol{k}_1, \omega_1)\, A^*(\boldsymbol{k}_2, \omega_2)> \;=\; \Phi(\boldsymbol{k}_1, \omega_1)\, \delta(\boldsymbol{k}_1 - \boldsymbol{k}_2)\, \delta(\omega_1 - \omega_2). \tag{B9}$$

$\Phi(\boldsymbol{k}, \omega)$ is the three-dimensional amplitude spectrum. The kinetic energy in the wave field is

$$KE \;=\; \frac{1}{2}\, <v_x{}^2> \;=\; \frac{\gamma H g}{2(\gamma - 1)} \int_{-\infty}^{\infty} \int_{-\infty}^{\infty} \int_{-\infty}^{\infty} \Phi(\boldsymbol{k}, \omega)\, d\omega \, dk_x \, dk_z \tag{B10}$$

so that the three-dimensional energy spectral density is

$$E(\boldsymbol{k}, \omega) \;=\; \frac{\gamma H g}{2(\gamma - 1)}\, \Phi(\boldsymbol{k}, \omega). \tag{B11}$$

Consider the one-dimensional vertical wavenumber spectrum

$$E(k_z) \;=\; \int_{-\infty}^{\infty} \int_{-\infty}^{\infty} E(\boldsymbol{k}, \omega)\, d\omega \, dk_x \tag{B12}$$

111

$$E(k_z) = \int_{-\infty}^{\infty} \frac{1}{2} <v_x(z) \, v_x(z + u)> \, e^{ik_zu} du. \tag{B13}$$

If v_x is an ergodic process, the ensemble average $<\cdot>$ can be approximated by a spatial average

$$<v_x(z) \, v_x(z + u)> \simeq \frac{1}{L} \int_{z_0}^{z_0+L} v_x(z) \, v_x(z + u) \, dz. \tag{B14}$$

By substituting Eq. (B14) into Eq. (B13) and limiting the u integration to the range $(z_0, z_0 + L)$, we obtain

$$E(k_z) \simeq \frac{1}{L} \, |V_x(k_z)|^2 \tag{B15}$$

where

$$V_x(k_z) = \int_{z_0}^{z_0+L} v_x(z) \, e^{ik_zz} \, dz. \tag{B16}$$

Thus, from Eq. (B5) and the discussion following Eq. (B7), we have

$$E(k_z) \simeq \frac{\gamma Hg}{2(\gamma-1)L} \, |R(k_z)|^2 \tag{B17}$$

where

$$R(k_z) = \int_{z_0}^{z_0+L} \left[\frac{\rho(z)}{\rho_0(z)} - 1 \right] e^{ik_zz} dz. \tag{B18}$$

The photocount in a Rayleigh lidar system is proportional to the atmospheric density and inversely proportional to the square of the range. For a zenith-pointing lidar, the expected photocount in the absence of wave perturbations can be modeled as

$$<N(z)> \simeq \frac{z_0^2 N_0}{z^2} \, e^{-(z-z_0)/H} \tag{B19}$$

112

where $N(z)$ is the measured photocount and N_0 is the expected photocount at $z = z_0$. The atmospheric density is estimated from the measured photocount by range scaling and multiplying by an appropriate scaling constant ξ,

$$\tilde{\rho}(z) = \xi \, z^2 \, N(z). \tag{B20}$$

The unperturbed atmospheric density is approximately

$$\rho_0(z) \simeq \rho_0 \, e^{-(z-z_0)/H}. \tag{B21}$$

where ρ_0 is the density at $z = z_0$. Thus, the measured value of $r(z)$ is

$$r(z) = \frac{\xi z^2 N(z)}{\rho_0(z)} - 1. \tag{B22}$$

$R(k_z)$ is estimated by computing the discrete Fourier transform of $r(z)$

$$R(k_z) \simeq \sum_m \left[\frac{\xi(m\Delta z)^2 \, N(m\Delta z)}{\rho_0(m\Delta z)} - 1 \right] e^{ik_z m\Delta z} \Delta z \tag{B23}$$

where Δz is the lidar range gate width. Because $N(m\Delta z)$ is a Poisson process, the photocount fluctuations will introduce noise into the calculated values of $R(k_z)$. The expected power spectrum is

$$<|R(k_z)|^2> = \sum_m \sum_l \left< \left[\frac{\xi(m\Delta z)^2 \, N(m\Delta z)}{\rho_0(m\Delta z)} - 1 \right] \right.$$
$$\left< \left[\frac{\xi(l\Delta z)^2 \, N(l\Delta z)}{\rho_0(l\Delta z)} - 1 \right] \right> e^{ik_z(m-l)\Delta z} \Delta z^2. \tag{B24}$$

Eq. (B24) can be simplified by noting that

$$<N(m\Delta z)N(l\Delta z)> = \begin{array}{ll} <N_m> \, <N_l> & m \neq l \\ <N_m>^2 + \, <N_m> & m = l. \end{array} \tag{B25}$$

As a consequence of Eq. (B25), we have

$$\langle |R(k_z)|^2\rangle = \left| \sum_m \left[\frac{\xi(m\Delta z)^2 \langle N(m\Delta z)\rangle}{\rho_o(m\Delta z)} - 1 \right] e^{ik_z m\Delta z}\Delta z \right|^2$$

$$+ \sum_m \frac{\xi^2(m\Delta z)^4 \langle N(m\Delta z)\rangle}{\rho_o^2(m\Delta z)} \Delta z^2. \tag{B26}$$

The first term in Eq. (B26) is the spectrum of the density perturbations, while the last term is the shot noise floor. This last term can be evaluated by approximating the summation by an integral and by using Eqs. (B19) and (B21)

$$\sum_m \left[\frac{\xi^2(m\Delta z)^4 \langle N_m\rangle}{\rho_o^2(m\Delta z)} \right] \Delta z^2 \simeq \int_{z_o}^{z_o+L} \frac{z^2\Delta z}{z_o^2 N_o} e^{(z-z_o)/H} dz$$

$$\simeq \frac{\Delta z H}{N_o} \left(1 + \frac{L-H}{z_o}\right)^2 e^{L/H}. \tag{B27}$$

The noise floor level is inversely proportional to the photocount at z_o and grows exponentially with L, the altitude range of the observations. Thus, from Eqs. (B17), (B26) and (B27), we obtain

$$\frac{\gamma H g}{2(\gamma-1)L} \langle |R(k_z)|^2\rangle \simeq E(k_z) + \frac{\gamma H g\Delta z}{2(\gamma-1)N_o} \frac{H}{L} \left(1 + \frac{L-H}{z_o}\right)^2 e^{L/H}. \tag{B28}$$

Smith et al.[2] have derived a theoretical expression for $E(k_z)$ which appears to agree with radar wind measurements in the mesosphere

$$E(k_z) = \frac{\lambda_z^3}{4\pi T_g^2} = \frac{(\gamma-1)g\lambda_z^3}{16\pi^3\gamma H}. \tag{B29}$$

Thus, the vertical wavenumber spectrum will be greater than noise floor provided

$$\lambda_z^3 > \frac{g^2 T_g^4}{2\pi} \frac{\Delta z}{N_o} \frac{H}{L} \left(1 + \frac{L-H}{z_o}\right)^2 e^{L/H}. \tag{B30}$$

Equation (B30) defines the resolution of the Rayleigh scatter lidar. Shorter wavelengths can be observed only by increasing the photocount rate $N_o/\Delta z$ at $z = z_o$ or by decreasing the altitude range of the observations L. It is more convenient to express Eqs. (B28) and (B30) in terms of the total photocount comprising a density profile

[2]Smith, S.A., Fritts, D.C., and VanZandt, T.E. (1987) Evidence for a saturated spectrum of atmospheric gravity waves, *J. Atmos. Sci.*, 44: 1404

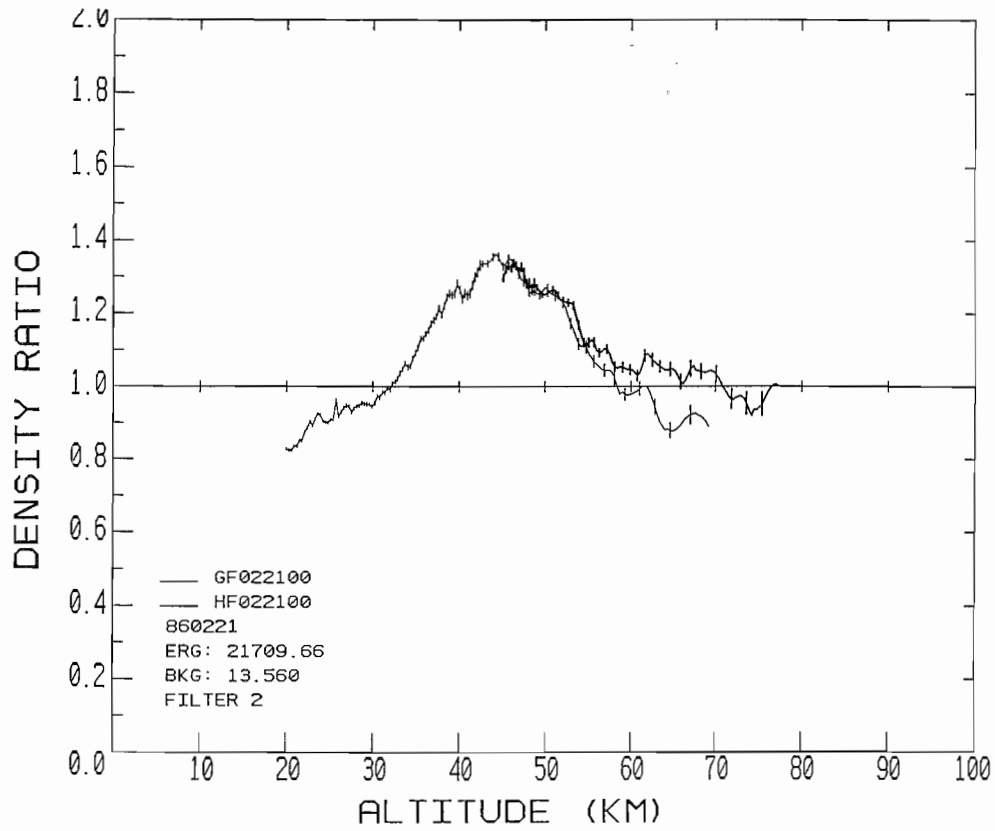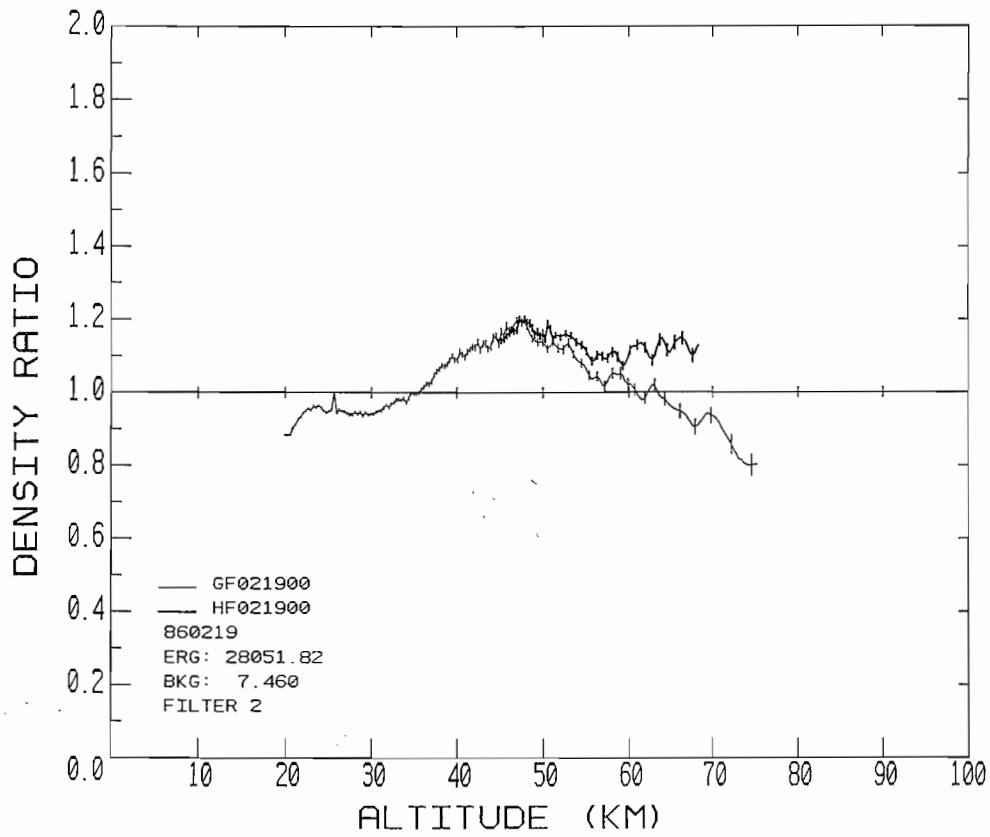$$N_T = \sum_m \frac{z_o^2 N_o}{(m\Delta z)^2} \ e^{-(m\Delta z - z_o)/H} \simeq \frac{z_o^2 N_o}{\Delta z} \int_{z_o}^{z_o + L} \frac{e^{(z-z_o)/H}}{z^2} \ dz \simeq \frac{N_o H}{\Delta z}. \tag{B31}$$

As a consequence of Eq. (B31), we have

$$\frac{\gamma H g}{2(\gamma - 1)L} <|R(k_z)|^2> \simeq E(K_z) + \frac{g^2 T_g^2 H}{8\pi^2 N_T} \frac{H}{L} \left(1 + \frac{L-H}{z_o}\right)^2 e^{L/H}. \tag{B32}$$

For $z_o = 30$ km, $L = 30$ km and $H = 6$ km, Eq. (B32) becomes

$$\frac{\gamma H g}{2(\gamma - 1)L} <|R(k_z)|^2> \simeq E(K_z) + 100 \ \frac{g^2 T_g^2 H}{8\pi^2 N_T} = E(k_z) + \frac{6 \times 10^{10}}{N_T}. \tag{B33}$$

Alternatively, Eq. (B30) becomes

$$\lambda_z^3 > \frac{g^2 T_g^4 H}{2\pi \ N_T} \frac{H}{L} \left(1 + \frac{L-H}{z_o}\right)^2 e^{L/H} = \frac{6.7 \times 10^{16}}{N_T} \tag{B34}$$

or

$$\lambda_z(\text{km}) > \frac{400}{N_T^{1/3}}. \tag{B35}$$

For $N_T = 10^5$, we have $\lambda_z > 8.6$ km.

References

1. Gardner, C.S., and Voelz, D.G. (1986) *Lidar Studies of the Nighttime Sodium Layer Over Urbana, Illinois, 2. Gravity Waves*, EOSL Report No. 86-002, University of Illinois.

2. Smith, S.A., Fritts, D.C., and VanZandt, T.E. (1987) Evidence for a saturated spectrum of atmospheric gravity waves, *J. Atmos. Sci.*, **44**: 1404

APPENDIX C: DATA PLOTS OF NIGHTLY SUMMARIES

These summary plots of the mean profiles are obtained by combining all of the data available on each night of operation. The large number of data runs on some of the nights lead to small statistical errors, but at the expense of removing the short term variations. These plots are very useful for studying the variations of the atmosphere associated with planetary and tidal waves. The strong seasonal variations are also apparent in the comparison of the results from the various dates. The larger number of counts in each range bin means that the smoothing lengths and thresholds can be improved significantly. Note that the $\pm 1\sigma$ error is greatly reduced. All of the results are shown relative to the USSA76 model atmosphere.

118

Top figure:
- GF021900
- HF021900
- 860219
- ERG: 28051.82
- BKG: 7.460
- FILTER 2

Axes: DENSITY RATIO (vertical, 0.0 to 2.0), ALTITUDE (KM) (horizontal, 10 to 100)

Bottom figure:
- GF022100
- HF022100
- 860221
- ERG: 21709.66
- BKG: 13.560
- FILTER 2

Axes: DENSITY RATIO (vertical, 0.0 to 2.0), ALTITUDE (KM) (horizontal, 10 to 100)

121

122

123

124

126

128

Y axis: DENSITY RATIO (0.0 to 2.0)
X axis: ALTITUDE (KM) (10 to 100)

Legend:
GF042800
HF042800
860428
ERG: GY47799.24
BKG: 1062.640
FILTER 2